PYROLYSIS OF POLYLACTIC ACID USING BIFUNCTIONAL CATALYST

A THESIS SUBMITTED TO
THE GRADUATE SCHOOL OF NATURAL AND APPLIED SCIENCES
OF
MIDDLE EAST TECHNICAL UNIVERSITY

BY

UĞUR SÖKMEN

IN PARTIAL FULFILLMENT OF THE REQUIREMENTS
FOR
THE DEGREE OF MASTER OF SCIENCE
IN
CHEMICAL ENGINEERING

DECEMBER 2024

Approval of the thesis:

PYROLYSIS OF POLYLACTIC ACID USING BIFUNCTIONAL CATALYST

submitted by **UĞUR SÖKMEN** in partial fulfillment of the requirements for the degree of **Master of Science in Chemical Engineering, Middle East Technical University** by,

Prof. Dr. Naci Emre Altun
Dean, **Graduate School of Natural and Applied Sciences**

Prof. Dr. Yusuf Uludağ
Head of the Department, **Chemical Engineering**

Prof. Dr. Naime Aslı Sezgi
Supervisor, **Chemical Engineering, METU**

Assoc. Prof. Dr. Çerağ Dilek Hacıhabiboğlu
Co-Supervisor, **Chemical Engineering, METU**

Examining Committee Members:

Prof. Dr. Fatma Suna Balcı
Chemical Engineering, Gazi University

Prof. Dr. Naime Aslı Sezgi
Chemical Engineering, METU

Assoc. Prof. Dr. Çerağ Dilek Hacıhabiboğlu
Chemical Engineering, METU

Prof. Dr. Yusuf Uludağ
Chemical Engineering, METU

Prof. Dr. Göknur Bayram
Chemical Engineering, METU

Date: 04.12.2024

I hereby declare that all information in this document has been obtained and presented in accordance with academic rules and ethical conduct. I also declare that, as required by these rules and conduct, I have fully cited and referenced all material and results that are not original to this work.

Name Last name : Uğur Sökmen

Signature :

ABSTRACT

PYROLYSIS OF POLYLACTIC ACID USING BIFUNCTIONAL CATALYST

Sökmen, Uğur
Master of Science, Chemical Engineering
Supervisor : Prof. Dr. Naime Aslı Sezgi
Co-Supervisor: Assoc. Prof. Dr. Çerağ Dilek Hacıhabiboğlu

December 2024, 126 pages

Polylactic acid is a promising polymer thanks to being biodegradable. PLA could be utilized to diminish environmental problems caused by non-biodegradable petroleum-based polymers. However, misconceptions about the biodegradability of PLA lead to PLA waste. Nature lacks the proper conditions, such as temperature, pH, etc., that PLA requires to decompose easily; therefore, PLA waste is inevitable. Thus, the aim of this study was to investigate PLA degradation using a catalyst. In this study support material mesoporous silica aerogel was synthesized via sol-gel method. Al and Fe metals were loaded to silica aerogels at different Al to Fe weight ratios via the wet impregnation method. Metal-loaded silica aerogels were characterized using various characterization techniques. The effects of Al/Fe weight ratio, temperature, and reaction time on the product yield and distribution in the depolymerization of PLA were investigated in a pyrolysis system. Regarding the Al/Fe weight ratio, the best-performing catalyst was found to be SimSAU0.5Al14.5Fe in terms of lowest solid yield (11.5 %) and highest condensable product yield (51 %). Thus, the effect of temperature and reaction time was investigated only for the best-performing catalyst.

Increasing the temperature yielded less condensable products, and more non-condensable products. Main condensable products were DL, L, and Meso L. The concentration of the main condensable products decreased with an increase in temperature. Main non-condensable products were acetaldehyde, and carbon monoxide. Whereas acetaldehyde concentration increased with an increase in temperature, carbon monoxide concentration decreased.

Eventually, when the reaction time was increased from 60 minutes to 120 minutes at 225 ℃ no solid was observed. Moreover, a slight increase in condensable product yield was also observed with the increase in reaction time. The highest lactide yield was obtained at 225 ℃ and 120 minutes.

Keywords: Polylactic acid, Biodegradable Polymers, Pyrolysis, Silica Aerogel, Bifunctional Catalyst, Lactide, Lactic Acid,

ÖZ

POLİLAKTİK ASİDİN BİFONKSİYONEL KATALİZÖR KULLANILARAK PİROLİZİ

Sökmen, Uğur
Yüksek Lisans, Kimya Mühendisliği
Tez Yöneticisi: Prof. Dr. Naime Aslı Sezgi
Ortak Tez Yöneticisi: Doç. Dr. Çerağ Dilek Hacıhabiboğlu

Aralık 2024, 126 sayfa

Polilaktik asit biyolojik olarak bozunabilen bir polimer olması dolayısıyla umut vadeden bir polimer olarak ortaya çıkmaktadır. Polilaktik asit petrol bazlı biyolojik olarak bozunamayan polimerlerin çevrede sebep olduğu problemleri azaltabilmektedir. Yine de, PLA'nın biyolojik olarak bozunabilmesi hakkındaki yanlış kanılar PLA atığına sebep olmaktadır. PLA'nın kolayca bozunabilmesi için gereken sıcaklık, pH vb., koşullar doğada uygun olmadığından PLA atığı kaçınılmazdır. Buna bağlı olarak, bu çalışmanın amacı PLA bozunmasını katalizör kullanarak incelemektir. Bu çalışmada destek malzemesi, silika aerojel sol-jel yöntemi ile sentezlenmiştir. Al ve Fe metalleri farklı ağırlık oranlarında ıslak emdirme yöntemi kullanılarak silika aerojellere yüklenmiştir. Metal yüklü silika aerojeller çeşitli karakterizasyon teknikleri kullanılarak karakterize edilmiştir. Al/Fe ağırlık oranının, sıcalık ve reaksiyon süresinin PLA depolimerizasyonundaki ürün verimindeki ve ürün dağılımındaki etkileri piroliz sisteminde incelenmiştir. Al/Fe ağırlık oranına bakılarak en düşük katı ürün verimi (% 11.5), ve en yüksek yoğuşabilir ürün verimi (% 51) açısından SimSAU0.5Al14.5Fe en iyi performans gösteren katalizör olarak bulunmuştur. Bu yüzden, sıcaklık ve reaksiyon süresi etkisi sadece en iyi performansı gösteren katalizör için incelenmiştir.

Sıcaklığın artmasıyla daha az yoğuşabilir ürün ve daha fazla yoğuşmayan ürün elde edilmiştir. Ana yoğuşabilir ürünler DL, L ve Mezo laktittir. Ana yoğuşabilir ürünlerin konsantrasyonu sıcaklığın artmasıyla azalmıştır. Ana yoğuşmayan ürünler asetaldehit ve karbon monoksittir. Asetaldehit konsatrasyonu sıcaklığın artmasıyla artarken karbon monoksit konsantrasyonu azalmıştır.

Son olarak reaksiyon süresinin 225 °C'de 60 dakikadan 120 dakikaya çıkarılmasıyla katı ürün gözlemlenmemiştir. Ayrıca, yoğuşabilir ürün veriminde reaksiyon süresinin artmasıyla az bir yükseliş gözlemlenmiştir. En yüksek laktit verimi 225 °C'de ve 120 dakikada elde edilmiştir.

Anahtar Kelimeler: Polilaktik Asit, Biyolojik Bozunabilen Polimerler, Piroliz, Silika Aerojel, Çift Fonksiyonlu Katalizör, Laktit, Laktik Asit

To my dear family and lovely fiancée Elif

ACKNOWLEDGMENTS

First of all, I would like to express my deepest sincere appreciation to my supervisor Prof. Dr. Naime Aslı Sezgi, for her belief in me, guidance, support, and understanding. Her broad knowledge and experience made me extremely motivated and believed in myself. Nothing could describe how grateful I am for having the chance to study under her supervision. I would also like to express my deepest gratitude to my cosupervisor, Assoc. Prof. Dr. Çerağ Dilek Hacıhabiboğlu, for her guidance and endless support.

I would like to express my gratitude to Kinetic Laboratory Members Merve Sarıyer, Seda Sivri, Emel Muşdu, and Salih Ermiş for their help when I need it.

I would like to extend my gratitude to Candan Akyıldız, Enes Akyıldız, Arzum Ceren Aydoğdu, Günalp Taşdelen, and Özgür Gülmez for the very valuable friendship that we have had and the road that we have got over together.

During this journey, I had lots of help from METU Chemical Engineering Department Staff; therefore, it would be missing if I did not express my thanks to Mihrican Açıkgöz, Doğan Akkuş, Murat Akgün, Ramazan Küçükdanışman, Mahmut Akdağ, Sedat Taşbaşı, Sedef Araz, Özlem Güven Pak, and Cemil Araçlı.

Last but not least, as in always in my mind, I wish to express my feelings for my family. It would not be possible to become who I am, this strong to endure all the toxicity around if my lovely fiancée Elif Ferligül, my mother Bedia Sökmen, my aunt Fedva Sülooğlu, my sister Asya Sökmen, my brothers Sami and İbrahim Sökmen support me whenever I lose faith. I am so lucky to have you with me with all the challenges. You have always been with me through thick and thin.

I would like to finish my gratitude with a quote from Leo Tolstoy that has shaped my life. "All great literature is one of two stories; a man goes on a journey or a stranger comes to town."

TABLE OF CONTENTS

CHAPTERS

APPENDICES

LIST OF TABLES

TABLES

LIST OF FIGURES

FIGURES

LIST OF ABBREVIATIONS

BSE	Backscattered Electrons
D L, L	The mixture of D Lactide and L Lactide
EDX	Energy Dispersive X-Ray Microscopy
FID	Flame Ionization Detector
FTIR	Fourier Transform Infrared Spectroscopy
GC	Gas Chromatography
LA	Lactic Acid
LDPE	Low-Density Polyethylene
Meso L	Meso Lactide
MPs	Microplastics
NC	Non-Catalytic
PA	Propionic Acid
PBS	Polybutylene Succinate
PBSA	Polybutylene Succinate Adipate
PCL	Polycaprolactone
PE	Polyethylene
PET	Polyethylene Terephthalate
PGA	Polyglycolide
PHA	Polyhydroxyalkanoates
PLA	Polylactic Acid

PP	Polypropylene
PS	Polystyrene
PSD	Pore Size Distribution
PU	Polyurethane
PVC	Polyvinyl Chloride
rpm	Revolutions Per Minute
SA	Calcined Silica Aerogel
SAU	Uncalcined Silica Aerogel
SEM	Scanning Electron Microscopy
TCD	Thermal Conductivity Detector
TGA	Thermogravimetric Analysis
UI	Unidentified Products

LIST OF SYMBOLS

A	Pre-exponential factor, 1/s
A_i	GC area of the compound i, mVolt^2*sec
E_a	Activation energy of the reaction, kJ/mol
$M_{condensable}$	Weight of the condensable product, mg
MW_i	Molecular weight of the compound i, g/mol
$M_{initial\ PLA}$	Initial weight of the PLA polymer, mg
$M_{non\text{-}condensable}$	Weight of the non-condensable product, mg
M_{solid}	Weight of the solid product, mg
N	Overall reaction order
N_i	Moles of compound i, mol
R	Gas constant, 8.314 J/(mol*K)
RRF_i	Relative response factor of compound i
t	Time, min
T	Temperature, ℃

V_i	Volume of compound i, ml
W_i	Weight fraction of compound i
W_0	Initial weight of the sample, mg
W_t	Weight of the sample at time t, mg
W_α	Weight of the sample at infinite time, mg
Y_i	Yield of solid, or condensable, or non-condensable product
y_i	Mole fraction of compound i

Greek Letters

ρ_i	The density of compound i, g/cm^3
β_i	The beta factor of compound i,
α_i	Fraction of PLA decomposed at time t
ϑ_{Ar}	Volumetric flow rate of argon, ml/min

CHAPTER 1

INTRODUCTION

It has always been a challenge for society to build secure, enduring, flexible, strong materials from ever since the beginning of humanity. This challenge has been the utmost driving force in the search for new materials. Starting from wood, brick, and steel to polymers, that journey has been both struggling and full of opportunities. It was not till the Second World War, that people were unaware of polymers even though they had used polymers in their lives for many decades (Rahman et al., 2020). With the increase in demand for manufactured products at that time, people became familiar with the breakthrough brand-new material that is polymers. Until that time mostly known materials were steel, glass, wood, and brick. No one could imagine at that time that this new material would dominate the whole life on the planet ranging from nano chips to automobiles, from cooking materials to clothing. After all, polymers have become a vital part of life, and they are used daily in clothes that we wear, in cups we drink, in bags, paints, and kitchenware (Storage boxes, containers, and so on) that are not easily replaced by other materials.

The seeking of versatile, durable, lightweight, cost-effective, customizable, and sustainable materials throughout the history of mankind has finally brought about unprecedented growth in both usage and research conducted regarding polymers. The word polymer is derived from Greek, and the modern definition of polymer was introduced by German chemist Hermann Staudinger in the 1920s (Namazi, 2017; Rahman et al., 2020). Known as macromolecule or polymer, polymer word comprises two words. With the help of Greek, poly means many and mere meaning part, and when they get combined as the name implies, many structural units or parts bounded with the covalent bond become one molecule which might have a very high molecular weight ranging from 10,000s to 1,000,000s g/mol (Namazi, 2017).

Investigating polymers and their properties, a polymer molecule is made up of a structure called a skeleton that could be linear, branched, or network structure, and atoms or atom groups (Van Krevelen & Nijenhuis, 2009). Besides, the structure of polymers could contain different structural groups such as hydrocarbon groups (CH_3, $-CH=CH_2$), non-hydrocarbon groups (-OH, -SH, NH_2, Cl, $-C \equiv N$), composed groups (-COOH, $-CONH_2$), etc. (Van Krevelen & Nijenhuis, 2009). Depending on the chemical structure, average molecular weight, type and length of the side chains, type of chain being branched, linear; chemical, and physical properties are impacted enormously. Those properties determine the stiffness, hardness, flexibility, and crystallinity of the desired product. A lot of research has been performed leading to the awareness of those properties, and with the modification of the repeating units, type of chains, and end groups, durable, flexible polymers are utilized in every part of life, as one can infer from the use of nylon bags or polyethylene terephthalate (PET) bottles. Those properties facilitated polymers to be regarded as materials of the 21st century, alternatively, the Age of Polymers (Goerg H. Michler & Francisco Balta-Calleja, 2022). It is not surprising to observe that the polymer industry has already taken over steel, copper, aluminum, and some other industries (Karak, 2009). As a result of this drastic increase in demand for polymers, the market size is anticipated to be valued at 1.38 trillion USD by the end of 2036, which was around 721.4 billion USD in 2023 (Research Nester, 2024). Although these promising developments and raises in market size seem profoundly promising and perfect, some other concerns regarding polymers have been arising. Issues related to plastics, which are the most common and widely used synthetic (man-made) polymers, are attempted to be solved.

Plastics such as polyethylene (PE), polypropylene (PP), and polyvinyl chloride (PVC) are the most common plastic types. Although the first plastics were produced around the 1950s (PE bag), from 1950 to 2012, the production of plastics reached around 288 million tons (Bråte et al., 2014). This trend of increase has been exponential and most of the produced plastics (around 50%) are of low value and are designed for single-use applications such as packaging, disposal of consumer items, etc. (Hopewell et al., 2009). Since most of the plastics are not recovered, the waste of those plastics poses a great threat to the environment. Figure 1.1 shows the forecast for plastics waste by year from 2019 to 2060. As can be seen, most plastics, around 65 %, are either mismanaged or landfilled. Therefore, the problem with plastics does not seem to decline if further precautions are not taken.

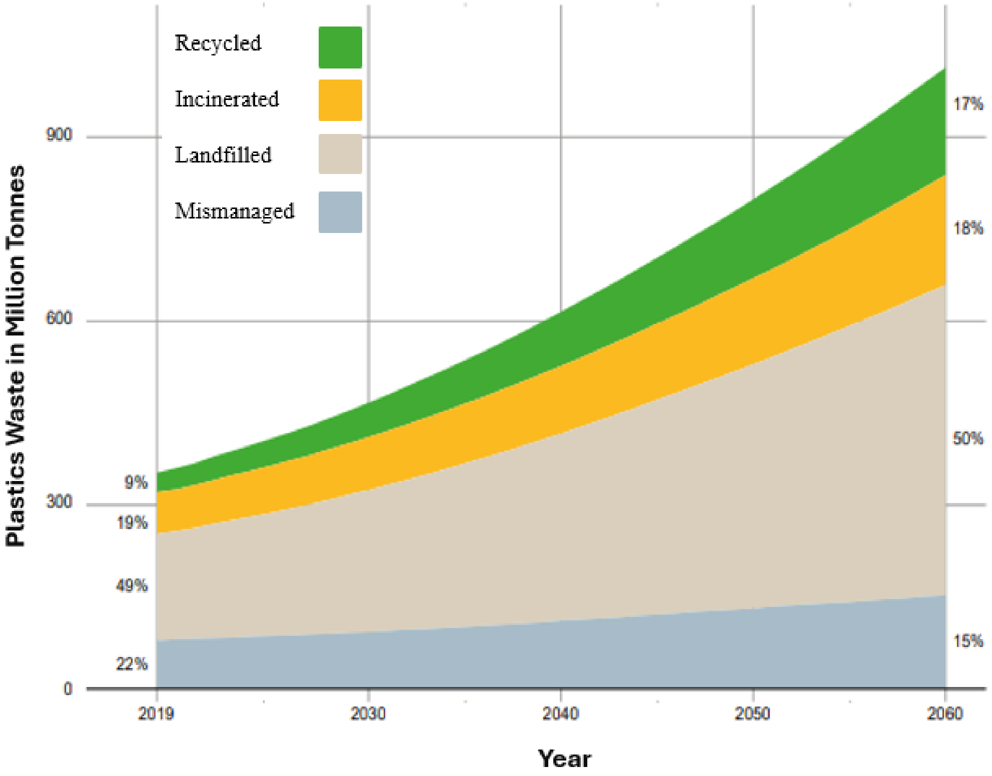

Figure 1.1. Plastics waste by year (OECD, 2022)

Moreover, the trouble has been getting even worse with the fact that plastics, when they enter the environment, are steadily decomposed into smaller particles named microplastics (MPs) (Walker, 2021). In other words, the globe is threatened by microplastics that are invisible to the eyes. These MPs have been found in soil, marines, fresh waters, and terrestrial ecosystems globally, leading to a variety of distinct troubles to confront (Figures 1.2 & 1.3). Therefore, scientists, policymakers, etc., seek urgent solutions to prevent possible irreversible outcomes with different approaches.

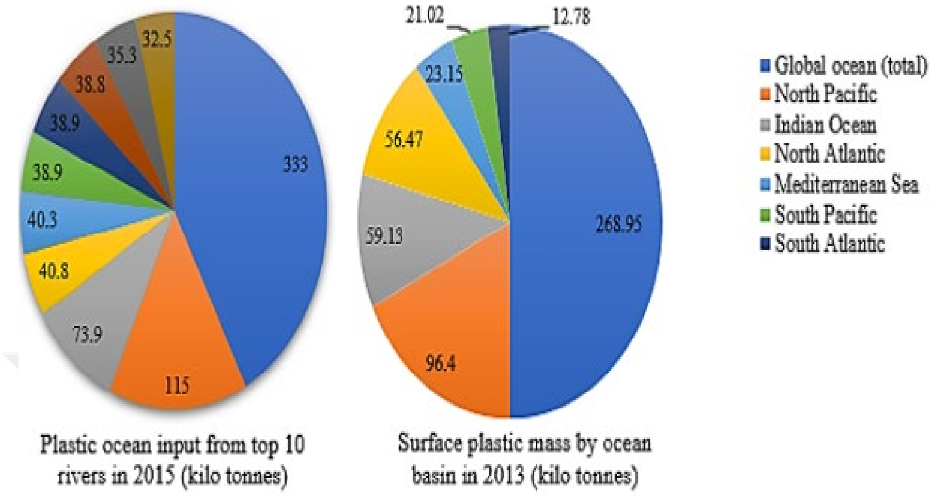

Plastic ocean input from top 10 rivers in 2015 (kilo tonnes)

Surface plastic mass by ocean basin in 2013 (kilo tonnes)

Figure 1.2. Global plastics input to the oceans (Kibria et al., 2023)

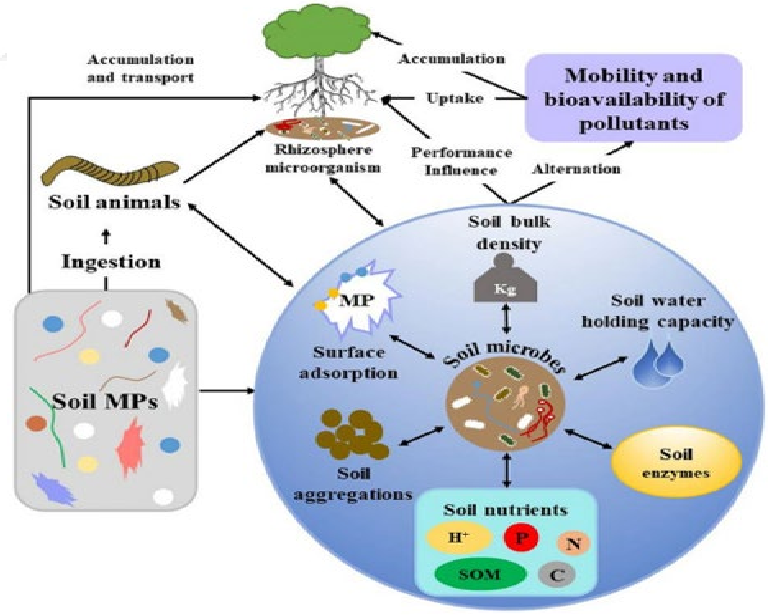

Figure 1.3. Impact of plastics on soil (Kibria et al., 2023)

Specifically, biodegradable polymers were produced especially to solve the problems that appeared because of MPs. However, the issue related to MPs, mostly arising from petroleum-based polymers, could not directly be solved by replacing petroleum-based polymers with biodegradable polymers.

In essence, although biodegradability is an important concept, degradation parameters, as shown in Figure 1.4, such as temperature, microorganism types, being on land or marines, etc., play vital roles in the rate of degradation. In that manner, polylactic acid (PLA), which is a very promising and popular biodegradable polymer, encounters some difficulties in the degradation rate regarding the above-mentioned parameters. Therefore, in this study, the degradation rate of PLA was attempted to be improved in a pyrolysis system by utilizing bifunctional catalysts within determined reaction time ranges.

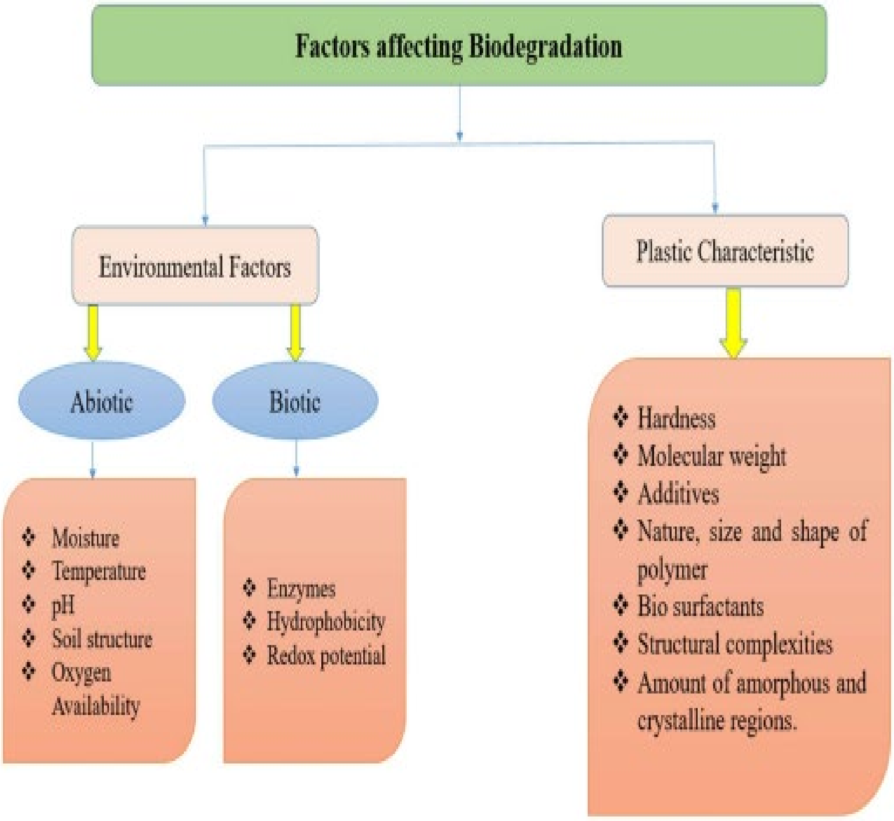

Figure 1.4. Factors affecting biodegradation (Kumari et al., 2023)

1.1 Classification of Polymers

A macromolecule combined by a variety of subunits called monomers, i.e., polymer, could be classified in many different ways. Since polymers have a unique complex structure, it is not possible just to classify them in one category. Therefore, it is better to investigate them according to their structure, applications, the way how they get synthesized, etc. For example, polymers found naturally in plants and animals are regarded as natural polymers, whereas human-made ones are called synthetic polymers. Moreover, there are also semi-synthetic polymers derived from natural resources and then chemically further modified to be semi-synthetic (Examples: Rayon, cellulose nitrate). This way of classification is based on the source of the polymer.

Polymers could further be categorized by the structure of the monomer chain. The categorization of polymers regarding their structure could be performed in different ways in the literature. One way is the following: the monomer chain comprising the polymers might be linear, branched, cross-linked, or networked. A polymer could not only have one of those basic structures but also a mixture of those structures. As can be seen in Figure 1.5, there is a structural difference between those polymers. Linear polymers resemble ‘spaghetti’ as they have long and straight chains. Weak Van der Waals and hydrogen bonds bind together those chains. As a result, applying heat to those chains in the linear polymers could easily break the chains (Redwing, 2024). To illustrate, PVC (Thermoplastic material) used in pipes, cable insulation, etc. - one of the most produced synthetic polymers- is a linear polymer. Linear polymers are typically thermoplastics, which is another way of classifying polymers depending on molecular forces.

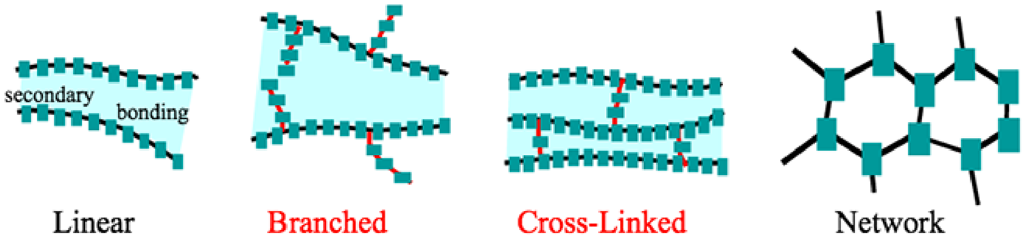

Figure 1.5. Different structures in polymers (Redwing, 2024)

Considering branched polymers, as seen in Figure 1.5, their structure is similar to that of linear polymers, except shorter chains hang from smaller linear chains compared to linear polymers. Moreover, those small hanging chains do not bridge from one linear chain (main backbones) to another, so applying heat breaks the bonds between branched chains and those polymers show the characteristics of thermoplastics (Redwing, 2024). Another structural difference that plays a vital role in classifying the polymers is the cross-linking of the chains within the polymer. In that structure, the main backbones of the linear structure is linked by other smaller chains, and compared to branched ones, they are connected with the other main linear chains within the polymer (Redwing, 2024). Unlike the aforementioned two types, the cross-linked polymer’s structure facilitates a covalent; therefore, cross-linked polymers are also known as thermosetting polymers. The last type of this category is the networked polymers. Those polymers form complex structures via the three-dimensional networking of chains. In addition, heating networked polymers rarely softens the material unless the underlying polymer structure is degraded. Figure 1.6 demonstrates the whole classification that might be performed depending on different aspects.

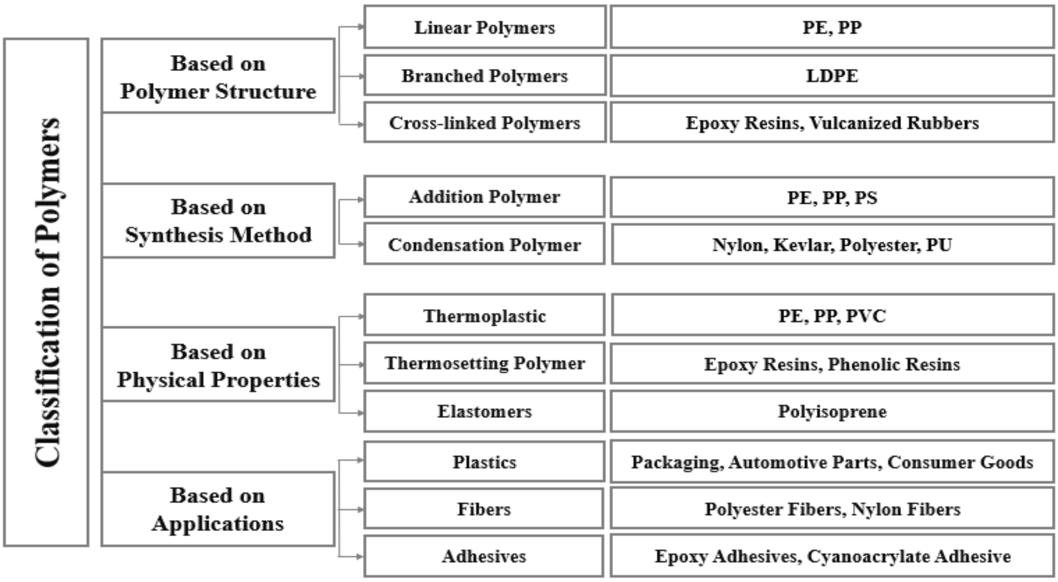

Figure 1.6. Classification of polymers (Safwan-Ul-Iman et al., 2024)

Polymers are synthesized through a process called polymerization. Polymerization can be divided into two categories: condensation and addition polymerization. When monomers of double or triple bonds are added repeatedly to form a polymer, addition polymerization is achieved. In contrast, condensation polymerization requires bi- and tri-functional monomers to be condensed repeatedly. On the other hand, the main difference between these two methods of production is that while addition polymerization gives no other by-product, condensation polymerization could produce H_2O, NH_3, HCl, etc., as a by-product. This could be regarded as another way how polymers are classified based on the synthesis method. Although the categorizing of polymers is very complex and needs more detail, one last detail could be based on forces and application of polymers that actually could not be considered separately.

Considering the intermolecular forces between the polymer chains, four types of polymers are utilized in a variety of industries. The first one is elastomers, rubber-like solid polymers, and chains in their structure are kept together by the weakest intermolecular forces. Weak forces such as in natural rubber (elastomer), provide the polymer with ease in stretchiness. Elastomers have a great range of applications in the industry. Petroleum-based synthetic elastomers are used as seals or hoses in the gas/petroleum industry thanks to their flexibility. Another typical hugely significant industrial application of elastomers is in automobile applications. Tires, gaskets, and adhesives based on elastomers are utilized profoundly in the automotive industry owing to their flexibility and durability. Their application is not just limited to automotive or petroleum; medical products such as gloves, agricultural products such as conveyor belts, consumer products, etc., all take advantage of elastomers to some extent. As a result, those industries, as well, make use of elastomers for most of their applications (Global Elastomeric Products, 2016).

The second intermolecular force-based polymers are fibres. Fibres resembling thread-like nature, having strong intermolecular forces like hydrogen bonding, possess high tensile strength. Possession of high tensile strength provides the ability to withstand pulling stress without breaking. Those polymers are highly demanded in clothing, and their application is beyond the daily used products. The third one is thermoplastics. Those linear polymers have weak Van der Waals forces between the chains, and they could be considered intermediate between elastomers and fibres in terms of the force strength within the polymer. The following properties of thermoplastics make them so promising and, not surprisingly, one of the most demanded polymers (E.g., polyurethane (PU), polystyrene (PS)): Upon heating, they could easily be reshaped and easily cast into different shapes. Eventually, polymers with primary bonds as intramolecular forces stronger than secondary bonds are known as thermosetting plastics. Unlike thermoplastics, thermosetting polymers have no melting points and when they get once hardened by being heated up, they cannot be reshaped, reformed, or recycled. Figure 1.7 gives an idea about the application of polymers. Based on all the characteristics of polymers, distinct applications force/require different categories of polymers or mainly a mixture of those properties.

For the scope of this thesis, one last significant category of polymer is investigated. Above all the mentioned characteristics, a polymer might be non-biodegradable or biodegradable. This classification is similar to source-based since natural polymers could undergo biodegradation, whereas synthetic polymers mostly lack this property. Understanding the degradation process of naturally occurring polymers led scientists to modify and develop new polymeric materials that imitate naturality so that developed plastics could undergo decomposition to fragments such as CO_2, CH_4, H_2O, etc., under aerobic or anaerobic medium by living organisms' action. The importance of biodegradability has been increasing dramatically with the realization of a sustainable future. Therefore, biodegradable polymers such as PLA, polyglycolic acid (PGA), and polycaprolactone (PCL) are becoming very popular, and they are given promising attention by many of the fields related to polymers and polymers based on other applications.

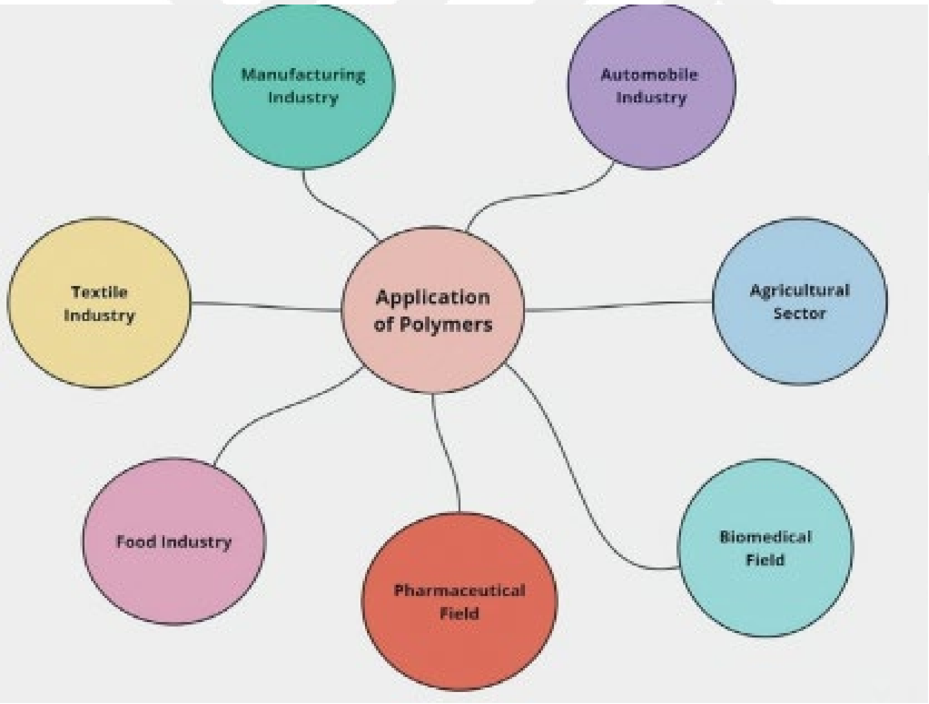

Figure 1.7. Application of polymers (Safwan-Ul-Iman et al., 2024)

1.1.1 Bioplastics

Plastics, being an essential part of society, have recently been posing great adverse effects on humanity. Plastics waste disposal is still a great challenge for industries all around the world. The main adversity of plastics is caused by mass production of plastics from petroleum-based materials (Silva et al., 2023). To diminish the adverse effects of non-biodegradable petroleum-based plastics, bioplastics play a key role. Alternation of the use of non-biodegradable plastic to biodegradable ones is required immediately since waste management of those plastics is highly energy intensive and thus costly because of the high heterogeneity of the content of the plastics. Additives such as plasticizers and stabilizers while producing plastics, and contamination of plastics with organic matter make thermochemical processing of plastics rather difficult (Silva et al., 2023). Unlike petroleum-based plastics, bioplastics could be produced from renewable resources. As in biomass, where the fuel of energy comes from agricultural and forestry residues, bioplastics could also be produced by those ingredients (Samir et al., 2022). On the other hand, sources such as starch or cellulose could also be utilized in the context of bioplastics manufacturing. Therefore, it can be inferred that bioplastics could lead to a more sustainable future compared to petroleum-based plastics so that their peaked demand is inevitable, and this is indeed what happens since global bioplastics production is expected to increase from 2.41 million tonnes to approximately 7.59 million tonnes between 2021 and 2026 (European bioplastics conference, 2021) as can be seen in Figure 1.8.

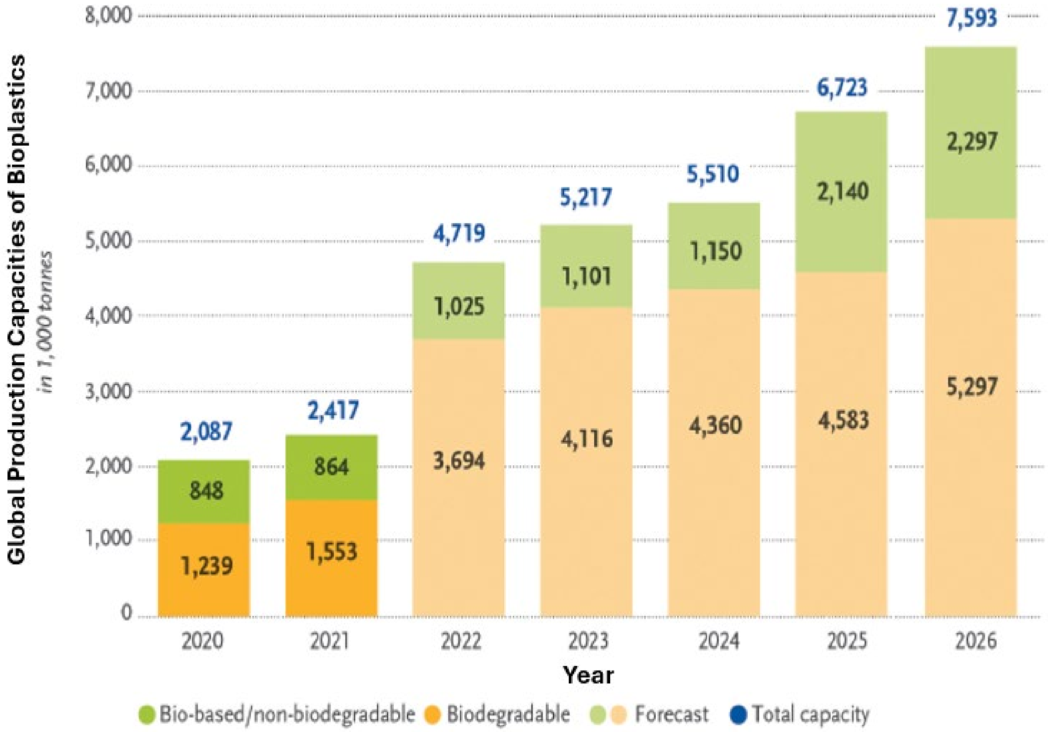

Figure 1.8. Global production of bioplastics between 2020 – 2026 (European bioplastics conference, 2021)

Although the definition of bioplastics is somewhat still not complete, bioplastics comprise all polymers that are produced from natural or renewable sources or those degrade naturally, such as polybutylene succinate (PBS) or have both features, such as polylactic acid (Silva et al., 2023). Having both abilities, being able to be produced by natural or renewable sources and being able to be decomposed, makes biodegradable polymers like PLA even more interesting and more promising to replace non-biodegradable plastics.

Figure 1.9 shows the distribution of PLA and other common biodegradable polymers as a pie chart by production capacity. PLA, with 25%, is the second most produced biodegradable polymer, as can be seen in the figure.

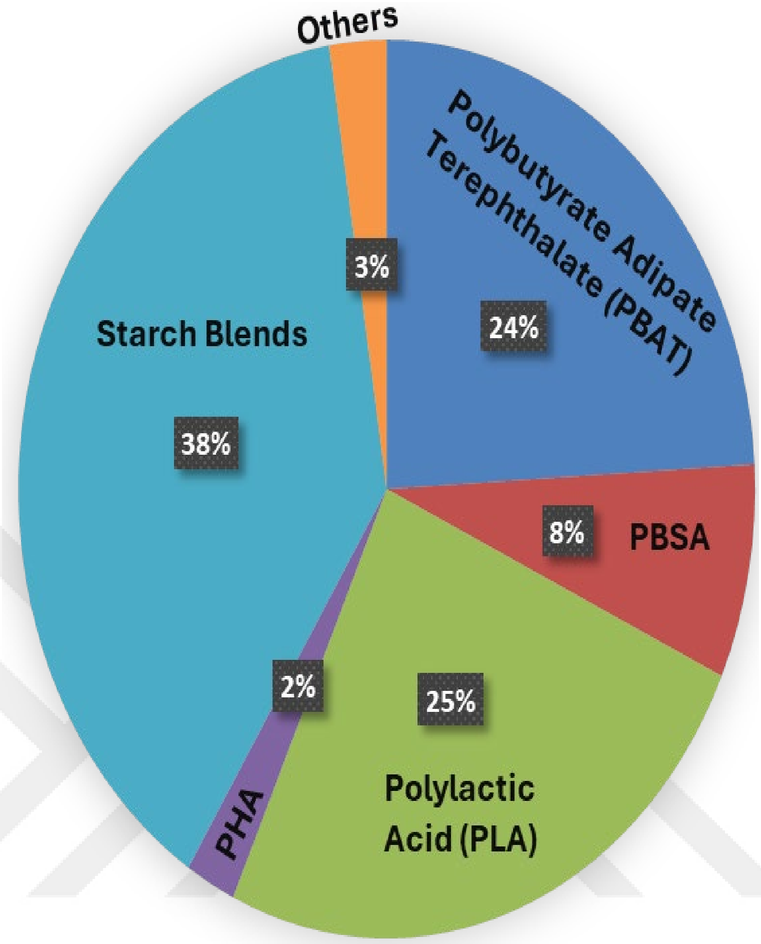

Figure 1.9. Distribution of biodegradable polymers by production capacity (Statista, 2021)

PLA already surpassed 290,000 tons of production in 2019 (Chellali et al., 2022). Moreover, the PLA market size is anticipated to grow dramatically, as seen in Figure 1.10. When the PLA market size is considered in Türkiye, the market size that is 17.7 million US $ in 2023 is anticipated to grow by 74% to 68.2 million US $ by 2030 (Horizon, 2023).

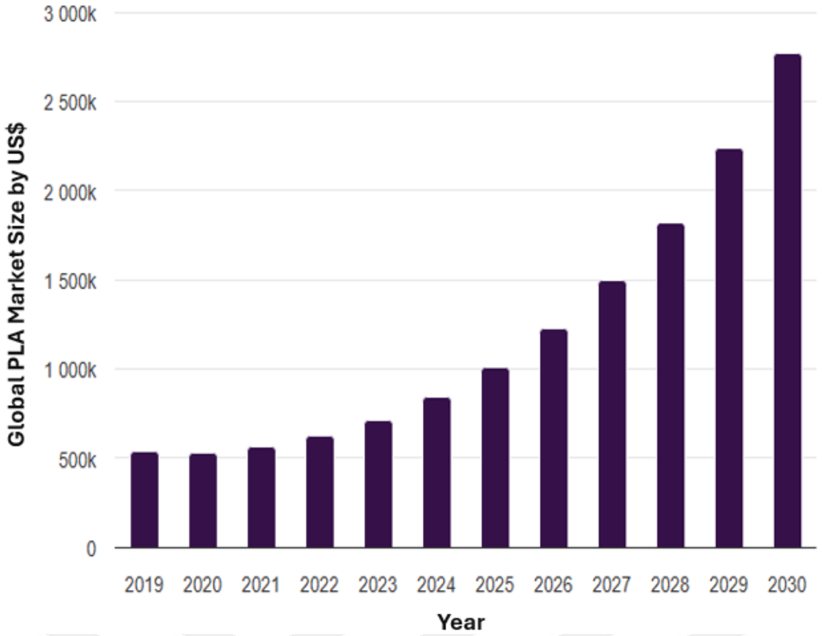

Figure 1.10. Global PLA market size (k:1,000) (Horizon, 2023)

Biodegradation is defined in various ways; for example, ASTM D 6400-99 defines it as a natural process occurring by microorganisms such as bacteria and fungi. (Luckachan & Pillai, 2011) whereas it can also be defined as a degradation process for which the end product achieved could be digested by microorganisms (Silva et al., 2023). In other words, if a polymer is decomposed or modified to decompose for a limited time into smaller fragments that microorganisms can digest, it is called a biodegradable bioplastic. The biodegradation of polymers takes place through two mechanisms. First is fragmentation, and the second is mineralization; when a polymer is exposed to those two processes, biodegradation occurs (Kržan, 2012). Kržan defined mineralization as a conversion of a polymer to inorganic substances such as CO_2 and fragmentation as a polymer undergoing chemical decomposition by being exposed to living or non-living conditions to achieve fragments (Kržan, 2012). Degradation essentially occurs with fragmentation followed by mineralization such that at the end, desired, functional smaller fragments that the metabolism of microorganisms could utilize are attained.

CHAPTER 2

POLYLACTIC ACID

Growing awareness of the need for a better, habitable, sustainable globe has already affected people worldwide to seek solutions to obstacles caused by different products used daily. Problems ranging from petroleum-based fuels to petroleum-based plastics will almost lead the planet to be inhabitable. Therefore, the behavior change concerning polymers, at least to diminish or slow down the adverse impacts, has resulted in attempts to replace non-biodegradable polymers with biopolymers such as PLA, as already mentioned in Chapter 1. Since PLA can be degraded into fragments not harming the environment and also can be produced by natural/renewable resources, it has become the focal point of biopolymers. As an alternative to non-biodegradable polymers, PLA is more admirable, and its utilization gains more popularity day by day. As a result, PLA-based studies focus on the improvement of the characteristics of the PLA degradation so that a material that is already biodegradable could be improved and utilized to fulfill any need that normally is provided by non-biodegradable polymers.

Polylactic acid, or shortly PLA, is made of repeating units of lactic acid or 2-hydroxypropanoic acid. A member of polyesters, PLA's fundamental and sole subunit is lactic acid, as seen in Figure 2.1 (Khouri et al., 2024). The discovery of PLA back in the 18th century by a Swiss chemist (Tyler et al., 2016). Following the invention of PLA, its first use was reported for medical applications for mending mandibular fractures in dogs (Tan et al., 2013). Afterward, PLA being extremely versatile, its applications went beyond biomedical applications since the 1700s. To better understand the physical, chemical, and mechanical properties and how PLA is synthesized, its monomer lactic acid (other names: α-hydroxypropanoic acid & 2-hydroxypropanoic) must be investigated specifically. Lactic acid has two active optical stereoisomers L(+) and D(-) (Jamshidian et al., 2010). Although lactic acid could be produced by chemical synthesis, because of the limitations to achieving the desired stereoisomer of L-lactic acid, fermentation is preferred in the industry. Besides, chemical synthesis is more costly than fermentation, so the economic feasibility of the production of lactic acid is even more challenging (Jamshidian et al., 2010).

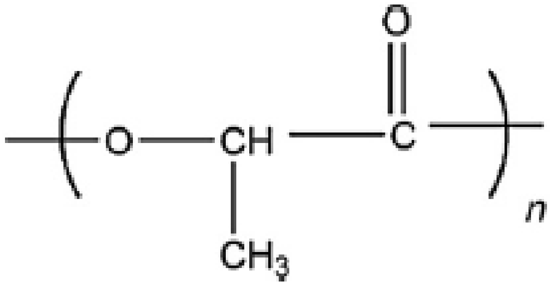

$$\left(O - \underset{CH_3}{\underset{|}{CH}} - \overset{O}{\overset{\|}{C}} \right)_n$$

Figure 2.1. PLA Structure (Tan et al., 2013)

Lactic acid’s bifunctional structure as can be seen in Figure 2.2, facilitates lots of vital properties to be utilized for itself and PLA, as well. Having both hydroxyl and carboxyl groups enables lactic acid to engage with a wide range of chemical reactions. Besides, whereas the hydroxyl group enables solubility in water and polar solvents, the carboxyl group also plays a vital role in the stabilization of the molecule by attraction with other molecules. (e.g., hydrogen bonding) Moreover, the carboxylic group could behave as a proton donor so that the molecule additionally acts as an acid. Having both of those functional groups ultimately ensures biofunctionality for lactic acid since some of the common amino acids, such as serine and threonine, possess both of those functional groups and are tremendously crucial to living beings since they are building blocks of proteins.

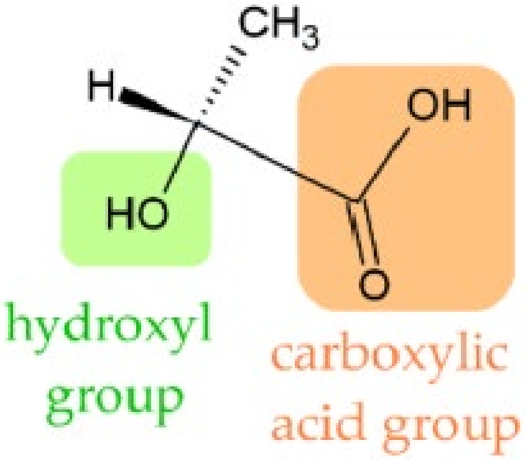

Figure 2.2. Bifunctional structure of lactic acid (Khouri et al., 2024)

PLA could be synthesized from renewable sources such as sugarcane, potatoes, and corn, and the synthesis takes place mainly through two mechanisms. The first route is the direct polycondensation of lactic acid, and the second is the ring opening (ROP) of already-produced lactide (Khouri et al., 2024). Figure 2.3 demonstrates the conventional paths for the synthesis of PLA. As mentioned above, lactic acid could be utilized to produce PLA; however, the molecular weight of the final product determines its value. The greater the molecular weight of the PLA produced, the higher the value of PLA. Therefore, the main aim is not just to produce PLA but also to produce PLA with high molecular weights. Considering the paths shown in Figure 2.3, each has pros and cons. Direct polycondensation of lactic acid results in mainly low molecular weight PLA because of the water produced in each polymerization step breaking down the polymer chains. To deal with the molecular weight problem, ROP was first demonstrated by Carothers in 1932; however, the first high molecular weight PLA was not achieved till 1954 when DuPont developed separation techniques for lactide purification (Khouri et al., 2024). Compared to direct polycondensation, ROP provides PLA with higher molecular weight mainly thanks to enabling greater control of the polymerization. As a result, although lactic acid is the monomer of PLA, lactide ROP is preferred more. One essential part of the ROP utilization is the possibility of the use of lactide to the PLA route before any step if lactide could be achieved via different methods other than the steps such as enzymatic polymerization or direct polycondensation of lactic acid.

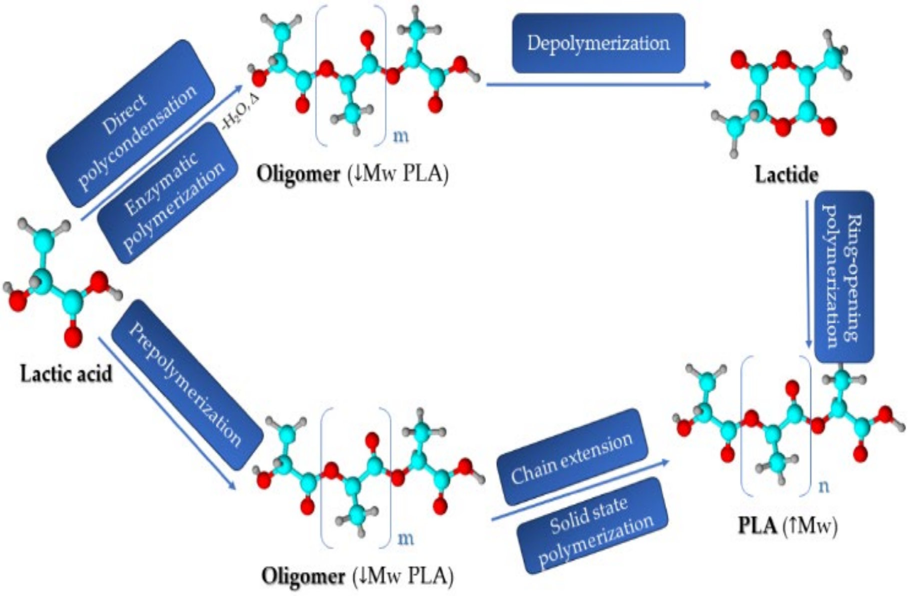

Figure 2.3. Traditional paths to produce PLA (Khouri et al., 2024)

Although ROP is the most preferred way of producing PLA, as mentioned earlier it has its cons so different methods have been studied to develop the best route to acquire PLA with the best characteristics depending on the application that PLA will be utilized. For example, a catalyst is mandatory for the ROP process, and depending on the catalyst used, different mechanisms, such as cationic, anionic, or coordination-insertion mechanisms, are involved (Dijkstra et al., 2011). Among those three mechanisms, study on metal complexes that could catalyze the polymerization of lactide via coordination-insertion mechanism has become extremely significant due to the fact that ROP by cationic mechanism has difficulty in acquiring high molecular weight PLA products, whereas the anionic mechanism lacks control over the molecular weight and molecular weight distribution of the final product, PLA (Dijkstra et al., 2011; Pang et al., 2010).

The coordination-insertion mechanism, mainly by metal alkoxides, as displayed in Figure 2.4, could be divided into 4 steps:

i. First step is the Lewis-acid metal center is occupied by the coordination of the lactide monomer,

ii. The second step is the nucleophilic addition of the lactide monomer into the metal-alkoxide bond,

iii. The third step is the acyl-oxygen splitting by the ring opening of the lactide monomer,

iv. The fourth step is the continuous insertion of lactide monomers,

Eventually, the polymerization reaction is ceased by hydrolysis of the active propagation chain (Dijkstra et al., 2011).

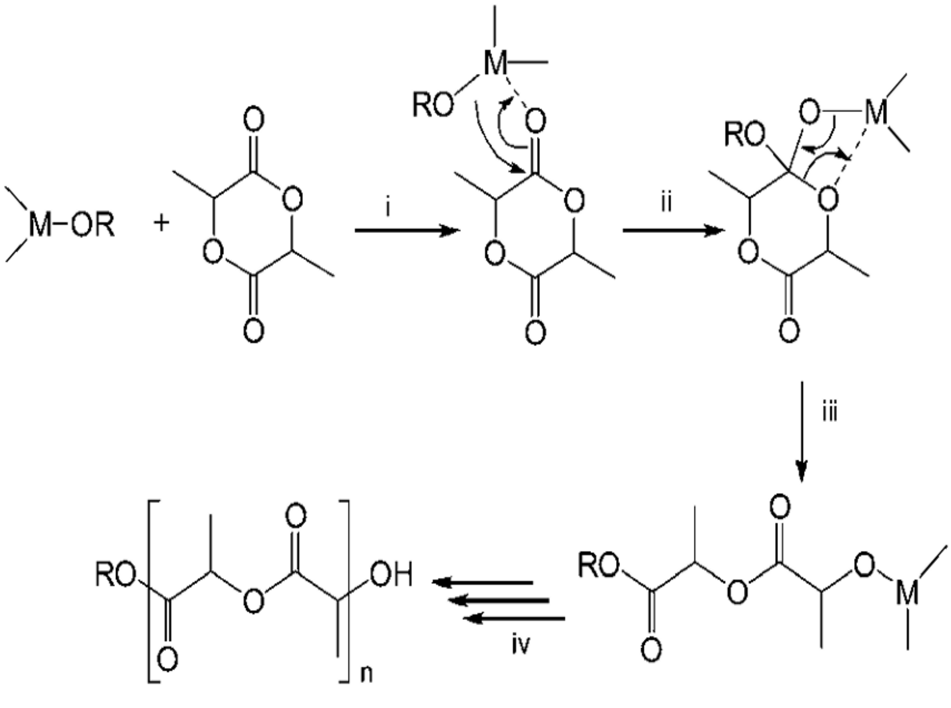

Figure 2.4. Coordination-insertion mechanism in the lactide ring opening (Dijkstra et al., 2011)

Having lots of information about PLA, it is important to grasp the main problems with PLA, which is as important as how PLA is synthesized. As mentioned earlier, especially in Chapter 1, PLA is one of the most promising bioplastics; however, its degradation depends on many different factors, as stated earlier. Thus, by attempting to replace or decrease the use of petroleum-based polymers, the suggested polymer, i.e., PLA, must not pose the same challenges to the environment such as PLA waste. In addition, the misconception of biodegradability indeed raises the potential of PLA waste all around the world. Therefore, the end-life treatment of PLA is as essential as replacing petroleum-based polymers with PLA.

Several methods have been developed for the end-life treatment of PLA to prevent any possibility of having PLA waste. Recycling of PLA could be divided into four main degrees: primary, secondary, tertiary, and quaternary (Sun et al., 2022). Those four categories include different methods and differ, especially in terms of the final product that the PLA is decomposed to. Figure 2.5 includes all the methods developed.

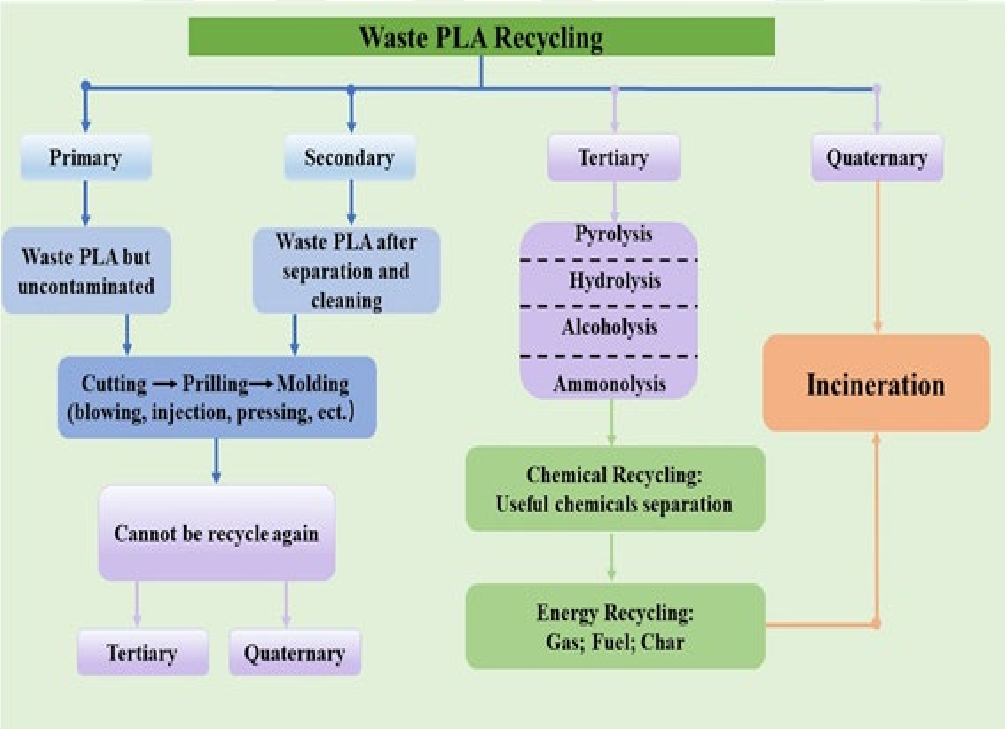

Figure 2.5. Levels of PLA recycling (Sun et al., 2022)

As Figure 2.5 implies, the primary and secondary levels of dealing with PLA waste especially is important when the primary goal is to reuse PLA; however, depending on the contamination degree this type of waste management is proceeding to be more challenging. Besides, the reusability of PLA by those two degrees of recycling is too limited (Up to 3 times most). After 3 times, the molecular weight of PLA decreases by 50% (Sun et al., 2022). Therefore, tertiary and quaternary levels of recycling become so important that most of the studies focus on improving the methods performed under these two categories. These two levels of recycling are also called chemical methods to recycle PLA.

Figure 2.6 summarizes and exhibits the paths to the final product when the above-mentioned chemical methods are applied. Each of these methods has some difficulties in application. For example, composting of PLA does not produce any intermediate product, and a substantial amount of CO_2 is produced which causes issues, especially in achieving sustainable recycling. Solvolysis which is known for both alcoholysis and hydrolysis has limitations in terms of the economic point of view due to expensive unit operation (Cho et al., 2023), and another problem is products must be separated from water, and alcohol. Moreover, crucially, the route to recover PLA back from fermentation is so costly that it accounts for 79% of the whole energy demand for PLA production (McKeown & Jones, 2020; Sun et al., 2022). As pointed out earlier in this chapter, a way to produce PLA from the ROP of lactide is promising, and it could be a cornerstone in waste management and economic feasibility in synthesizing PLA. Therefore, PLA pyrolysis as shown in Figure 2.6 provides a possibility to reach this goal and stands out as one of the most important paths to deal with the PLA waste problem that is about to occur.

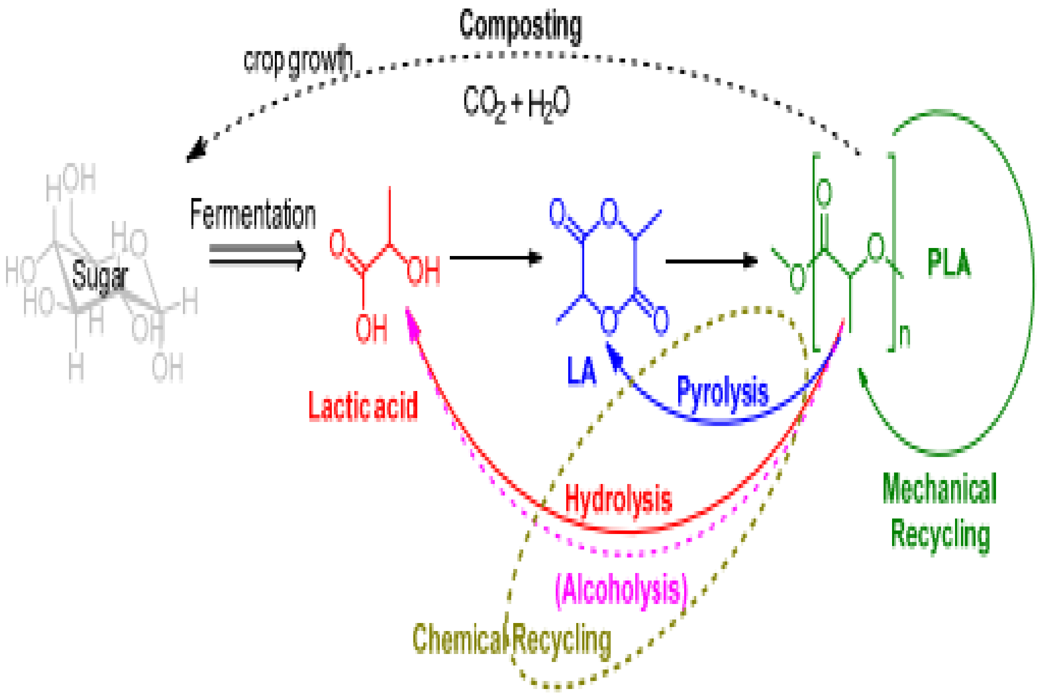

Figure 2.6. Methods to recycle PLA (McKeown & Jones, 2020)

2.1 PLA Pyrolysis

Pyrolysis is a process of decomposing material to its smaller molecules by means of thermal applications, i.e., heating under an inert medium. Depending on the temperature, heating rate, etc. the naming of the pyrolysis differs. There are three main types of pyrolysis: Fast, slow, and flash. Slow pyrolysis requires a heating rate of 0.1 to 0.8 °C/min with around 300 °C whereas fast pyrolysis requires a heating rate of 10 to 100 °C/min with around 400-700 °C of pyrolysis temperatures. On the other hand, flash pyrolysis has harsher conditions as 1000 °C/min of heating rate with 700-900 °C of pyrolysis temperatures (Hasan et al., 2021). Regarding PLA, pyrolysis happens mainly via two mechanisms:

1) Transesterification reactions
2) Free radical reactions

The transesterification arises through bite backing of carboxyl or hydroxyl groups on PLA chains to form $CH_3CH{=}O$, CO, lactide, and other sorts of cyclic products resembling lactide (Mcneill & Leiper, 1985). Through transesterification optical properties of PLA do not change, and the main products L-lactide and D-lactide are obtained (Kopinke et al., 1996). After pyrolysis exceeds around 270 ℃, free radical reactions start taking place (Fan et al., 2004). The main clear difference in observing whether free radical reactions started is the observation of the meso-lactide which is an optical isomer of L/D-lactide. Free radical reaction within PLA pyrolysis occurs mainly due to the cleavage of main chains within PLA which causes the formation of oxygen and carbon free radicals. Considering these two mechanisms mentioned, temperature and heating rate have the utmost importance in terms of the final product distribution.

Most of the studies so far have focused on fast pyrolysis of PLA. Therefore, slow pyrolysis of PLA, especially at milder conditions, has become extremely crucial in terms of both cost-effectiveness and the final product distribution. In addition, noncatalytic PLA pyrolysis occurs in a range of 306 to 384 ℃ (Sun et al., 2022). As a result, catalytic PLA pyrolysis becomes state-of-art in terms of both decreasing the PLA degradation temperatures and achieving the desired final product. Various studies have been reported on catalytic PLA pyrolysis so far. For example, Noda et al., in their study, showed that catalytic activity order for Sn, Al, Zn, Zr, and Ti followed as Sn > Zn > Zr > Ti > Al (Su et al., 2023). Moreover, Cam et al. demonstrated metals Sn, Zn, Al, and Fe, impact PLA pyrolysis behavior as well (Cam & Marucci, 1997). Another study (Mcneill & Leiper, 1985) showed that in the depolymerization of PLA, metal catalysts have the following impact: Fe > A1 > Zn > Sn. Eventually, a more recent study (Sivri, 2023) showed that metal-loaded silica aerogels have promising results. In the study, Mg, Al, and Fe loaded silica aerogels were examined, and the best activity in terms of condensable product achievement was obtained by Mg and Fe loaded silica aerogels whereas Al loaded silica aerogels favored non-condensable product distribution. Regarding mild pyrolysis conditions and a product such as lactide for ROP of lactide to be able to recycle PLA, catalysts, especially Fe and Mg loaded silica aerogels, showed highly promising results as no solid (PLA residual) around 250 ℃, and more condensable product achievement compared to Al based catalysts for 60 minutes of reaction time.

2.2 Silica Aerogel

Aerogels are famous materials with their outstanding properties, namely highly porous structures with high surface areas, exceptionally low density, and very low thermal conductivity (Hüsing & Schubert, 1998). As a result of these exclusive properties, they are in great demand for various applications such as thermal insulations (Koebel et al., 2012), pharmaceuticals, biomedical applications (Maleki et al., 2016), and catalysis (Choi & Suh, 2007; Maleki et al., 2016; Pajonk, 1999). Back in history, Kistler obtained the first aerogel using the method of supercritical drying in the 1930s (Maleki & Hüsing, 2018). Aerogels are solid materials that still preserve their early wet gel structure, which consists of a 3D porous web with a connection to pores that have micro and meso dimensions obtained by drying methods (Hüsing & Schubert, 1998). Besides, depending on the synthesis route, silica aerogel pore size might range from 5 to 100 nm, meaning that macro pores might also be available in silica aerogels (Gurav et al., 2010). Hence, they are attractive in the chemical industry, especially in the field of catalysts. Indeed, Kistler is the first person not only to discover the material itself but also to reveal its catalytic features by trying to convert organic acids to ketones. Later studies in the 1990s showed that aerogels could be used as catalysts in liquid-solid and gas-solid reactions specifically for a remedy to environmental issues such as removal of volatile organic compounds (VOCs) from the air and of toxic organics from water, CO_2 capture, and removal of heavy metal ions from wastewater (Choi & Suh, 2007; Pajonk, 1999). Having stunning architecture in terms of structure and an easily adaptable route of synthesis makes the aerogels a perfect fit for support material in catalysis (Pajonk, 1991; Schneider & Baiker, 1995).

2.3 The Aim of the Study

Polymers have been an essential part of life for a long time. The use of polymers is almost inevitable for most of the products used daily. However, proper management of the end life of the polymer products is still troublesome. Besides, most of the daily used polymers are petroleum-based polymers, which causes sustainability problems. Therefore, bioplastics to replace petroleum-based polymers are intended to be utilized. When bioplastics are in use, it is considered to degrade naturally so that management of waste problems can be easily handled. However, it is seen that although biodegradability is inherently embedded in bioplastics, the nature of degradation depends on several factors. Different bioplastics have different realms of uses. One of the bioplastics, PLA, has been very promising in terms of utilization as a bioplastics polymer to replace non-biodegradable petroleum-based polymers. However, PLA degradation depends on several factors such as temperature, pH, moisture content, molecular weight, etc., so if the medium lacks the proper conditions, PLA waste is also inevitable. Therefore, to improve PLA degradation, this study aimed to utilize bimetallic catalysts in the degradation reaction of PLA in the pyrolysis system. Moreover, high surface area and porous structure make silica aerogel promising for catalysis. Therefore, silica aerogel was selected to be the support material for the synthesized bimetallic catalysts. The study in summary aims the following:

∇ Synthesizing support material that is silica aerogel, and then loading metals into the synthesized silica aerogel

∇ Characterization of the synthesized catalysts via several characterization techniques to achieve information about the physical, and chemical properties of the catalysts

∇ Performing the activity tests of the catalysts in PLA degradation reaction both in TGA equipment and the pyrolysis system

∇ Investigating the effect of Al/Fe weight ratio on product yields, condensable, and non-condensable product distributions

- Observing the effect of temperature on the PLA degradation reaction on product yields, condensable, and non-condensable product distributions for the selected catalyst that shows the best performance in terms of achieving condensable product when the Al/Fe weight ratio is changed
- Observing the reaction time impact on product yields, condensable and non-condensable product distributions for the best-performing catalyst

CHAPTER 3

EXPERIMENTAL

Experiments in this study involve three categories: synthesis of support material and bimetallic catalysts, characterization of support material and bimetallic catalysts, and, lastly, testing the activity of the synthesized catalysts in depolymerization of PLA in the pyrolysis system.

3.1 Support Material

Support material, silica aerogel, is synthesized via the sol-gel method. The following chemicals are utilized: tetraethyl orthosilicate as a silicon source, ethanol, hexane, and distillled water as solvents, NH_3 as a basic catalyst, HCl as an acidic catalyst, NH_4F as a gelling agent, and finally TMCS as a surface modifier.

3.1.1 Silica Aerogel Synthesis

Silica aerogel synthesis is performed according to the procedure given by Sivri et al. (Sivri et al., 2019). First, 5 beakers, a bottle, and a 30 ml graduated cylinder are cleaned with soap, distilled water, and ethanol. After cleaning, all the mentioned items are dried in fumehood to discard any residual content. Upon the completion of the cleaning process, the bottle is placed into a balance (Sartorius BL 210 S) where the silica aerogel product is achieved, at the end. Necessary chemicals distilled water, ethanol (Sigma Aldrich), and tetraethyl orthosilicate (TEOS, Merck) are poured into beakers within the fumehood cautiously. Firstly, from the beakers prepared, 1.73 g distilled water is added to the bottle, followed by 5.64 g ethanol, 10.01 g tetraethylorthosilicate, and 62 µL of 1M hydrochloric acid (HCL, 37 v/v%, Merck) are added, respectively. This part of synthesis takes place at room temperature. Then, a magnetic stirring bar is placed into the bottle and a magnetic stirrer equipment is utilized for 2 hrs mixing of the mixture prepared within the airtight bottle. After 2 hrs of mixing, the magnetic stirring bar is removed from the mixture, and the bottle is inserted into the balance; 3.85 g distilled water and 9.92 g ethanol are added dropwise to the solution. Following that, 650 µL of 1M ammonia (NH_3, 25 v/v%, Merck) and then 800 µL of 1M ammonium fluoride (NH_4F, Merck) solutions are added to the solution dropwise while the mixture within the bottle is stirred with the idle hand. Adding NH_4F solution, gel formation is observed. With the help of a spatula, the gel within the bottle is cut into small pieces immediately. Later, ethanol that covers the whole gel is added to the bottle. This produced mixture (gel + ethanol) remains at room temperature for 8 hrs. After 8 hours, the next step is to filter the ethanol and replace it with 30 ml of hexane (Sigma Aldrich). Afterward, the gel and hexane mixture is put into a water bath that is kept at 45°C and is allowed to stay for 2 hrs. Later, 5 g of trimethylchlorosilane (TMCS, Merck), after filtering the hexane and adding 30 ml of hexane again, is added to the gel and hexane mixture dropwisely. At this point, HCl and water vapors are observed. Renewing hexane for the mixture, the mixture of gel and hexane is placed in a water bath which is kept at 45°C and is proceeded to remain for 5 hrs within the bath. 5 hrs later, 30 ml of hexane is renewed and is again allowed to remain in the water bath for another 5 hrs. Eventually, after 5 hrs pass, hexane is filtered and the gel is dried at 125°C for 2 more hrs. The whole process of synthesis takes 24 hours. Figure 3.1 shows the whole process as an illustration.

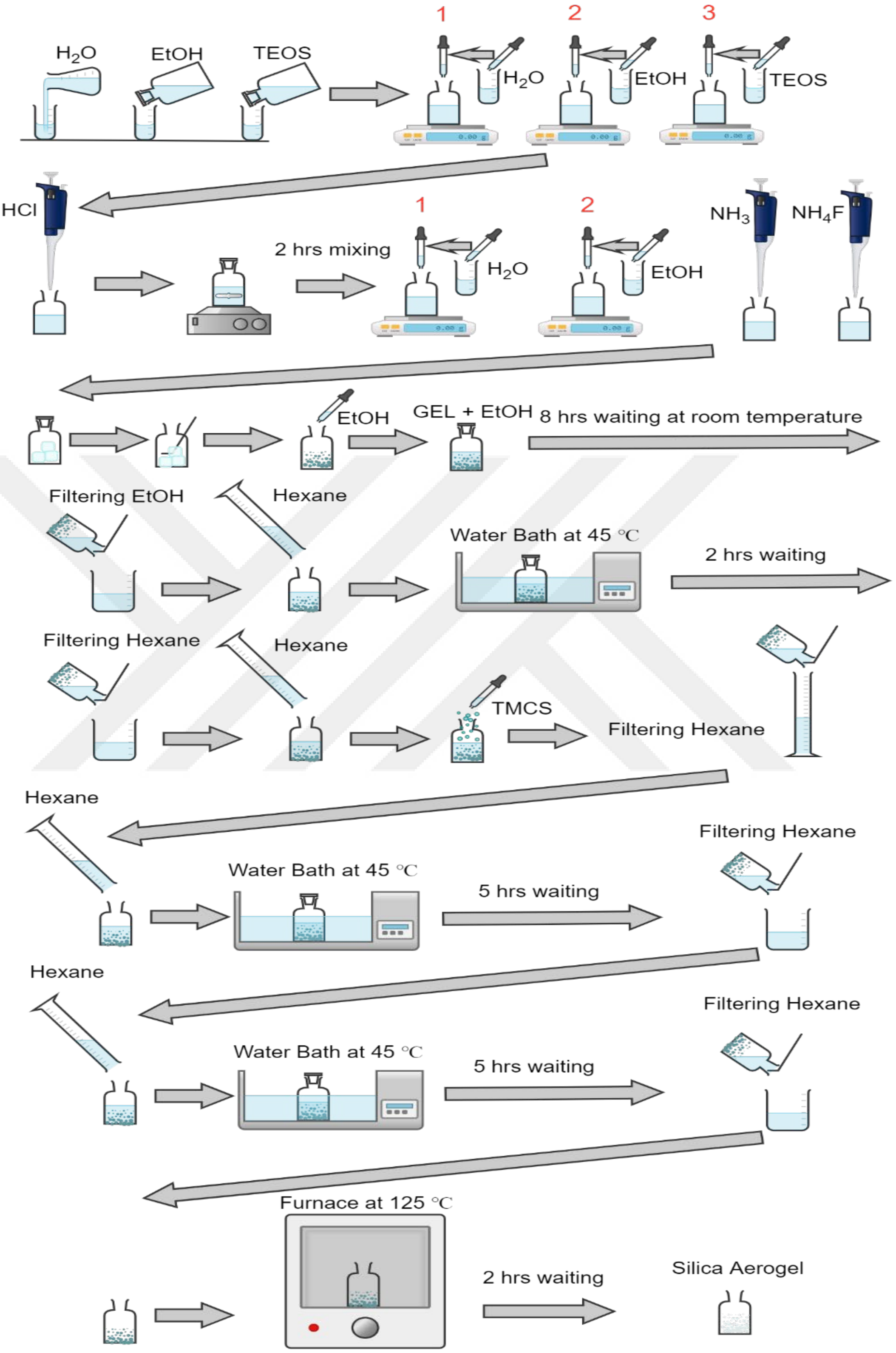

Figure 3.1. Silica aerogel synthesis steps

3.2 Catalyst Synthesis

All the catalysts were synthesized by using the wet impregnation method. Depending on the strategy followed, different catalysts could be synthesized. The support material, which is silica aerogel, might be calcined or uncalcined. Moreover, metal loading could be performed as two metals being loaded simultaneously, or one metal could be loaded, and then when the wet impregnation procedure is finished for the first metal, the second metal follows the same procedure as if the metal loaded silica aerogel is now the new support material. In addition, while loading the metals, as mentioned in the second case, the first metal-loaded silica aerogel could be calcined, and then the second metal could be loaded. Within the scope of this study, only uncalcined silica aerogel loaded simultaneously synthesized bimetallic catalysts, for which calcination was only performed after the bimetallic catalysts were synthesized, were considered. The details of the simultaneous synthesis of bimetallic catalysts are explained in the following subsection. To illustrate, Figure 3.2 shows the steps of simultaneous bimetallic catalyst synthesis using the wet impregnation method.

3.2.1 Simultaneous Synthesis

Bimetallic catalysts were synthesized by using wet impregnation via simultaneous synthesis. Following this procedure, 1 g of previously produced silica aerogel was powdered and poured into a beaker, after which 20 ml of ethanol (Sigma Aldrich) was poured into the same beaker. Later, depending on the weight percent of the metals that were used, precursors ($Fe(NO_3)_3*9H_2O$, Sigma Aldrich and $Al(NO_3)_3*9H_2O$, Sigma Aldrich) were weighed and poured into different beakers where 10 ml of ethanol was added to each beaker, respectively. Then, magnetic stirrer bars were put into these three beakers and were allowed to mix uniformly for 2 hrs on magnetic stirrer equipment (Heidolph MR Hei-Standard & Daihan Scientific MSH-20D). When 2 hrs of mixing was finished, firstly, the solution containing the metal with the lower weight percent was added dropwise to the silica solution without any abrupt mixing of the silica solution. Afterward, the second solution containing the higher weight percent metal was again added dropwise to the silica-first metal containing solution while mixing was kept continuing. This solution was kept mixing for 24 hrs. Finally, the magnetic stirrer bar was removed from the solution, and the solution was kept drying at 60℃ overnight in a furnace. Synthesized bimetallic catalysts were calcined under a helium medium at 500℃ for 12 hrs, for which the heating ramp is 1℃/min.

3.3 Naming of the Catalysts

The metal-loaded bimetallic catalysts were synthesized via the wet impregnation method. All the catalysts' support material is silica aerogel. The naming was performed in the following manner: SimSAUXYWZ, where SA stands for silica aerogel, and 'U' stands for silica aerogel being uncalcined. Within this scope, Y stands for the first metal, and X shows its percent in weight, whereas Z stands for the second metal, and W is again the weight percent of the second metal. Moreover, the prefix Sim stands for synthesis method being simultaneous. To demonstrate, SimSAU2Al13Fe means uncalcined silica aerogel was loaded with 2 wt.% of Al and 13 wt.% of Fe metals via the simultaneous synthesis method. Table 3.1 shows all the catalysts which were synthesized and utilized in the experiments.

Table 3.1 List of synthesized catalysts

Bimetallic Catalyst	***Metal Weight, %***	
	Al	**Fe**
SimSAU2Al13Fe	2	13
SimSAU1Al14Fe	1	14
SimSAU0.5Al14.5Fe	0.5	14.5

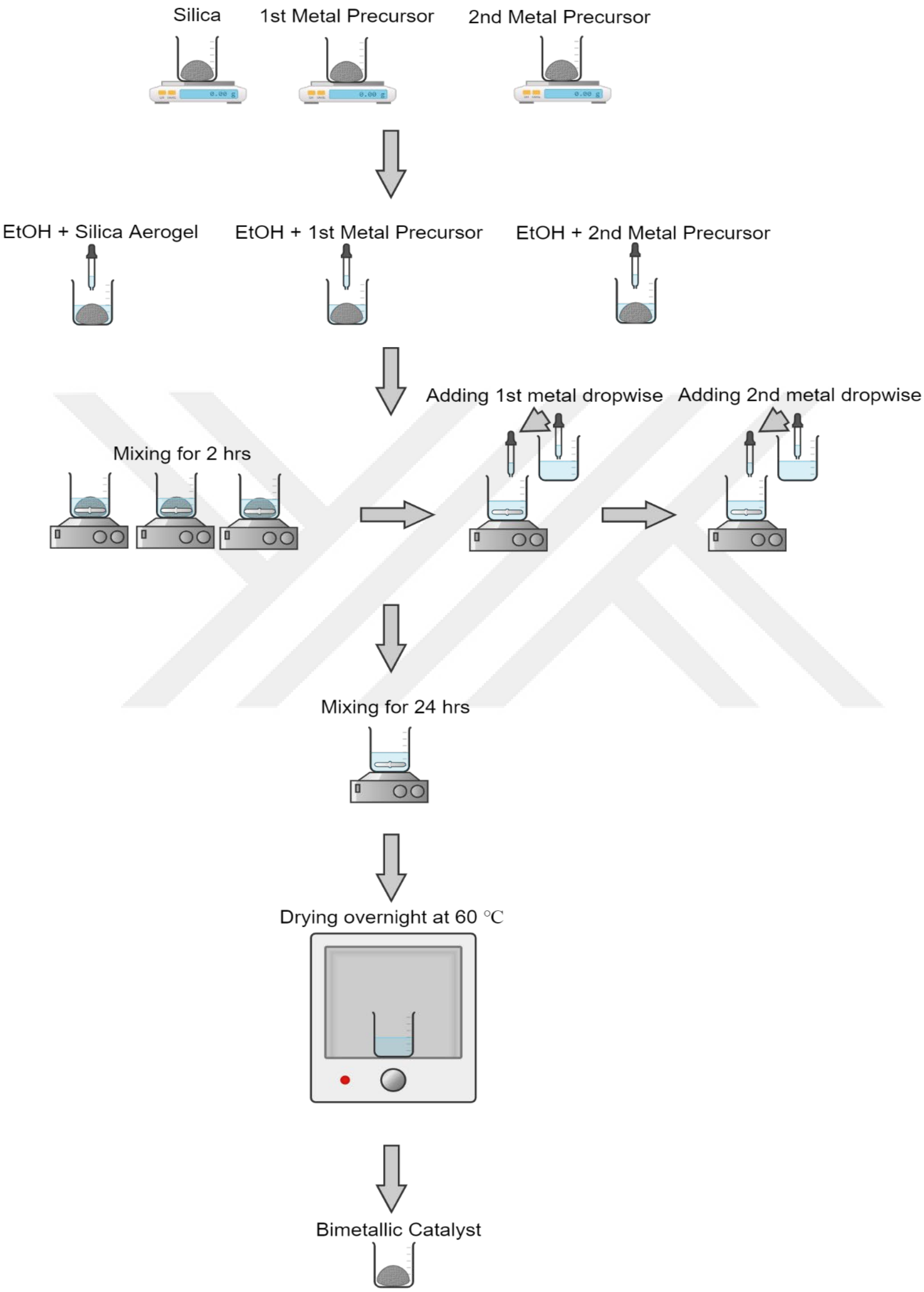

Figure 3.2. Bimetallic catalyst synthesis by using the wet impregnation method

3.4 Catalyst Characterization Techniques

Various characterization techniques were applied to both the bimetallic catalyst and the support material, silica aerogel. The information that could be achieved via performing these techniques is given in the following subsections.

3.4.1 Fourier Transform Infrared Spectroscopy

Fourier Transform Infrared Spectroscopy (FTIR), as one of the most utilized spectroscopy techniques, could provide information on the chemical properties of the material that is to be identified. Different elements, different bonding types, and different functional groups are absorbed at different frequencies. Therefore, the utilization of FTIR to realize the structural properties of silica aerogel and the bimetallic catalysts was performed. For the analyses conducted, 500 cm^{-1} to 4000 cm^{-1} wavenumber range with 64 scans and 4 cm^{-1} resolutions were used. The analyses were performed in the Perkin Elmer Spectrum Two device, which is in the METU Chemical Engineering Department.

3.4.2 X-ray Diffraction Analysis

Information about the crystallinity, phases, and complexes that are available within the bimetallic catalysts was obtained by using X-ray Diffraction Analysis (XRD) equipment with Cu anode, (Bruker D8 Advance), in the METU Department of Metallurgy and Materials Engineering. Bragg angle for characterization was determined by looking at the structures that might be available so that the range was accepted as 20˚-110˚ with a scanning rate of 1˚/min to get XRD patterns.

3.4.3 N_2 Physisorption Analysis

The nitrogen physisorption technique is commonly applied to materials for obtaining the material's surface area (Thommes & Cychosz, 2014). To be able to characterize adsorption/desorption isotherms, pore size distribution (PSD), pore volume, and surface area properties of the support and metal-loaded supports the Micromeritics Tristar II 3020 device at METU Department of Chemical Engineering was utilized. Samples to be inspected were degassed at 130℃ for 2 hours under vacuum before analysis was conducted. The relative pressure range (P/P_0) was from 0.0001 to 0.99.

3.4.4 Thermogravimetric Analysis

Thermogravimetric Analysis (TGA) is a technique by which a substance is exposed to heat in a controlled media. Utilizing TGA facilitates monitoring the change of the mass of the substance with time and/or temperature (PerkinElmer, 2010). TGA in essence could give an idea about thermal stability, oxidative stability, decomposition kinetics, moisture, and volatile content of the material to be inspected (Ryan & TA Instruments – Waters LLC, 2021). Therefore, within the scope of this study, analysis regarding activity testing of the catalysts with PLA, catalyst and support stability, and coke formation testing of the used catalysts were all performed by using TGA equipment (Thermogravimetric analyzer Shimadzu DTG-60H) in METU Chemical Engineering Department. Activity tests of the catalysts were performed from room temperature to 500℃ in nitrogen medium with 5℃/min ramp whereas stability tests and coke formation tests were performed from room temperature to 1000℃ in air medium with 10℃/min ramp.

3.4.5 Scanning Electron Microscopy

Scanning Electron Microscopy (SEM) could be performed in order to acquire information about morphology, particle size, dispersion of the particles, and the content of the sample to be observed (Wang et al., 2024). SEM is a vital technique, especially in terms of having an idea about the surface topography of the support and the metal-loaded support (i.e. Catalysts) (Değirmencioğlu, 2018). Therefore, SEM equipment (Supra 35VP LEO GEMINI) that is in Sabancı University was utilized to observe the surface morphology of the catalysts. Moreover, both the metal content of the catalyst on different regions by Electron dispersive X-ray spectroscopy (EDX) and the dispersion via mapping and backscattered electrons (BSE) were obtained. The samples, before being analyzed by SEM, all were covered with Au/Pd to provide conductivity for being able to interact with the electrons that are sent to the material to be inspected (Değirmencioğlu, 2018).

3.5 PLA Pyrolysis System

PLA pyrolysis was carried out under the Ar medium within the system, which is shown in Figure 3.3. All PLA pyrolysis experiments were conducted in an inert atmosphere provided by an argon tank with the control of flow via a mass flow controller (MFC). Argon gas was fed by MFC to a 100 ml stainless steel reactor of 8 cm height and 4 cm diameter. The reactor was heated by using a tube furnace that surrounded the reactor. The reactor temperature was controlled by a temperature controller, and a thermocouple that went inside the reactor was connected to the controller. The reactor outlet line was surrounded by heating tape to prevent any condensation inside the line. The temperature of the heating tape was controlled by another temperature controller. Following the reactor outlet line, three condenser vessels were installed. Besides, to ensure all the condensable products were collected, another condenser was integrated next to 3 condenser vessels. Whereas the first 3 condenser vessels were kept at 20°C with a water bath, the following last condenser vessel was cooled by circulating water that is at -5°C. Gas products were collected by utilization of a gas sampling bulb. Eventually, all the products (condensable or non-condensable) were analyzed using GC.

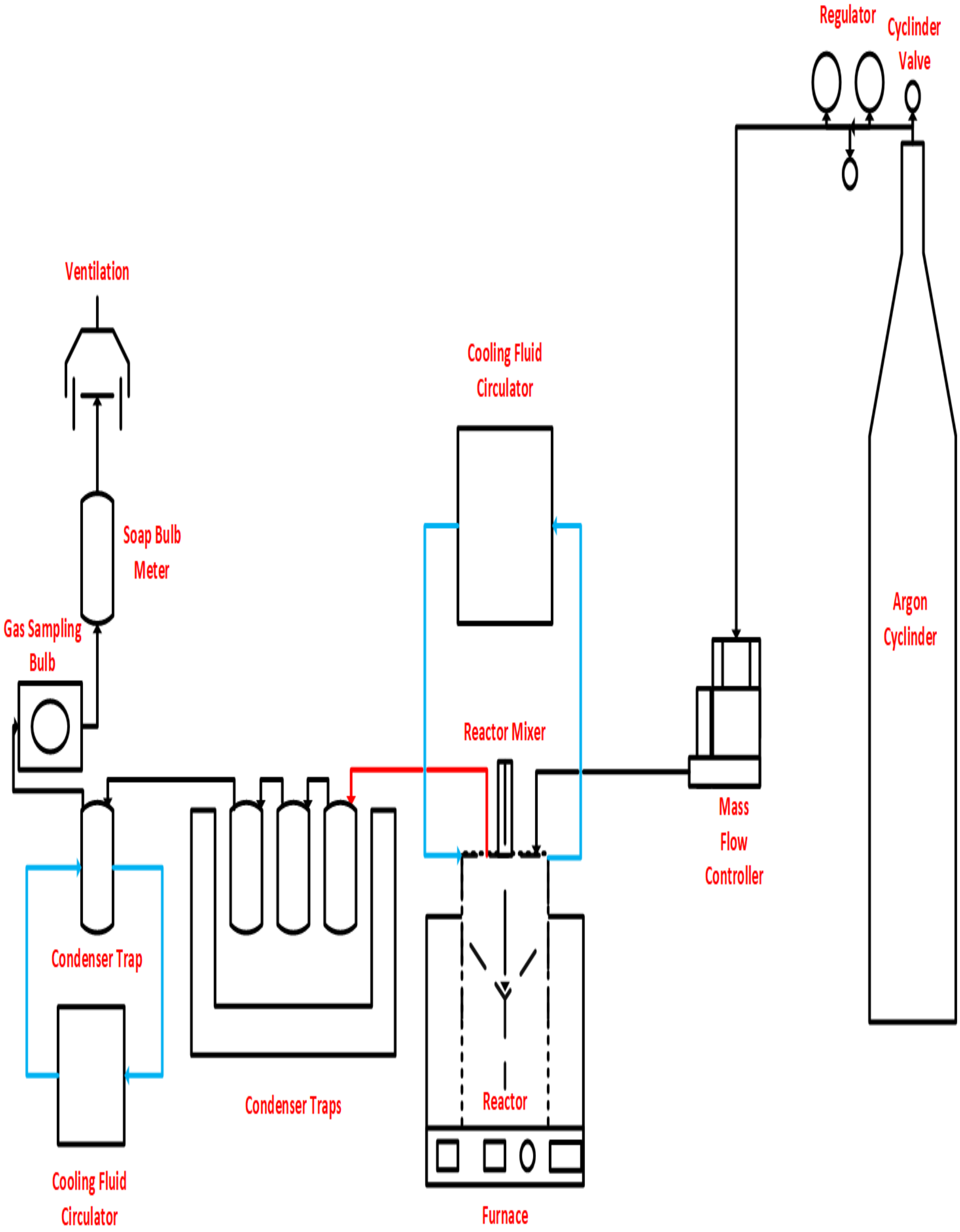

Figure 3.3. Pyrolysis System

3.5.1 Catalytic and Non-catalytic PLA Pyrolysis Experimental Procedure

2 g of PLA pellets (Natureworks,2003D) is placed into the reactor. For catalytic experiments, 1 g of bimetallic catalyst is placed on top of PLA pellets, whereas for non-catalytic experiments, only 2 g of PLA is utilized. 50 ml/min Ar flow is adjusted by an MFC, and the reactor outlet flow rate is measured by a soap bulb meter to ensure no leakage in the pyrolysis system. The heating rate is set to be 5℃/min by using the temperature controller that is connected to the tube furnace system. Reaching the desired temperature, the reaction is started. Temperature remains constant at the desired temperature during the reaction time, which is 60 minutes. However, besides 60 minutes duration of reaction, throughout the heating and cooling of the system furnace, reactor, heating tape temperatures, and flow rate data are collected every ten minutes. The gas leaving the reactor (effluent gas) is trapped within the gas sampling bulb for certain intervals, and the trapped gas is analyzed by the utilization of a GC. When the reaction finishes, the system is allowed to cool down. After cooling down, condensable products within the condenser vessels and the solid remaining within the reactor are weighed. Finally, collected condensable products are characterized using GC. Repeated experiments of PLA degradation in the pyrolysis system were conducted twice under the following conditions: 250℃ reaction temperature, 70rpm mixing rate, 60 minutes reaction time, ϑ_{Ar} = 50 ml/min, and without a catalyst.

3.6 GC Analyses of the Condensable and Non-condensable Products

The analyses of the condensable products were carried out by using Varian CP 3800 GC equipped with an FID detector and TRB-1 (Teknokrome) capillary column (30m x 0.25 mm x 0.25 μm). The capillary column is made of 100% dimethylpolysiloxane. Tables 3.2 and 3.3 display the GC conditions. For all the analyses, $1\mu L$ sample is injected into the column. Relative response factor values of lactide isomers ($C_6H_8O_4$, Sigma Aldrich), lactic acid ($C_3H_6O_3$, Sigma Aldrich) and propionic acid ($C_3H_6O_2$, Sigma Aldrich) were obtained based on reference acetone.

Table 3.2 Condensable product GC analysis condition

	Temperature (℃)	**Pressure (psi)**	**Flow rate (ml/min)**	**Carrier gas**
FID	275	-	32	Helium
Column	125-200	5	0.3	Helium

Table 3.3 Condensable product GC column temperature program

Temperature (℃)	**Hold duration (min)**	**Heating rate (℃)**	**Split ratio**
125	20	-	100
150	5	5	100
200	5	5	100

The analyses regarding non-condensable products were performed in Shimadzu GC-2010 Plus CP3800 GC equipped with a TCD detector and SUpelco capillary column (30m x 0.53 mm). 0.25 ml sample was injected into the column in each analysis. The calibration gas contains hydrogen, carbon monoxide, carbon dioxide, methane, and ethylene with 1 mol%. The balance was argon. Acetaldehyde was also calibrated. By analyzing the calibration gas, beta factors and retention times of the components were determined. Tables 3.4 and 3.5 exhibit GC conditions.

Table 3.4 Non-condensable product GC analysis condition

	Temperature (℃)	**Pressure (psi)**	**Flow rate (ml/min)**	**Carrier gas**
TCD	250	4.6	108	Argon/Helium
Column	40-250	-	5	Argon/Helium

Table 3.5 Non-condensable product GC column temperature program

Temperature (℃)	**Hold duration (min)**	**Heating rate (℃)**	**Split ratio**
40	7.5	-	20
250	14	23	20

CHAPTER 4

RESULTS AND DISCUSSION

Throughout this chapter, results that demonstrate the catalytic activity of the metal-loaded silica aerogels in the PLA degradation reactions and the material properties of those catalysts are shown. Material properties were tested by utilizing various characterization techniques that are mentioned in Chapter 3. Catalytic activity was also tested beforehand in TGA equipment.

4.1 Characterization Results of the Catalysts

Support material and the metal-loaded support materials, i.e., bimetallic catalysts, were characterized for acquiring properties such as morphology, porosity, the thermal stability of the support material, the structure of the material, etc., by the following characterization techniques: N_2 Physisorption, Thermogravimetric Analysis, Fourier Transform Infrared Spectroscopy, Scanning Electron Microscope Analysis, X-ray Diffraction Analysis.

4.1.1 Support: Silica Aerogel

Support material, i.e., silica aerogel physical properties, were determined by utilizing the above-mentioned characterization techniques.

4.1.1.1 Fourier Transform Infrared Spectroscopy Results

Figure 4.1 demonstrates the peaks corresponding to different bondings that are available in synthesized uncalcined silica aerogel. Peaks at 549 cm^{-1}, 799 cm^{-1}, and 951 cm^{-1} correspond to Si-O stretching vibration. 691 cm^{-1}, 758 cm^{-1} are for Si-O-Si stretching whereas peaks at 845 cm^{-1} and 1257 cm^{-1} are for Si-C stretching. On the other hand, C-H stretching, that is because of TMCS modification, was obtained at 2968 cm^{-1}. Eventually, the sharp peak around 1062 cm^{-1}, followed by a smaller broader peak around 1162 cm^{-1}, belongs to Si-O-Si stretching. These findings agree with what is found by Sivri et al. (Sivri et al., 2019) and also agree with the literature that the synthesized uncalcined silica aerogel possesses the structure of acknowledged silica aerogel that is in literature (Al-Oweini & El-Rassy, 2009; Wu et al., 2018). Therefore, the silica aerogel produced was synthesized successfully.

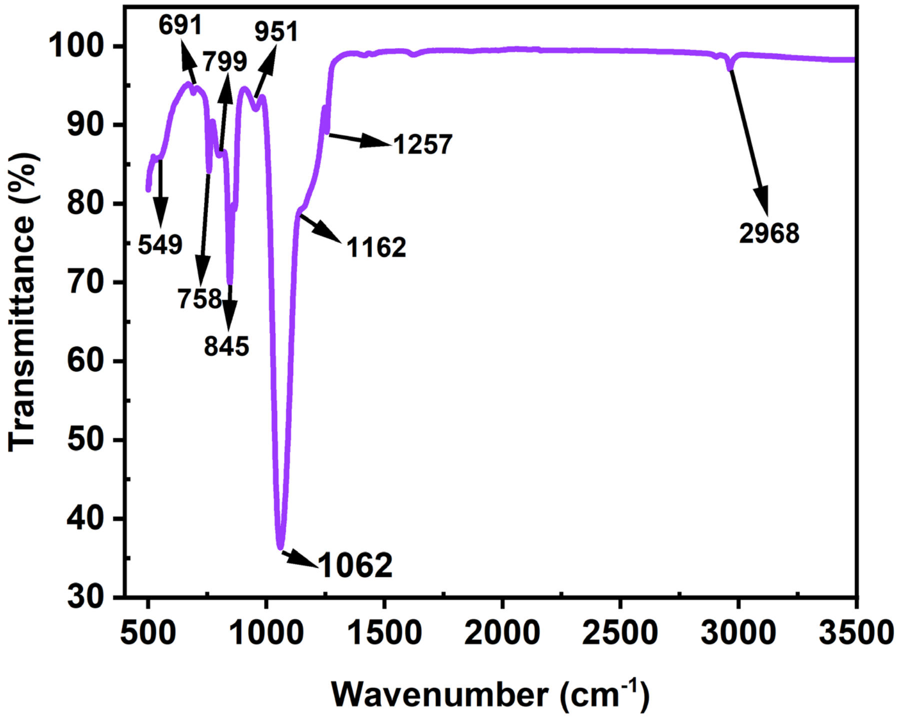

Figure 4.1. FTIR spectrum of uncalcined silica aerogel

4.1.1.2 N_2 Physisorption Analysis Results

All the bimetallic catalysts were synthesized by using porous silica aerogel as a support material. Silica aerogels, which were synthesized at different times, were characterized by performing N_2 Physisorption Analysis. Figure 4.2 shows nitrogen adsorption/desorption isotherms of SAU1, SAU2, SAU3, SAU4, SAU5, and SAU6 that stand for uncalcined silica aerogels of different batches. All six samples showed Type IV isotherm according to IUPAC classification (Clair & Ruelle, 2009) with hysteresis. Different batches showed hysteresis at P/P_0 values very close to each other and exhibited H3-type hysteresis. In terms of P/P_0 values where hysteresis began, 0.65, 0.65, 0.64, 0.66, 0.66, and 0.66 of relative pressures were obtained for SAUs of different batches, respectively. Accordingly, the synthesized silica aerogels displaying Type IV isotherm means a mesoporous material was produced.

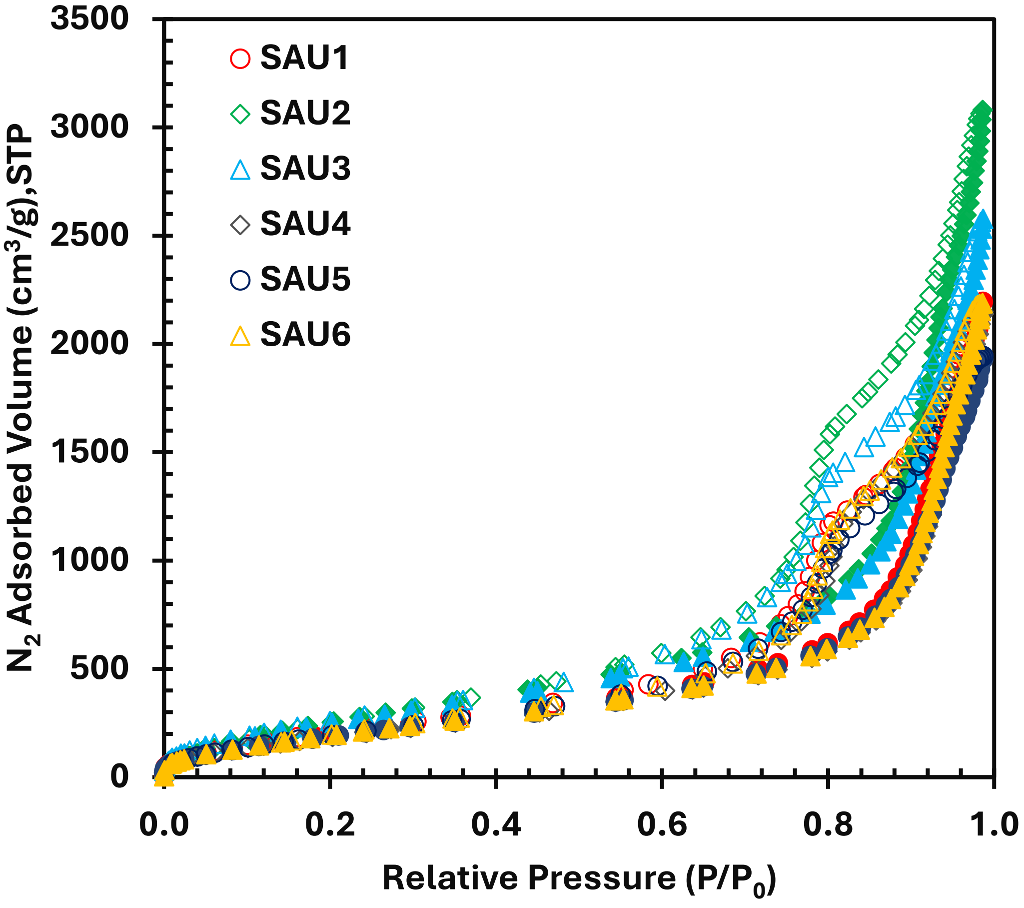

Figure 4.2. N_2 adsorption/desorption isotherms regarding silica aerogels of different batches (Filled symbol: adsorption branch, empty symbol: desorption branch)

Figure 4.3 displays the pore size distribution of the silica aerogels synthesized at different times. As can be seen in Figure 4.3, pore size distribution peaks around 10 nm; however, pores of different sizes ranging from 1 to 100 nm were also available for those samples. Peaking around 10 nm shows the mesoporous structure of the samples as anticipated from Figure 4.2. Nevertheless, since pore sizes other than the range of 2 to 50 nm were available within the materials, macropores (pores having diameter > 50 nm) and micropores (pores having diameter < 2nm) (Lowell, 2004) were also available beside the mesopores. Thus, it could be inferred that synthesized silica aerogels bear micro, meso, and macro pores at the same time, and pore size distribution is compatible with the adsorption/desorption isotherms shown in Figure 4.2.

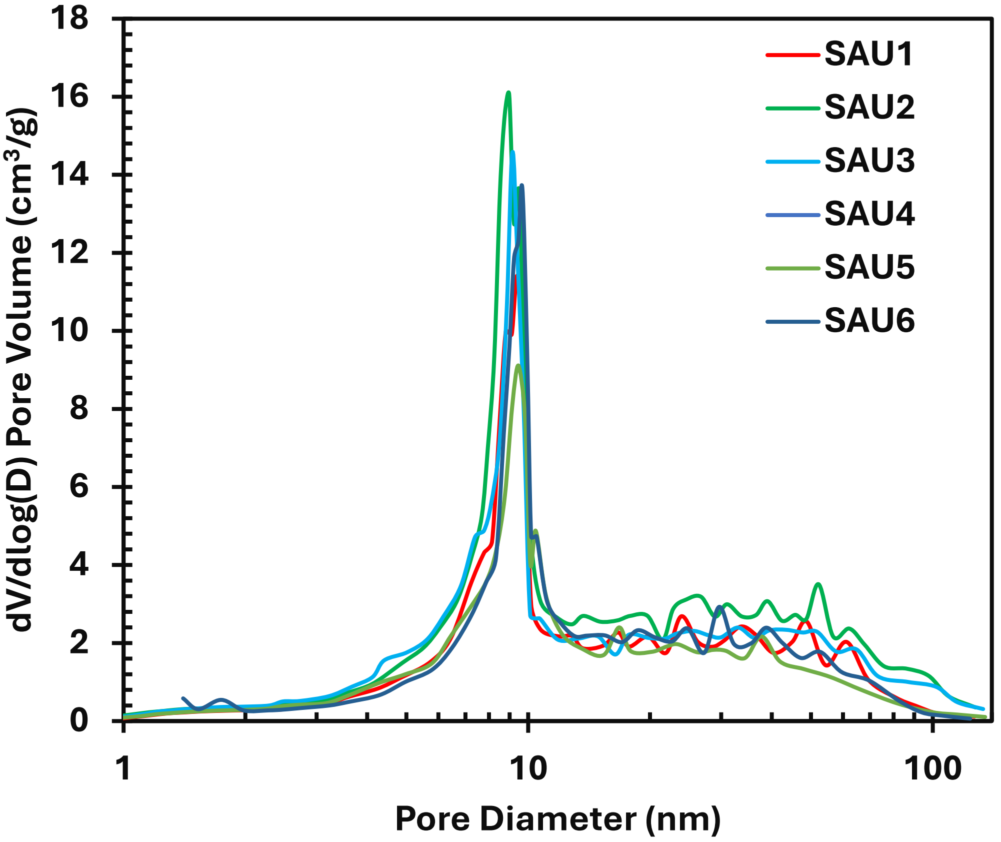

Figure 4.3. Pore size distribution of silica aerogels of different batches

As displayed in Table 4.1, multipoint BET surface area values ranged from 833 to 1090 m^2/g, BJH desorption pore volume values ranged from 3.01 to 4.77 cm^3/g, BJH desorption average pore diameters ranged from 9.0 to 10.4 nm with microporosity ranging from 3.00 to 4.21 % for the produced silica aerogels of different batches. Standard deviations were found to be ∓123.4 for multipoint BET surface area, ∓0.58 for BJH desorption pore volume, ∓0.5 for BJH desorption average pore diameter and ∓0.41 for microporosity, respectively. The data shown in Table 4.1 is compatible with the isotherms and the pore size distribution. Besides, the pore diameter of the synthesized aerogels showed that synthesized silica aerogels are mesoporous materials. Eventually, small standard deviations shown in Table 4.1 mean that silica aerogel synthesis is repeatable.

Table 4.1 Properties of synthesized uncalcined silica aerogels

Uncalcined Silica Aerogel of Different Batches	Multipoint BET Surface Area (m^2/g)	BJH Desorption Pore Volume (cm^3/g)	BJH Desorption Average Pore Diameter (nm)	Microporosity (%)
SAU1	833	3.40	9.7	3.65
SAU2	1090	4.77	9.6	3.00
SAU3	1042	3.99	9.2	3.84
SAU4	793	3.33	10.4	3.88
SAU5	793	3.01	9.0	4.21
SAU6	813	3.40	10.01	3.88
Average	894∓123.4	3.65∓0.58	9.66∓0.5	3.74∓0.41

4.1.1.3 Thermogravimetric Analysis (TGA) Results

Figure 4.4. displays the weight loss (%) by temperature change. There is too small around 2 % weight loss before 100 ℃, that might be because of the moisture within the silica aerogel material. However, after 100 ℃, till around 330 ℃, almost no change was observed related to the weight loss. Then, after 330 ℃, another decay in weight loss begins with a very small slope until 1000 ℃, where the analysis stops. In the end, around 13 % weight loss was observed. The loss after 330 ℃ is anticipated to be because of the main methyl groups leaving, followed by minor ones that are in silica aerogel with the TMCS modification (Ermiş, 2022). Considering TGA results, the calcination temperature for the metal-loaded silica aerogels was selected as 500 ℃.

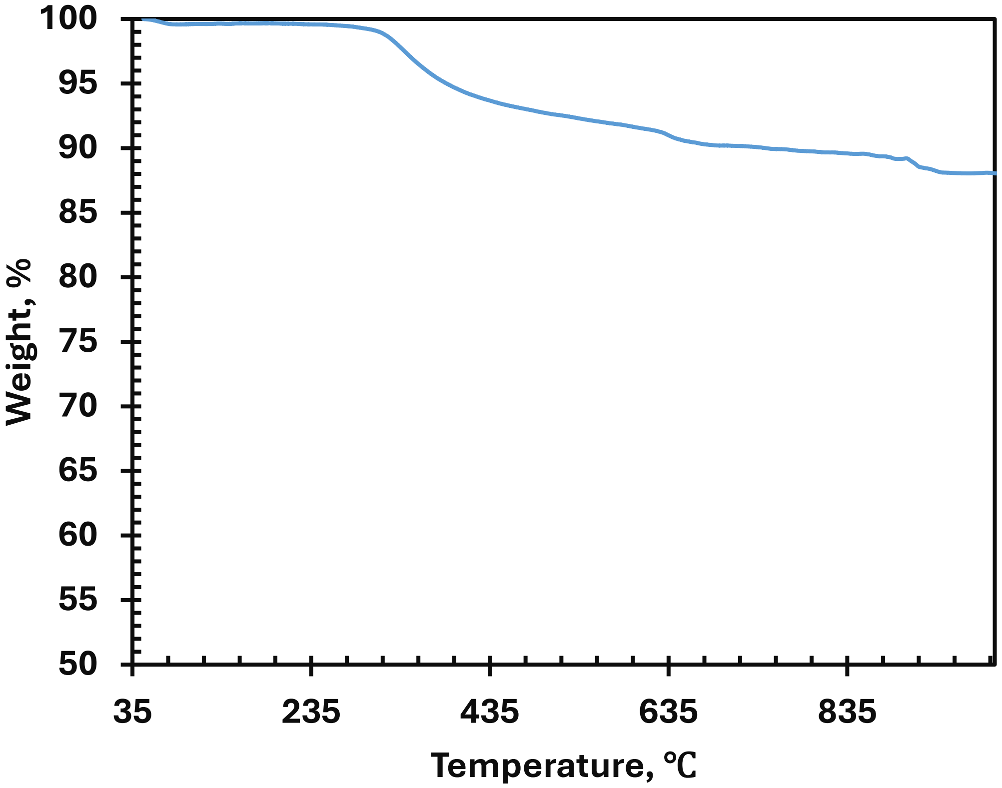

Figure 4.4. TGA result of uncalcined silica aerogel under air medium

4.1.2 Metal Loaded Silica Aerogel

Aluminum and iron (Al & Fe) loaded silica aerogel bimetallic catalysts were characterized by the following three characterization techniques.

4.1.2.1 N2 Physisorption Analysis Results

Figure 4.5 demonstrates the results obtained for metal-loaded silica aerogels (SimSAU2Al13Fe, SimSAU1Al14Fe, and SimSAU0.5Al14.5Fe) after calcination by utilization of N_2 physisorption characterization. Metal-loaded silica aerogels showed Type IV isotherm, indicating that the mesoporous structure of the silica aerogel was conserved. Comparing the average silica aerogel properties mentioned in Table 4.1, metal loading to silica aerogel support decreased the capacity that the material could adsorb (Figure 4.5). A decrease in N_2 adsorbed volume with metal loading was due to the fact that the pores of the support material were filled with the loaded metals. Moreover, in the hysteresis loop, whereas it was H3 type for SAU, a shift to H1 was observed after the metal loading for all the cases, and hysteresis started around 0.44 of P/P_0. The shift in hysteresis from 0.65 (SAU) to 0.44 exhibits a decrease in pore diameter. Moreover, the change from H3 type to H1 type also means the pores are narrower compared to silica aerogels. Lastly, it was observed that the SimSAU1Al14Fe catalyst's N_2 adsorption capacity, as can be seen in Figure 4.5, is lower than both SimSAU2Al13Fe and SimSAU0.5Al14.5Fe catalysts.

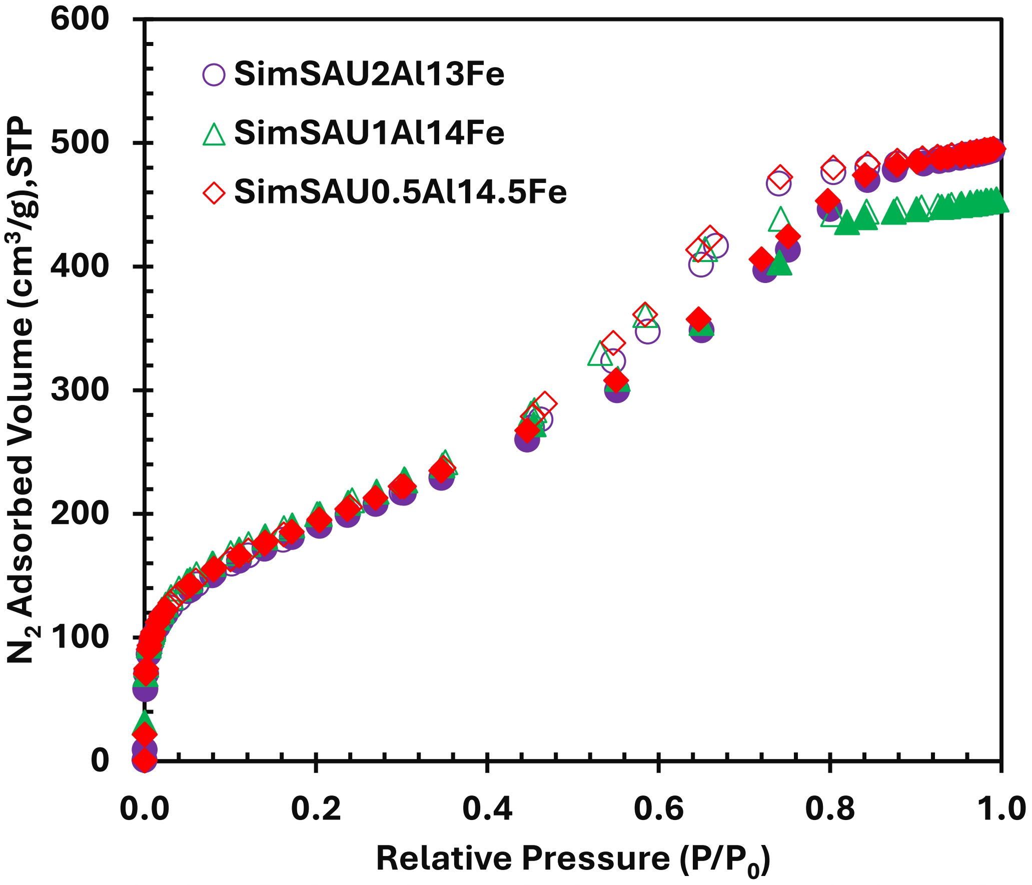

Figure 4.5. N_2 adsorption/desorption isotherms regarding metal-loaded silica aerogels (Filled symbol: adsorption branch, empty symbol: desorption branch)

Shrinkage on the pore sizes, as Figure 4.5 implies, could also be inferred from Figure 4.6. While support silica aerogel's pore size distribution peaks around 10 nm, metal-loaded silica aerogels' pore size distribution peaks around 3.4 to 5.1 nm, which implies loading of the metals to the support blocked the meso and macro pores within the structure. BJH desorption average pore diameter for silica support is 9.66 nm, whereas for the metal-loaded silica aerogels (SimSAU2Al13Fe, SimSAU1Al14Fe, and SimSAU0.5Al14.5Fe) are 3.02, 2.68, and 2.98 nm, respectively.

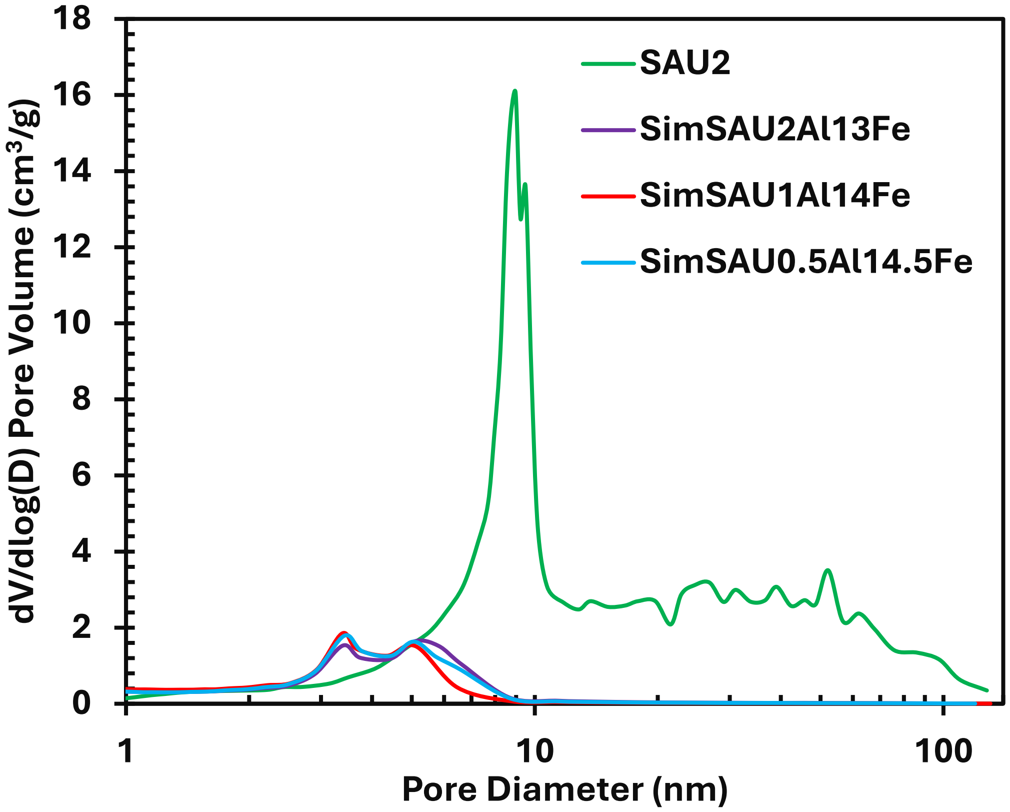

Figure 4.6. Pore size distribution of silica aerogel and metal-loaded silica aerogels

Figure 4.7 exhibits the pore size distribution of only the catalysts (SimSAU2Al13Fe, SimSAU1Al14Fe, and SimSAU0.5Al14.5Fe). As can be seen, the pore size distribution of all the synthesized catalysts looks very similar. Moreover, the average BJH pore size was improved by 2 times by increasing the time of mixing and having 10 minutes between each 3 ml of impregnation of the metal to be loaded.

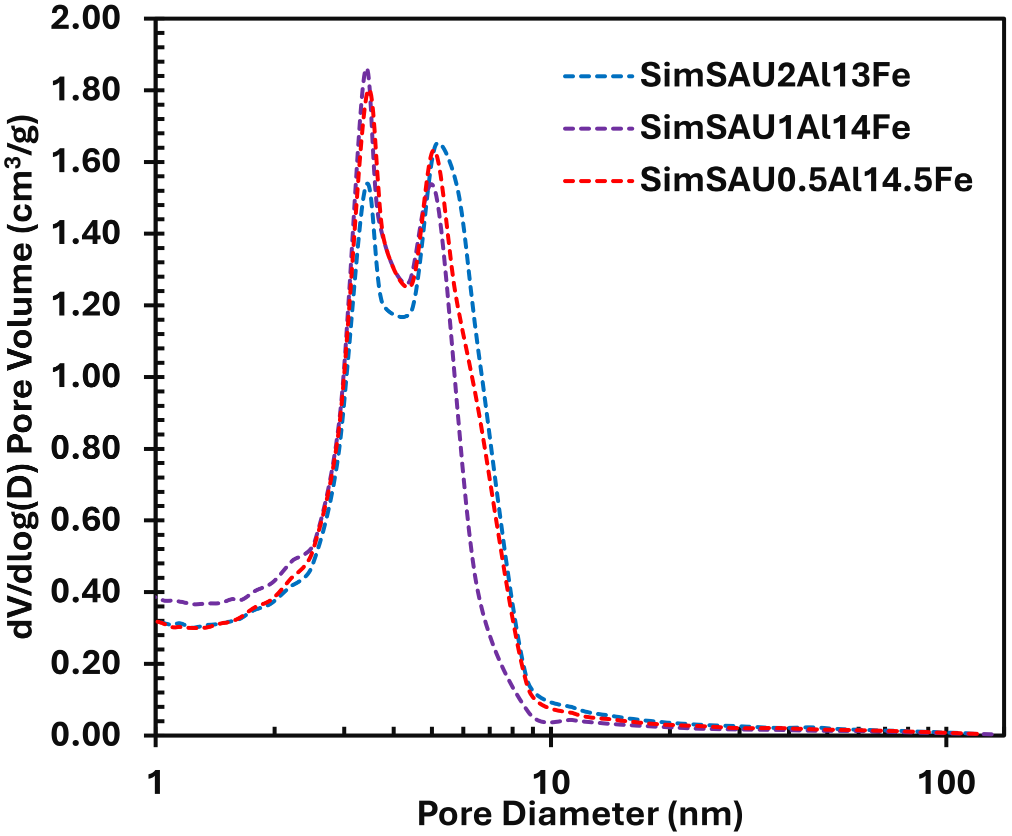

Figure 4.7. Pore size distribution of metal-loaded silica aerogels

As displayed in Table 4.2, multipoint BET surface area values ranged from 678 to 695 m^2/g, BJH desorption pore volume values ranged from 0.73 to 0.79 cm^3/g, BJH desorption average pore diameters ranged from 2.7 to 3.0 nm with microporosity ranging from 20.51 to 23.84 % for the metal-loaded silica aerogels of different Al/Fe weight ratio. The data shown in Table 4.2 is compatible with the isotherms and the pore size distribution. Besides, the pore diameter of the metal-loaded silica aerogels showed that metal-loaded silica aerogels conserved silica aerogels' mesoporous structure.

Table 4.2 Properties of synthesized metal-loaded silica aerogels

Metal-Loaded Silica Aerogels of Different Al/Fe Weight Ratio	**Multipoint BET Surface Area (m^2/g)**	**BJH Desorption Pore Volume (cm^3/g)**	**BJH Desorption Average Pore Diameter (nm)**	**Microporosity (%)**
SimSAU0.5Al14.5Fe	695	0.79	2.9	21.19
SimSAU1Al14Fe	688	0.73	2.7	23.84
SimSAU2Al13Fe	678	0.78	3.0	20.51

4.1.2.2 X-ray Diffraction Analysis Results

XRD results were obtained for aluminum and iron loaded silica aerogel bimetallic catalysts. All the investigated catalysts were synthesized via the simultaneous wet impregnation method. XRD patterns of the SimSAU2Al13Fe, SimSAU1Al14Fe, and SimSAU0.5Al14.5Fe catalysts were displayed with red, green, and purple lines in Figure 4.8. Peaks at 2θ values correspond to 24°, 33°, 35°, 43°, 54°, 57°, 62°, and 64° belong to Fe_2O_3 (Table A.3 in Appendix A). Peaks at 2θ values correspond to 30°, 35°, 43°, 57°, and 62° belong to Fe_3O_4 (Table A.4 in Appendix A). Thus, XRD patterns of the synthesized catalysts displayed that there are Fe_2O_3 and Fe_3O_4 phases within the catalysts.

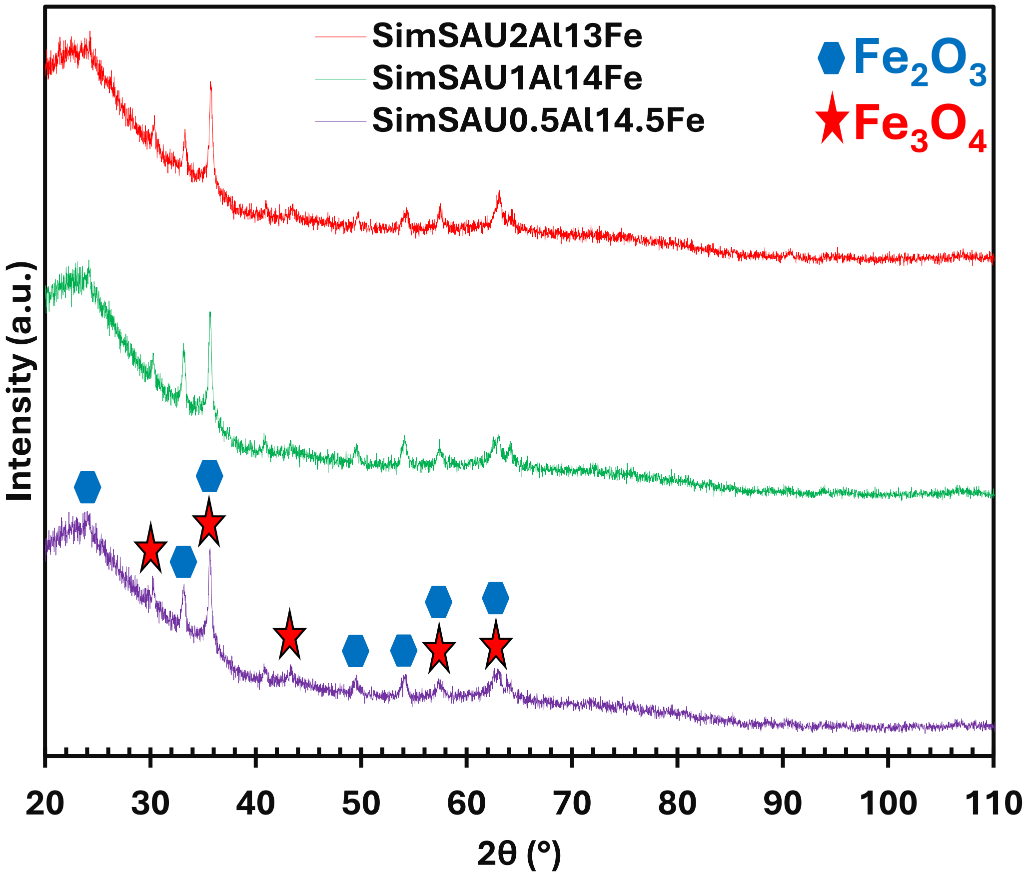

Figure 4.8. XRD patterns of bimetallic catalysts

4.1.2.3 Scanning Electron Microscopy Results

SEM was used to observe the surface morphology of the synthesized catalysts. For 20.00 kV HV and 100,000 x magnification, the images of bimetallic catalysts shown in Figure 4.9 were obtained. The porous structure of silica could be seen in all cases proving the morphology of the support was conserved though metal loading to silica aerogel supports was performed.

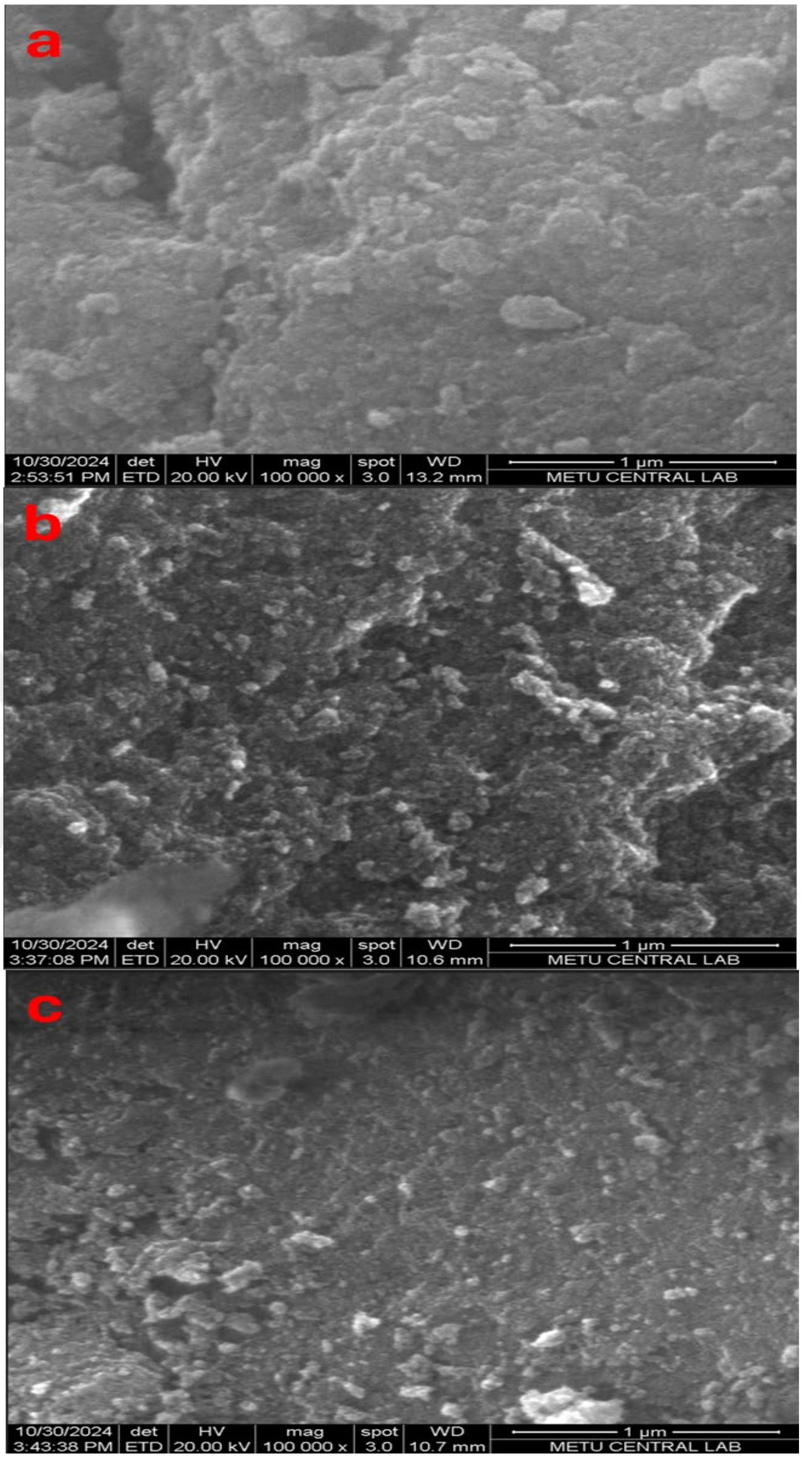

Figure 4.9. SEM images of synthesized bimetallic catalysts: a) SimSAU2Al13Fe, b) SimSAU1Al14Fe, and c) SimSAU0.5Al14.5Fe

Elemental composition regarding the species (Al, Fe, Si, and O_2) available in the SimSAU2Al13Fe catalyst is shown in Figure 4.10 for two different regions in the catalyst. EDX spectra of the synthesized catalysts are given in Appendix B. There is too small difference between these two regions in terms of both aluminum and iron content.

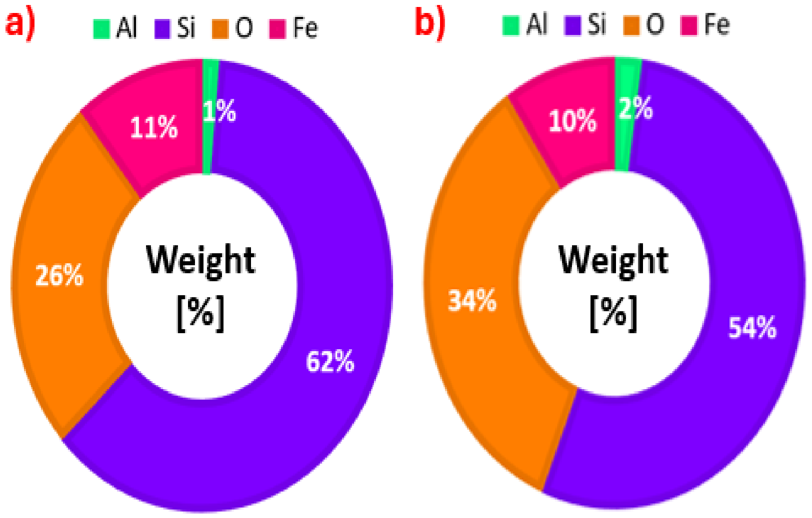

Figure 4.10. Elemental composition of the SimSAU2Al13Fe catalyst from different regions: a) Region 1, and b) Region 2

Elemental mapping of the catalysts was utilized to confirm the loading of the metals and their uniformity on the surface of the silica support. The backscattered electron image of the SimSAU2Al13Fe catalyst can be seen in Figures 4.11a and 4.12a for different regions. Bright areas in those two figures are thought to be the metals loaded, i.e., Al and Fe. In addition, elemental mapping of the same catalyst is shown in Figures 4.11b and 4.12b. Regardingly, the other images shown in Figures 4.11 and 4.12 c,d,e, and f are distributions of aluminum, iron, silicon, and oxygen elements in the same catalyst. As can be seen, in both regions, aluminum is uniformly dispersed on the surface (Figures 4.11c and 4.12c). Compared to aluminum, iron seems to be dispersed in region 1 better than in the second region, which suggests non-uniform dispersion of iron loading. However, this difference is not quite large, as Figure 4.10 exhibits.

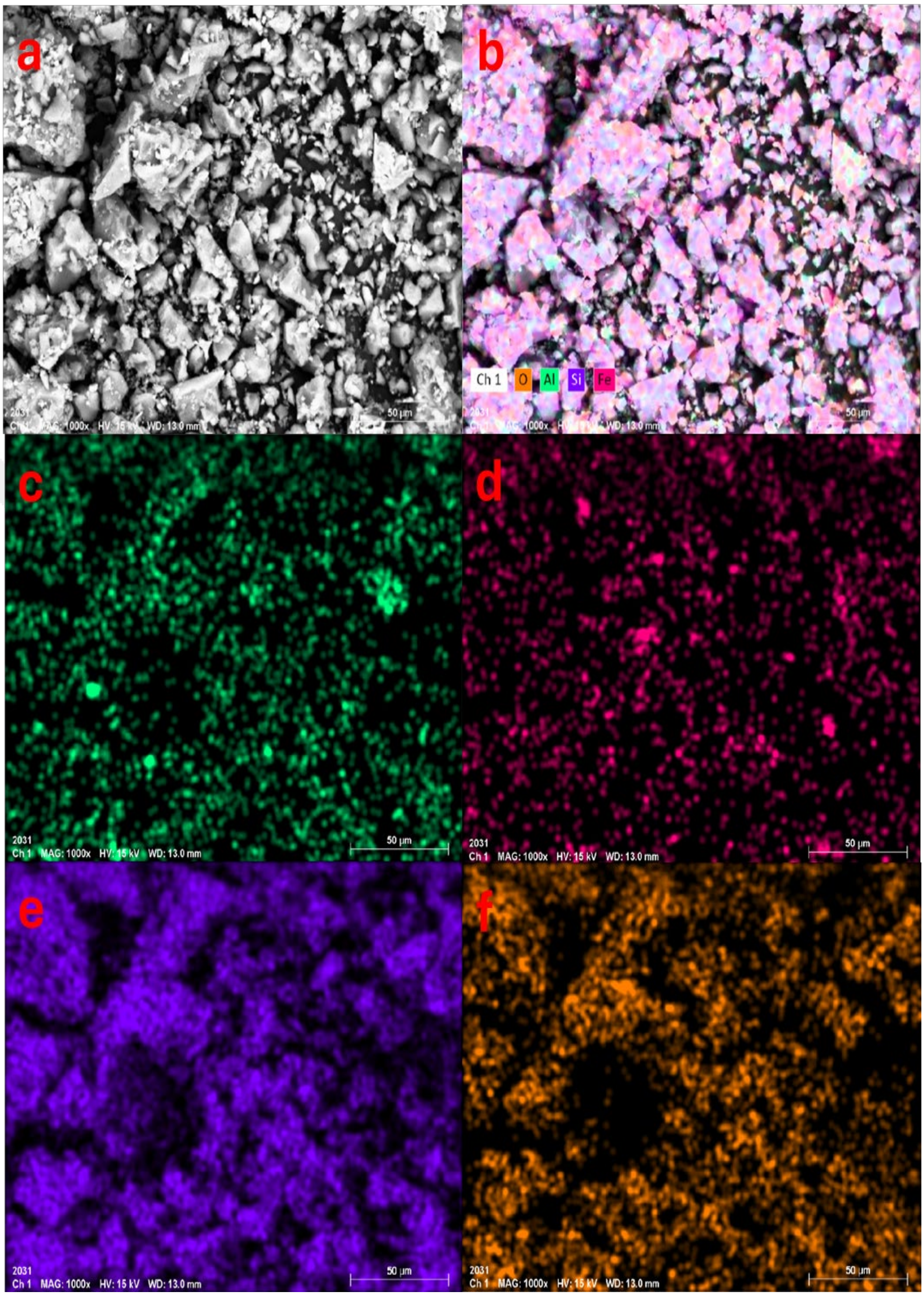

Figure 4.11. (a) Backscattered electron image of SimSAU2Al13Fe, b) the elemental mapping of the SimSAU2Al13Fe catalyst in Region 1, and the distribution of aluminum (c), iron (d), silicon (e), and oxygen (f) elements in the catalyst

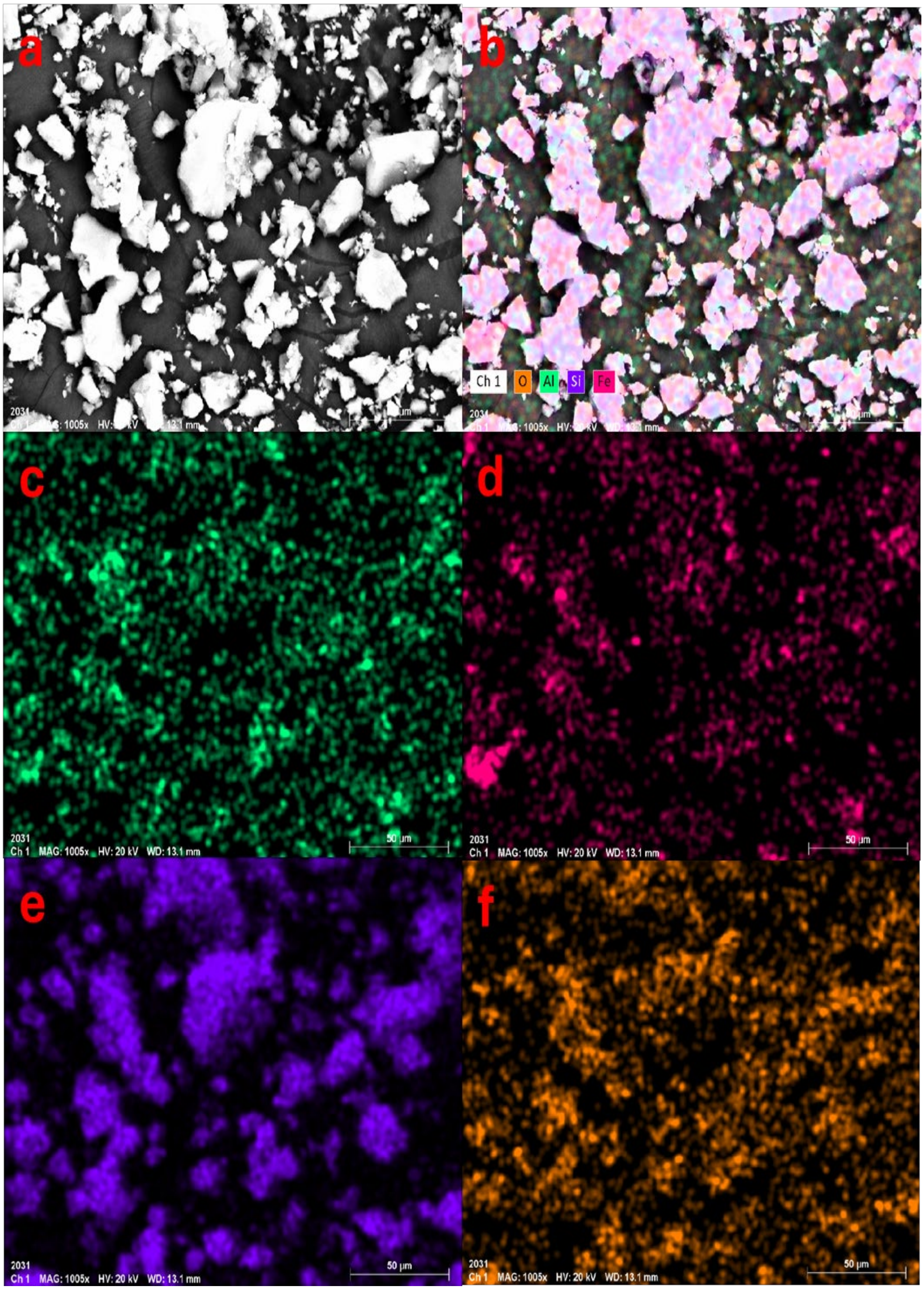

Figure 4.12. (a) Backscattered electron image of SimSAU2Al13Fe, b) the elemental mapping of the SimSAU2Al13Fe catalyst in Region 2, and the distribution of aluminum (c), iron (d), silicon (e), and oxygen (f) elements in the catalyst

Elemental composition regarding the species (Al, Fe, Si, and O_2) available in the SimSAU1Al14Fe catalyst is shown in Figure 4.13 for two different regions in the catalyst. Again, as can be seen in Figure 4.13, whereas there is too small difference for iron content (by 1%), aluminum content is quite similar.

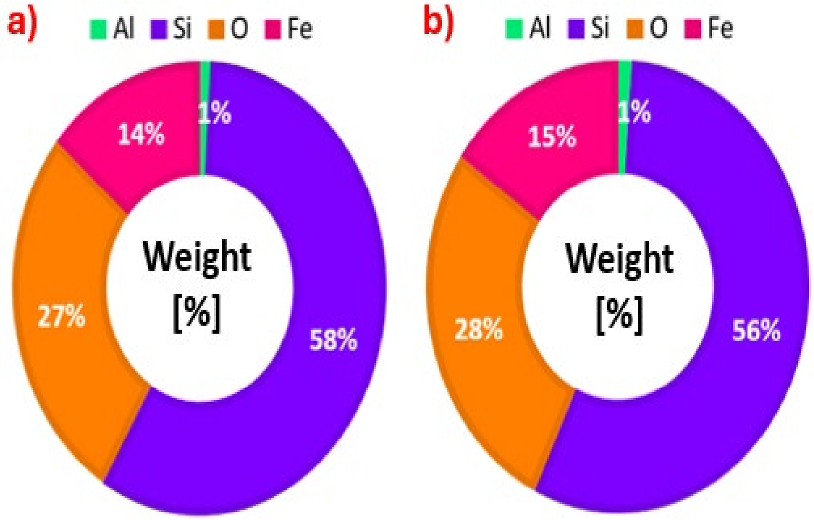

Figure 4.13. Elemental composition of the SimSAU1Al14Fe catalyst from different regions: a) Region 1, and b) Region 2

The backscattered electron image of the SimSAU1Al14Fe catalyst can be seen in Figures 4.14a and 4.15a for different regions. Bright areas in those two figures are thought to be the metals loaded, i.e., Al and Fe. In addition, elemental mapping of the same catalyst is shown in Figures 4.14b and 4.15b. Moreover, the other images shown in Figures 4.14 and 4.15 c,d,e, and f are distributions of aluminum, iron, silicon, and oxygen elements in the same catalyst. As can be seen, in both regions, aluminum is uniformly dispersed on the surface (Figures 4.14c and 4.15c). Compared to aluminum, iron dispersion seems to be less uniform. In addition, in some parts of both regions agglomeration of the Fe metal is observed. Nonuniformity and agglomeration of the Fe metal compared to Al metal could be attributed to the synthesis procedure. Since Fe metal atomic diameter (~ 0.248 nm) is less than Al atomic diameter (~ 0.286 nm), and for all the synthesized catalysts, first, Al is impregnated; it is thought that Al contributes to the blockage of the pores so that Fe metal loading results in less uniform dispersion.

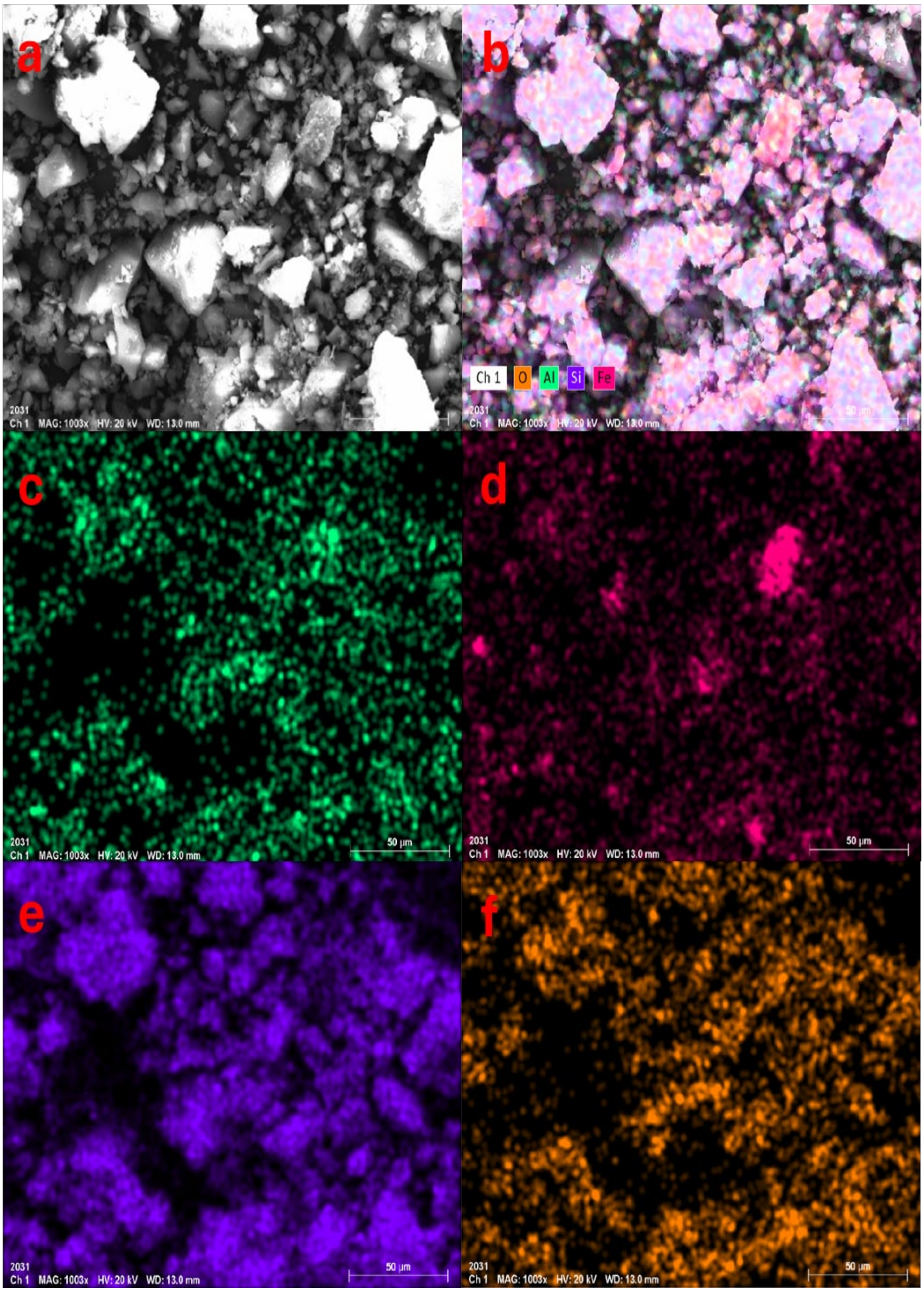

Figure 4.14. (a) Backscattered electron image of SimSAU1Al14Fe, b) the elemental mapping of the SimSAU1Al14Fe catalyst in Region 1, and the distribution of aluminum (c), iron (d), silicon (e), and oxygen (f) elements in the catalyst

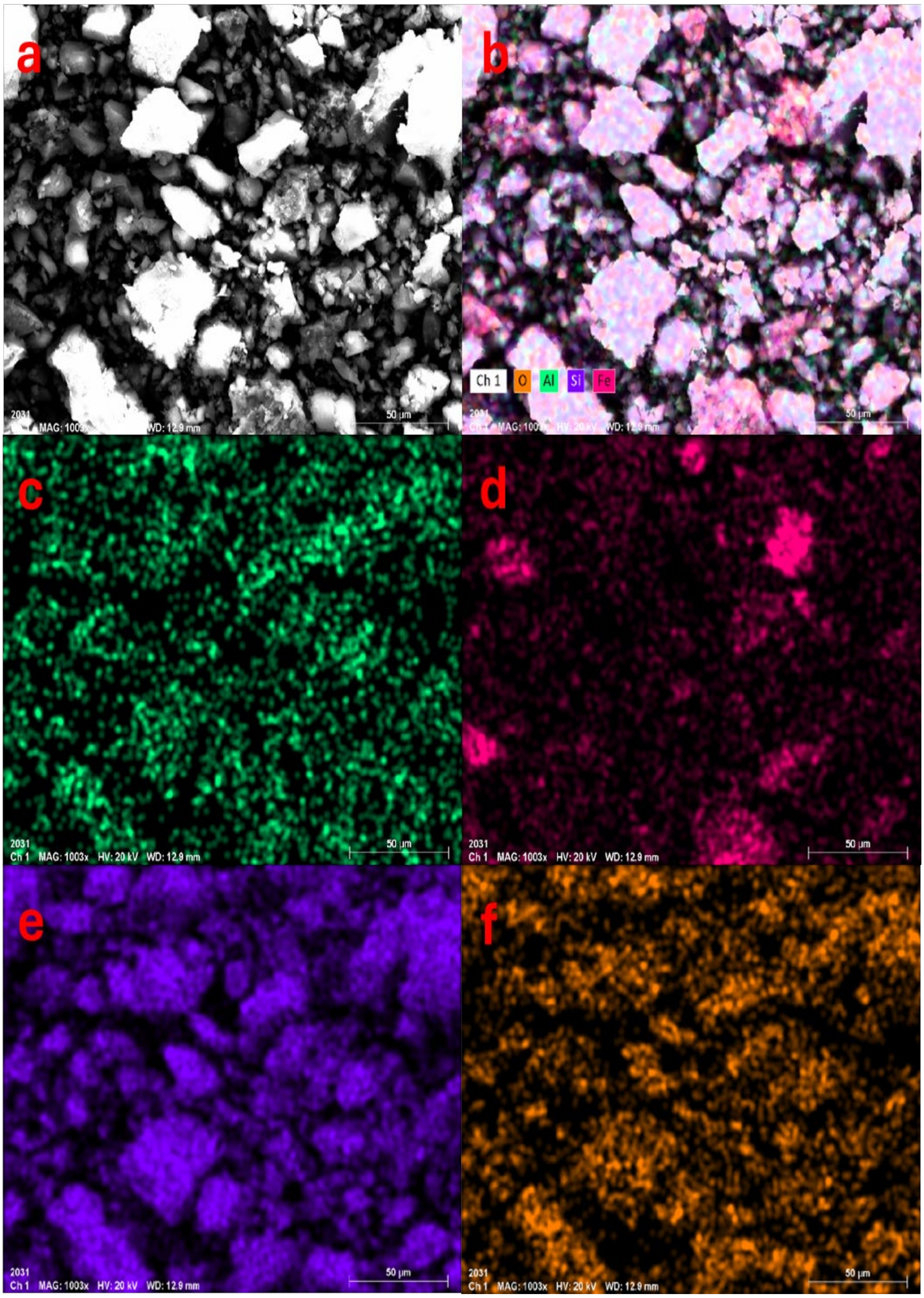

Figure 4.15. (a) Backscattered electron image of SimSAU1Al14Fe, b) the elemental mapping of the SimSAU1Al14Fe catalyst in Region 2, and the distribution of aluminum (c), iron (d), silicon (e), and oxygen (f) elements in the catalyst

Elemental composition regarding the species (Al, Fe, Si, and O_2) available in the SimSAU0.5Al14.5Fe catalyst is shown in Figure 4.16 for two different regions in the catalyst. The iron content of these two regions differs by 3 %, while aluminum content is again quite similar.

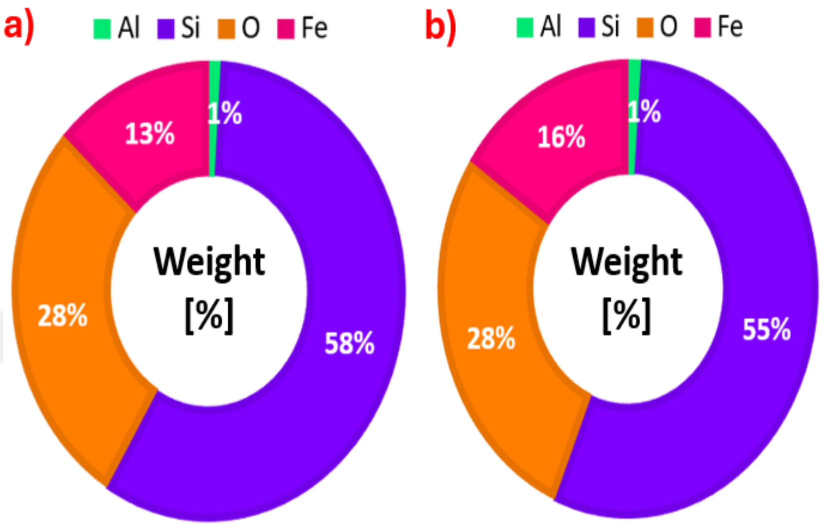

Figure 4.16. Elemental composition of the SimSAU0.5Al14.5Fe catalyst from different regions: a) Region 1, and b) Region 2

Eventually, the backscattered image of the SimSAU0.5Al14.5Fe catalyst can be seen in Figures 4.17a and 4.18a for different regions. Bright areas in those two figures are thought to be the metals loaded, i.e., Al and Fe. In addition, the elemental mapping of the same catalyst is shown in Figures 4.17b and 4.18b. Besides, the other images shown in Figures 4.17 and 4.18 c,d,e, and f are distributions of aluminum, iron, silicon, and oxygen elements in the same catalyst. As can be seen, in both regions, aluminum is uniformly dispersed on the surface (Figures 4.17c and 4.18c). Compared to aluminum, iron dispersion seems to be less uniform, as found before for the SimSAU1Al14Fe catalyst. Thus, in some parts of both regions agglomeration of the Fe metal is observed. Nonuniformity and agglomeration of the Fe metal compared to Al metal could again be attributed to the synthesis procedure. Since Fe metal atomic diameter (~ 0.248 nm) is less than Al atomic diameter (~ 0.286 nm), and for all the synthesized catalysts first Al is impregnated, it is considered that Al contributes to the blockage of the pores so that Fe metal loading results in less uniform dispersion.

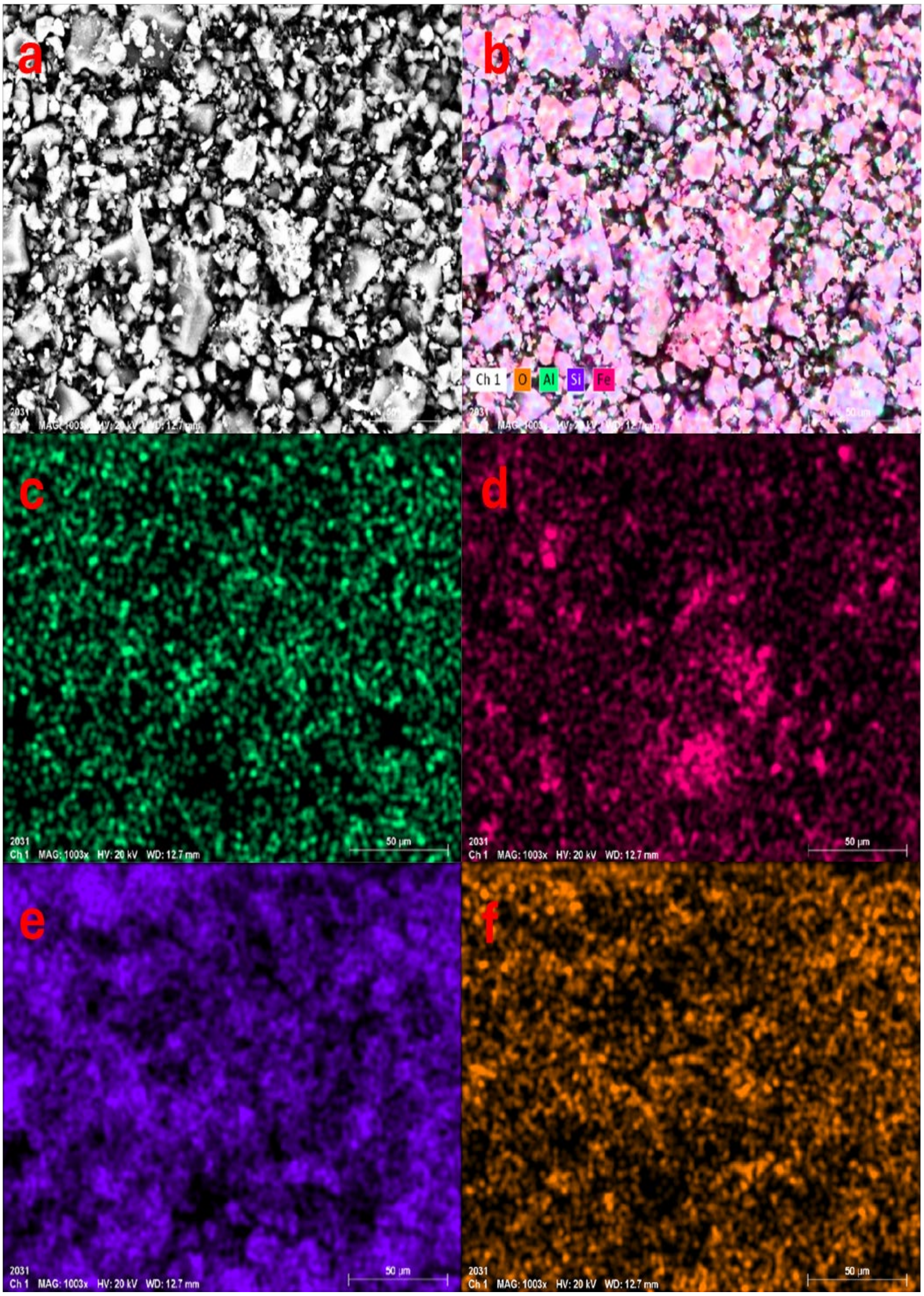

Figure 4.17. (a) Backscattered electron image of SimSAU0.5Al14.5Fe, b) the elemental mapping of the SimSAU0.5Al14.5Fe catalyst in Region 1, and the distribution of aluminum (c), iron (d), silicon (e), and oxygen (f) elements in the catalyst

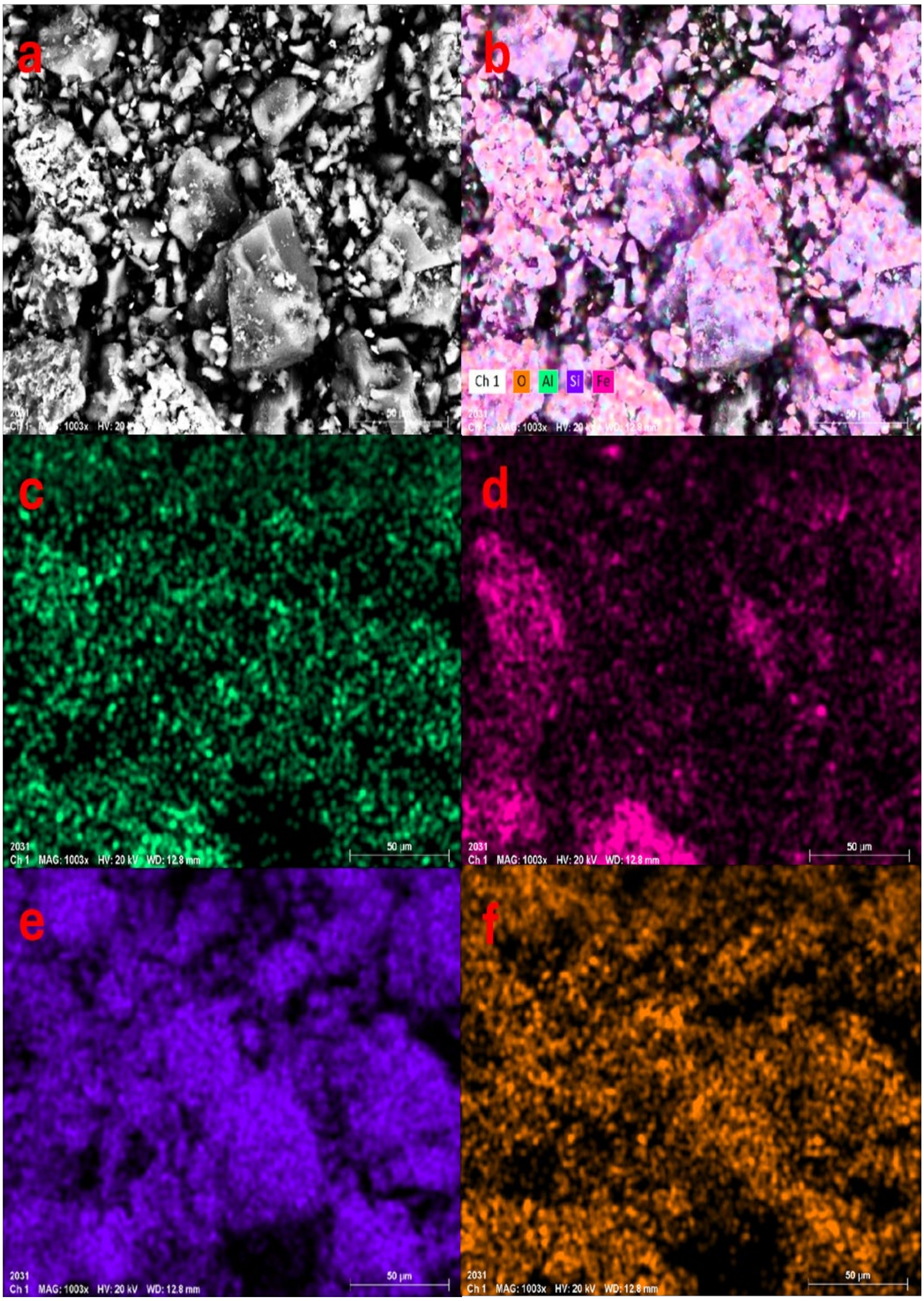

Figure 4.18. (a) Backscattered electron image of SimSAU0.5Al14.5Fe, b) the elemental mapping of the SimSAU0.5Al14.5Fe catalyst in Region 2, and the distribution of aluminum (c), iron (d), silicon (e), and oxygen (f) elements in the catalyst

4.1.2.4 Thermogravimetric Analysis Results

Activation energies of PLA degradation reactions for synthesized bimetallic catalysts were found using a thermogravimetric analyzer. Those analyses were performed on pure PLA and PLA samples with the synthesized catalysts, as shown in Figure 4.19. Then, the activation energy of the PLA degradation reaction was calculated by applying the procedure given in Appendix C. The blue line in Figure 4.19 shows the change in weight loss of PLA with an increase in temperature. Pure PLA decomposition starts around 310 ℃ and finishes around 360 ℃. A sharp decrease between those temperatures in Figure 4.19 demonstrates the PLA chain degradation.

Regarding the procedure in Appendix C, Figure C.1 was obtained for non-catalytic PLA degradation reaction for different reaction orders, namely n=1 and n=2. Better fitting was obtained for the first-order degradation reaction. This result agrees with the PLA degradation reactions performed in the literature (Sivri et al., 2019). The activation energy of the PLA degradation reaction was found to be 262 kJ/mol.

Utilization of catalysts shifted the TGA curve to the left in all cases, meaning that the degradation temperature of the PLA decomposition reaction decreased with the use of a catalyst. In Figure 4.19, red, purple, and green lines display TGA curves regarding the use of SimSAU0.5Al14.5Fe, SimSAU1Al14Fe, SimSAU2Al13Fe catalysts with PLA samples. Almost the same behavior for all the catalysts was observed, which could be attributed to very small differences in Al/Fe ratio.

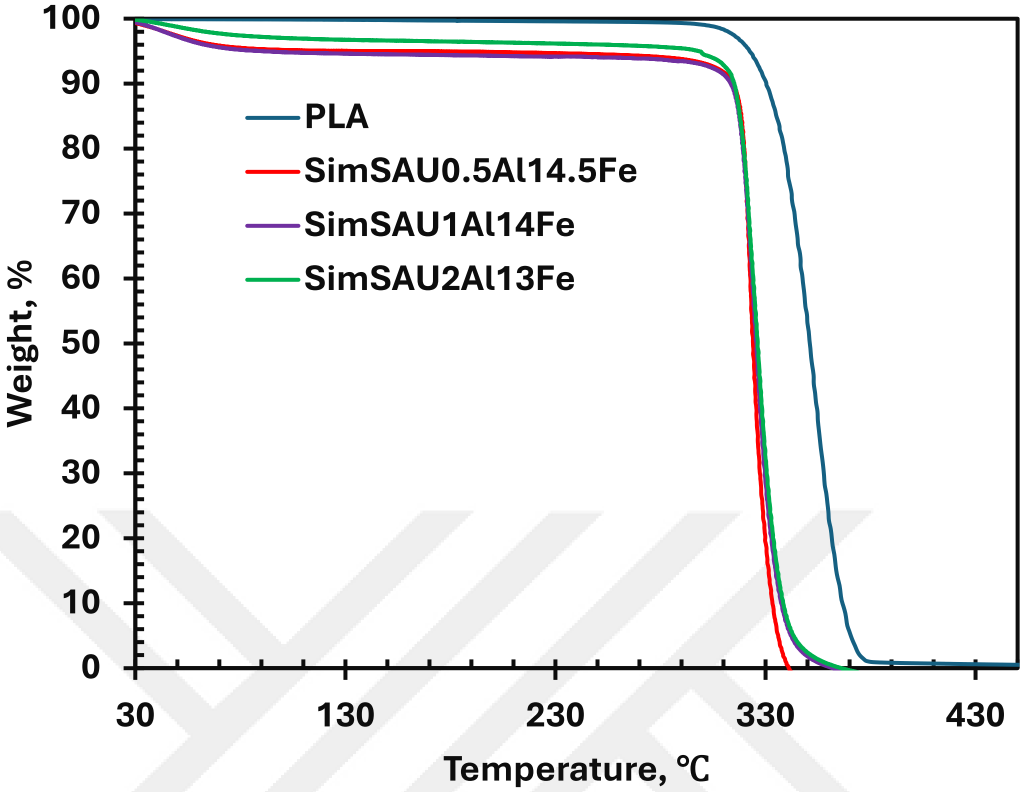

Figure 4.19. TGA results of PLA degradation reaction with, and without catalysts (SimSAU0.5Al14.5Fe, SimSAU1Al14Fe, SimSAU2Al13Fe) under N_2 medium

Table 4.3 shows degradation temperatures regarding distinct % of weight losses regarding the degradation of PLA, and PLA with the synthesized catalysts. As seen in Table 4.3, the use of a catalyst decreased the degradation temperature from 336 ℃ to around 321 ℃ for 30 % weight loss. In addition, this behavior was also observed for 60 % weight loss a decrease from 348 ℃ to around 327 ℃. Thus, all the synthesized catalysts are active for the PLA degradation reaction, as already inferred from Figure 4.19.

Table 4.3 Degration temperatures of 30 wt.%, and 60 wt.% of pure PLA and PLA with synthesized catalysts (Cat1: SimSAU0.5Al14.5Fe, Cat2: SimSAU1Al14Fe, and Cat3: SimSAU2Al13Fe)

	Weight Loss, %							
	PLA		**PLA+Cat1**		**PLA+Cat2**		**PLA+Cat3**	
	30	**60**	**30**	**60**	**30**	**60**	**30**	**60**
Temperature (°C)	336	348	321	326	321	327	322	328

4.2 PLA Depolymerization Reaction Results

The effects of the Al/Fe weight ratio, reaction temperature, and reaction time on the product yield and product distribution were studied for the PLA degradation reaction. The residual that remained in the reactor, the non-volatile products, and volatile products were named as solid, condensable products, and non-condensable products, respectively. The weights of solid and condensable products were measured at the end of the degradation reaction so as to find non-condensable products by subtracting the weights of the solid and condensable products from the PLA amount that was used in the degradation reactions. Calculations regarding product yields are given in Appendix D. The composition of the condensable products was determined by GC. The relative response factor (RRF) technique was utilized to determine the number of moles of the condensable products. RRF values are given in Appendix Table E.1. Moreover, the number of moles and weight fraction calculations are given in Appendix E. In addition, beta factors were utilized in order to calculate the number of moles of the non-condensable products. Beta factors are given in Appendix Table

F.1. The number of moles and composition calculations regarding non-condensable products are given in Appendix F. Lastly, repeated experiments of PLA degradation in the pyrolysis system were conducted twice under the following conditions: 250℃ reaction temperature, 70rpm mixing rate, 60 minutes reaction time, ϑ_{Ar} = 50 ml/min, and without a catalyst.

Figure 4.20 displays the product yields regarding the repeatability experiments conducted as in conditions mentioned above. Solid yield for first run was 13.33 %, whreas it is 13.78 % for the second run. Condensable yield for first run was 32 % when it is 33 % for the second run. Lastly, non-condensable yield changed from 54.67 % to 53.22 % for the second run compared to first run. Those results show that the experiments are repeatable.

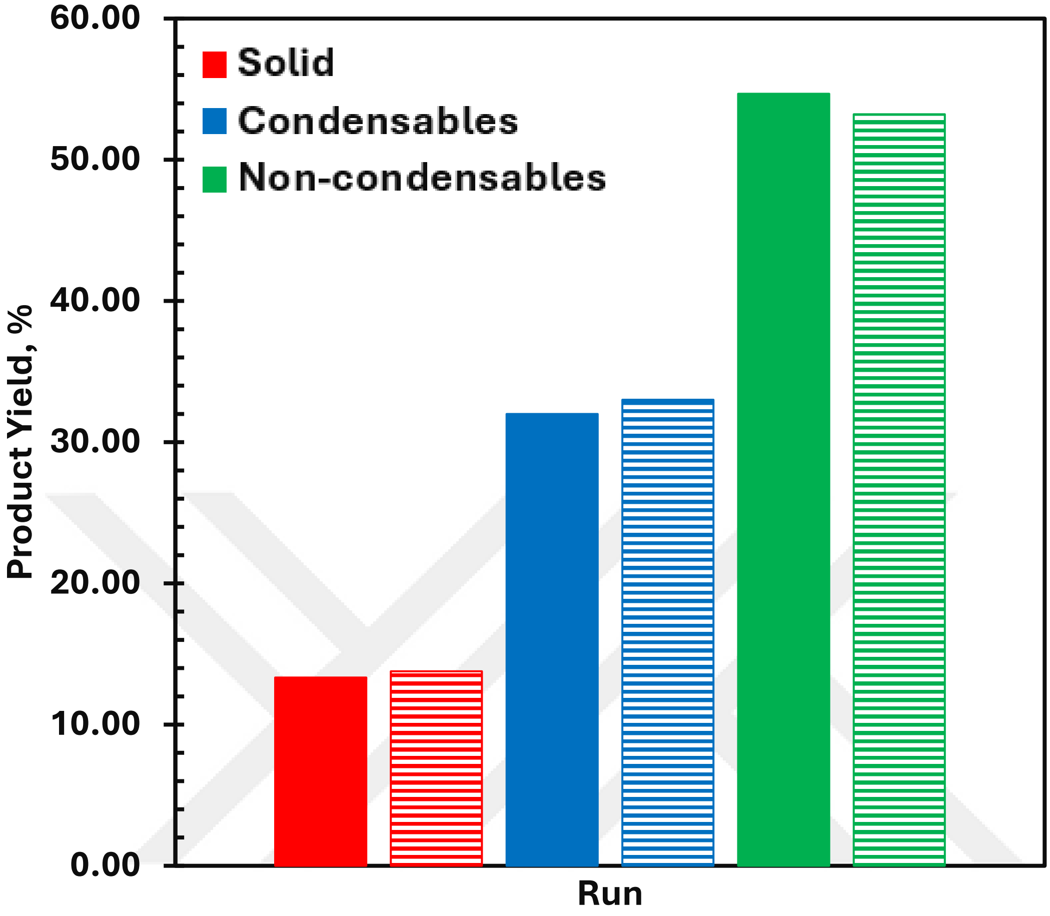

Figure 4.20. Product yields of repeatability experiments: Filled box: first run, and lined box: second run (Non-catalytic, T=250 ℃, 70 rpm, 60 min, and ϑ_{Ar} = 50 ml/min)

Figure 4.21 exhibits the condensable product distributions of the repeatability experiments. As can be seen, almost all the products were achieved at the same concentration, only DL, L decreasing from 53.12 wt.% to 52.38 wt.%, which was almost compensated by the increase in Messo L concentration from 33.40 wt.% to 34.46 wt.%. LA concentration is 3.39 wt.% for both runs, whereas PA concentration changed from 1.45 wt.% to 1.28 wt.%. Lastly, UI product concentration decreased from 8.62 wt.% to 8.48 wt.%. Following that, the same conclusion, which is repeatability, could be inferred from these results.

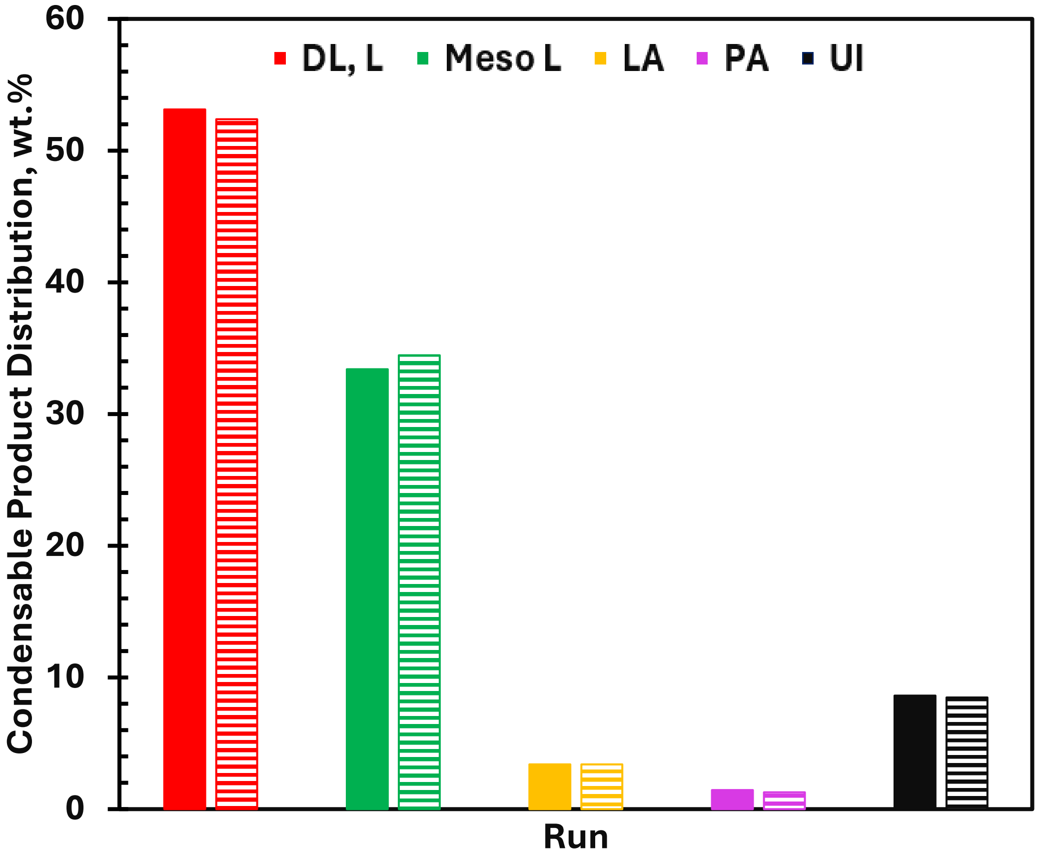

Figure 4.21. Condensable product distributions of repeatability experiments: Filled box: first run, and lined box: second run (Non-catalytic, T=250 °C, 70 rpm, 60 min, and ϑ_{Ar} = 50 ml/min)

Investigating the non-condensable product distributions of the repeatability experiments (Figure 4.22), it was observed that acetaldehyde concentration slightly decreased from around 78.9 mol % to 78.5 mol % from the first run to the second run. On the other hand, carbon monoxide concentration increased moderately from 20.23 mol % to 20.69 mol % between the two runs. Carbon dioxide concentration changed a bit from 0.77 mol % to 0.86 mol %. Lastly, for the two runs, trace amounts of ethylene and hydrogen were observed. As a result, considering product yields and distributions, approximately the same results were obtained, which is an indication of repeatability.

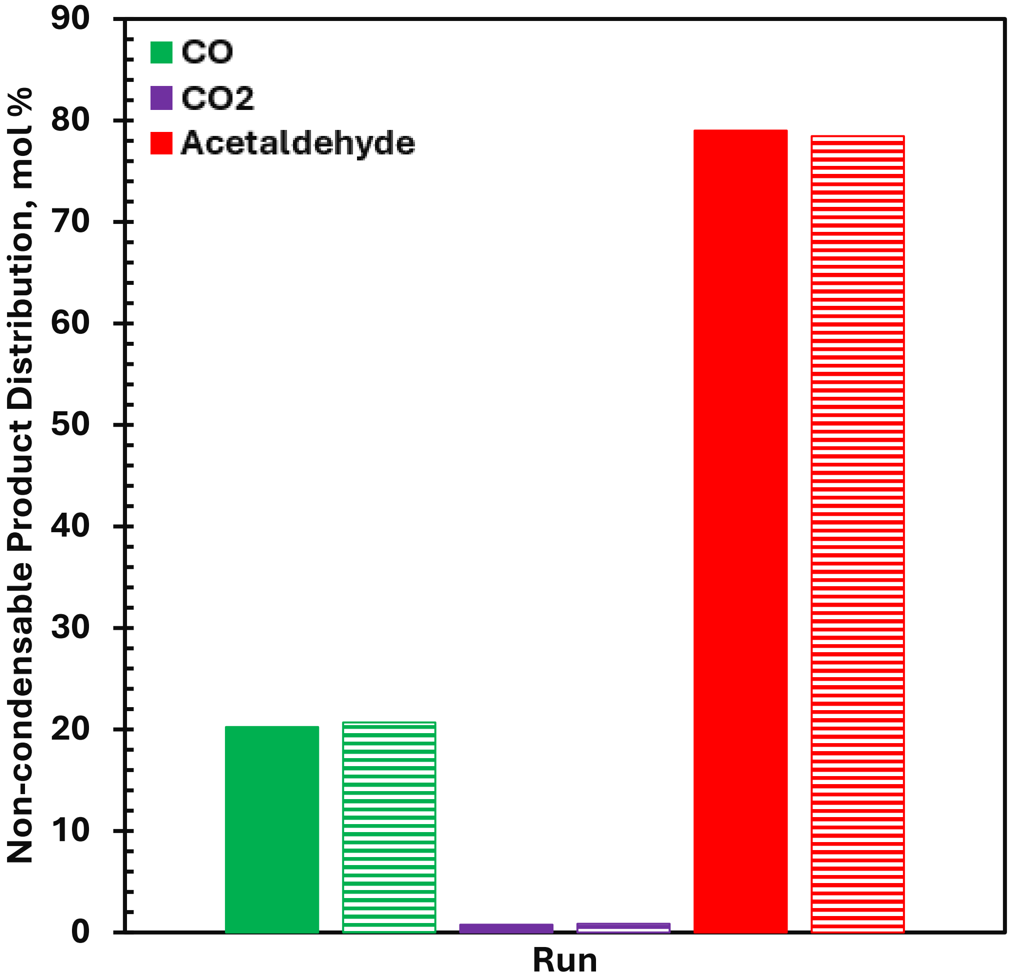

Figure 4.22. Non-condensable product distributions of repeatability experiments: Filled box: first run, and lined box: second run (Non-catalytic, T=250 °C, 70 rpm, 50 min, and ϑ_{Ar} = 50 ml/min)

4.2.1 The Effect of Al/Fe Weight Ratio on the Product Yield and Product Distribution

First of all, how different loadings of Al and Fe into silica aerogel support impact the product yield of solid, condensable, and non-condensable was tested. In all cases, total metal loading was kept to be 15 wt.%. Beginning with 2 wt.% Al, and 13 wt.% Fe loaded silica aerogel, pyrolysis experiments were conducted with the following conditions: 50 ml/min argon gas flow rate, 5°C/min heating rate, 225 °C the reaction temperature, and 70 rpm mixing rate. The following crucial results were obtained by keeping reaction conditions the same in all cases and by only changing the Al and Fe wt.% within 15 wt.% of metal loading into silica aerogels. Increasing the Fe content from 13wt.% to 14.5 wt.% of the catalyst resulted in less solid residual (Figure 4.23); in other words, solid yield decreased from around 19.45 % to 11.5 %. Increasing the Fe content of the catalyst led to more decomposition of PLA and less solid was observed at the end of the reaction. Besides, 14 wt.% Fe loaded catalyst showed so close solid yield to 14.5 wt.% Fe loaded catalyst (13 %). This could be attributed to the difficulty of loading 0.5 wt.% Al, which might be so close to 1 wt.% Al loading, which can be inferred from EDX results shown earlier.

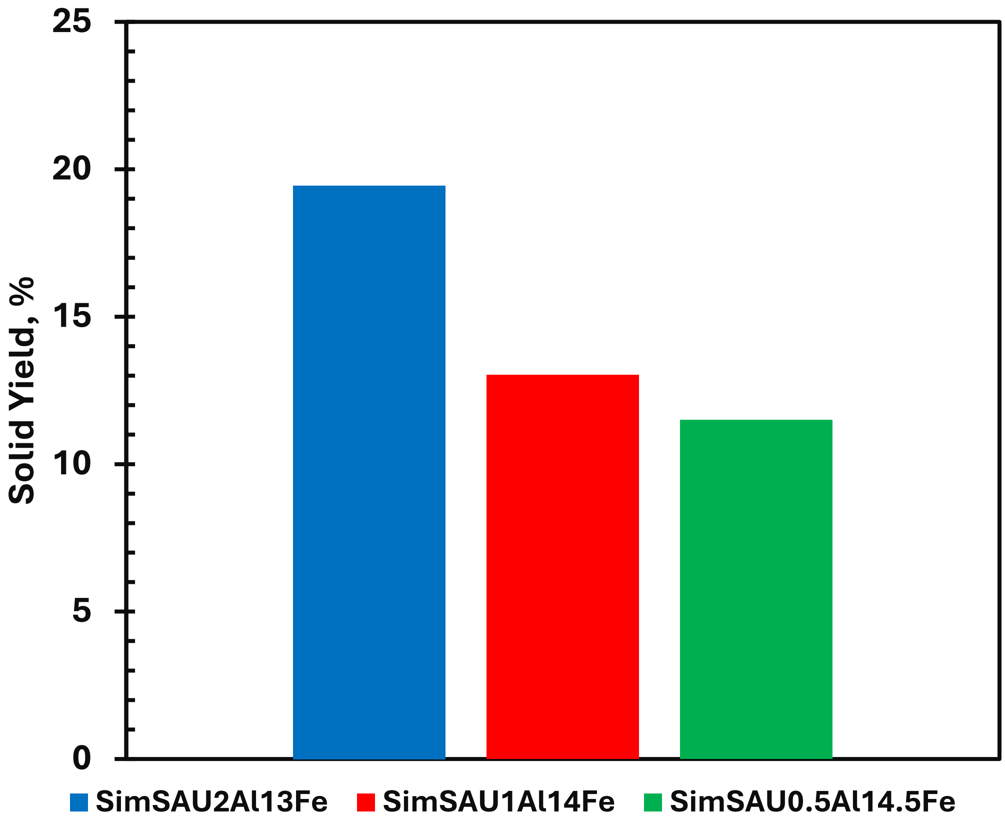

Figure 4.23. The effect of the Al/Fe weight ratio on the solid yield (T=225 °C, 70 rpm, 60 min, and ϑ_{Ar} = 50 ml/min)

Considering the condensable product yield, increasing the Fe content of the catalyst led to more condensable product yield. This increase was from 40 % (for SimSAU2Al13Fe) to 51 % (for SimSAU0.5Al14.5Fe) by a total 27.5 % increase (Figure 4.24). Again, comparing the SimSAU1Al14Fe and SimSAU0.5Al14.5Fe catalysts, only a 2 % increase was observed by increasing wt.% of Fe from 14 wt.% to 14.5 wt.%.

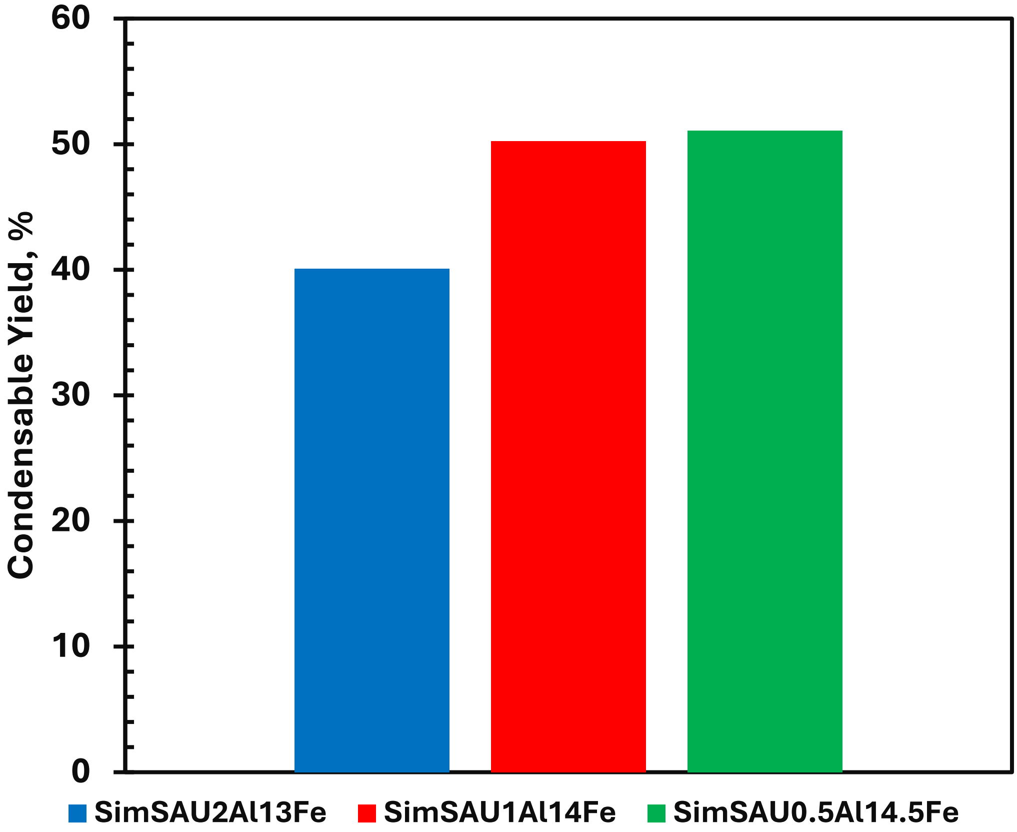

Figure 4.24. The effect of the Al/Fe weight ratio on the condensable yield (T=225 °C, 70 rpm, 60 min, and ϑ_{Ar} = 50 ml/min)

Eventually, comparing non-condensable product yield, the highest non-condensable yield was achieved for the least amount of Fe content, being around 40 %. These results showed that an increase in Al content favored the decomposition reaction to non-condensable, whereas the increase in Fe content favored the decomposition reaction to condensable products. The study conducted by Sivri (Sivri, 2023), showed the same trend when 15 wt.% Al and 15wt.% Fe loaded silica aerogels are compared. In the study mentioned, catalysts are not bimetallic so a synergetic impact is attempted to be achieved in this study for Al, and Fe loaded bimetallic catalysts. The results regarding non-condensable product yield can be seen in Figure 4.25.

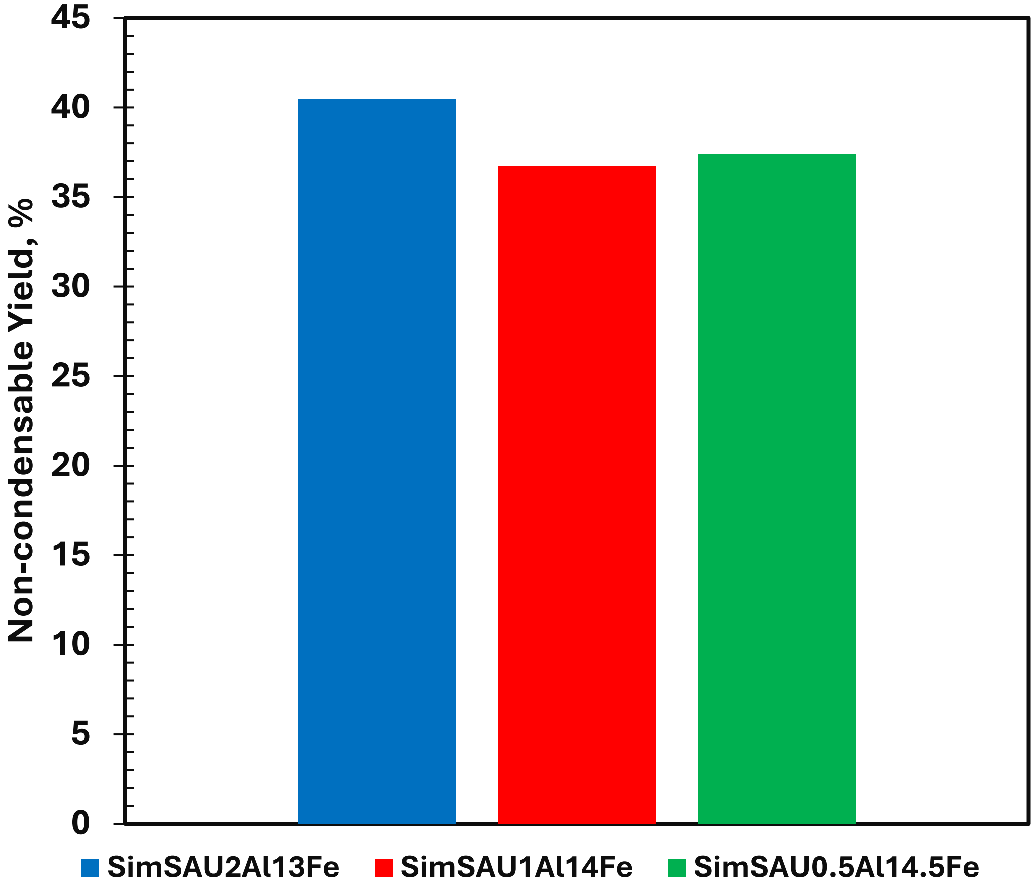

Figure 4.25. The effect of the Al/Fe weight ratio on the non-condensable yield (T=225 ℃, 70 rpm, 60 min, and ϑ_{Ar} = 50 ml/min)

The effect of the Al/Fe weight ratio on product distributions was also analyzed. Figure 4.26 displays the condensable product distribution regarding the three different Al/Fe ratios. As can be seen, DL, L concentration decreased slightly from 62 wt.% to 58.5 wt.% with the increase in Fe content, whereas Meso L concentration increased from 32.9 wt.% to 35.4 wt.% highest for SimSAU1Al14Fe catalyst, and second highest for SimSAU0.5Al14.5Fe catalyst as 34.6 wt.%. On the other hand, LA concentration seems to be almost the same for the SimSAU2Al13Fe, and SimSAU1Al14Fe catalysts, whereas it increased to 4.2 wt.% from 3.6 wt.% for SimSAU0.5Al14.5Fe catalyst. Eventually, considering PA concentrations, it was observed that almost the same concentration, which is around 1.5 wt.%, was achieved for all Al/Fe ratios inspected.

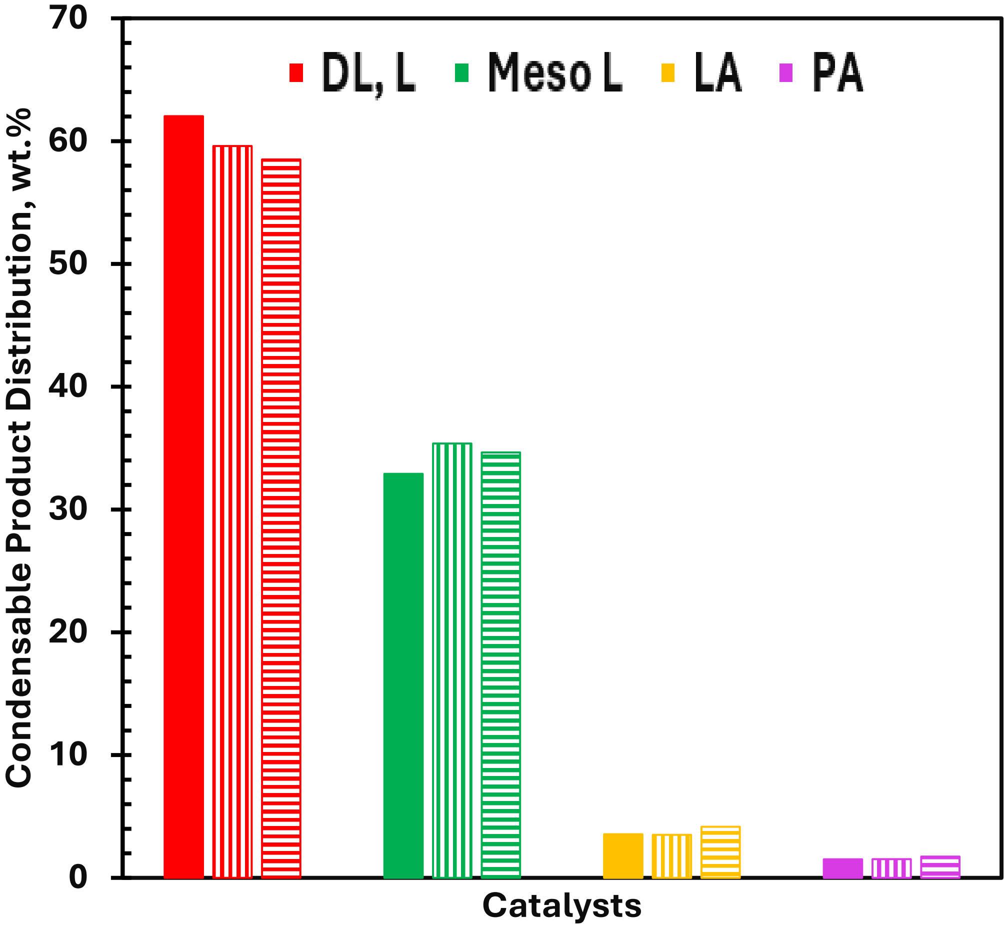

Figure 4.26. The effect of Al/Fe weight ratio on the condensable product distributions: Filled box: SimSAU2Al13Fe, vertical lined box: SimSAU1Al14Fe, and horizontal lined box: SimSAU0.5Al14.5Fe (T=225 °C, 70 rpm, 60 min, and ϑ_{Ar} = 50 ml/min)

When non-condensable product distribution was considered for 15th minutes of the reaction time for different Al/Fe weight ratios (Figure 4.27), carbon monoxide concentration increased from 19.5 mol % to 23.5 mol % with a decrease in Al/Fe weight ratio. While carbon monoxide concentration seems to have a trend, acetaldehyde, and carbon dioxide concentrations showed fluctuation between 56.1 mol % and 60.9 mol % for acetaldehyde and between 15.5 mol % and 20.7 mol % for carbon dioxide.

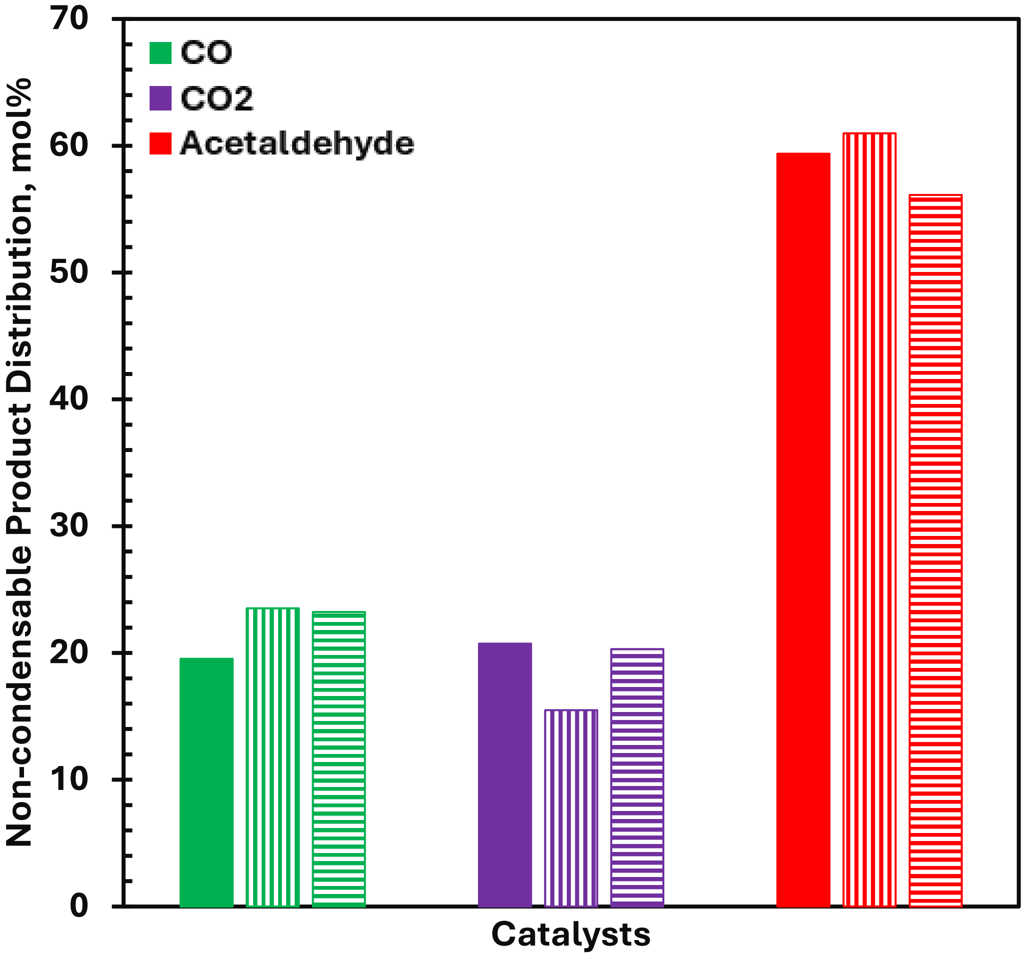

Figure 4.27. The effect of Al/Fe weight ratio on the non-condensable product distributions for t=15 min: Filled box: SimSAU2Al13Fe, vertical lined box: SimSAU1Al14Fe, and horizontal lined box: SimSAU0.5Al14.5Fe (T=225 °C, 70 rpm, 60 min, and ϑ_{Ar} = 50 ml/min)

On the other hand, non-condensable product distribution was considered for the 50th minute of the reaction time for different Al/Fe weight ratios (Figure 4.28), as well. Clearer trends for all the species were observed. Carbon monoxide concentration seems to decrease from 31.3 mol % to 22.7 mol % for a decrease from 2 wt.% to 0.5 wt.% Al content. Moreover, carbon dioxide concentration followed the same trend with a decrease from 6.7 mol % to 3.9 mol % with the increase in Al content. Eventually, acetaldehyde concentration increased from 62.1 mol % to 73.4 mol % with the decrease in Al content.

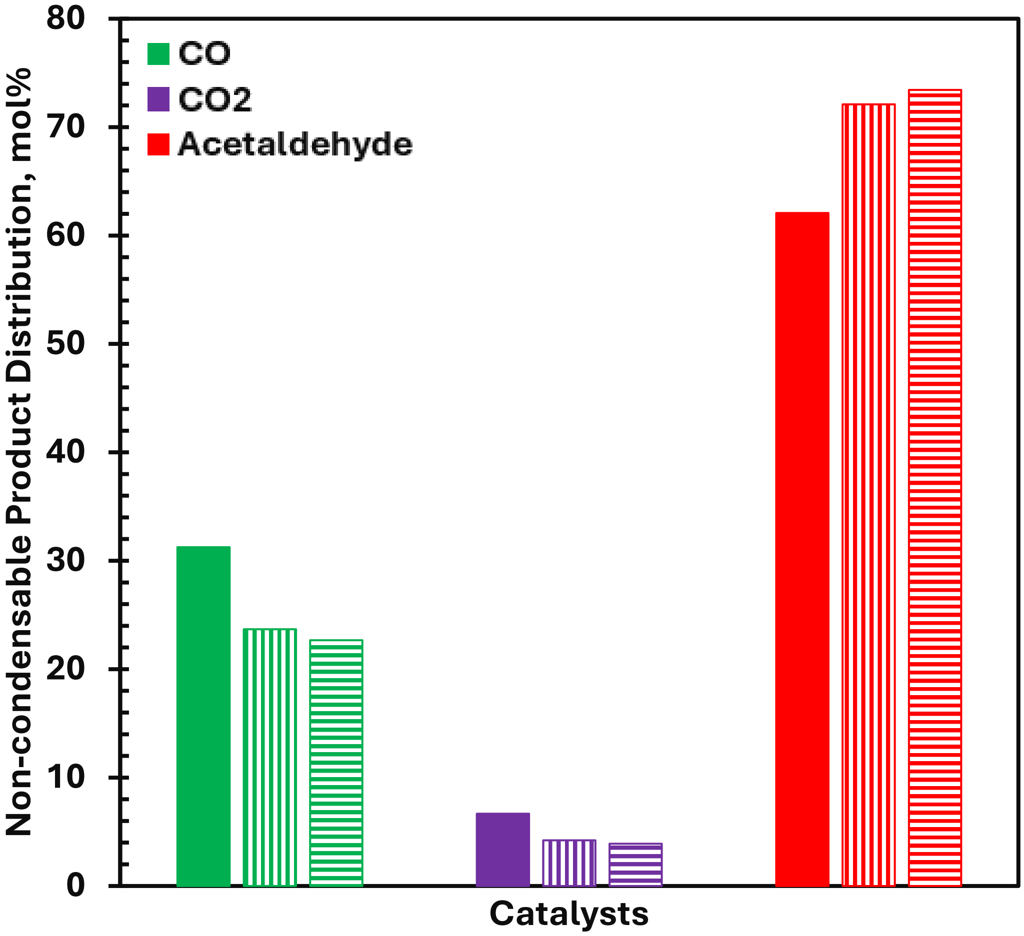

Figure 4.28. The effect of Al/Fe weight ratio on the non-condensable product distributions for t=50 min: Filled box: SimSAU2Al13Fe, vertical lined box: SimSAU1Al14Fe, and horizontal lined box: SimSAU0.5Al14.5Fe (T=225 ℃, 70 rpm, 60 min, and ϑ_{Ar} = 50 ml/min)

These product distribution results showed that change in the Al/Fe weight ratio did not only have impact on the product yields bu it had also impact on the condensable, and non-condensable product distributions.

Following obtaining these results, with the aim of the highest amount of condensable and the least solid product yield SimSAU0.5Al14.5Fe catalyst was chosen for analyzing the temperature, and time impact on the decomposition reaction.

4.2.2 Effect of the Reaction Temperature on the Product Yield, and Product Distribution

Figure 4.29 shows the results regarding solid yield for the decomposition reaction at different temperatures (from 225 ℃ to 350 ℃) for both non-catalytic and catalytic experiments conducted. Reaction conditions are as follows: 50 ml/min argon flow rate, 70 rpm mixing rate, catalyst: SimSAU0.5Al14.5Fe, and 5 ℃/min heating rate. As can be seen in Figure 4.29, at 225 ℃, the solid yield for the non-catalytic decomposition reaction was around 66.5 %, whereas it was 11.5 % for the catalytic decomposition reaction. Besides, at 250 ℃, the solid yield for the non-catalytic decomposition reaction was around 13.8 %, whereas no solid was observed at that temperature for the catalytic decomposition reaction. In other words, it can be inferred catalyst is active for that reaction so that less solid remains compared to the non-catalytic decomposition reaction case. This activity could better be seen for 225 ℃, and 250 ℃ since for the other temperatures till 350 ℃ no solid was observed in either case.

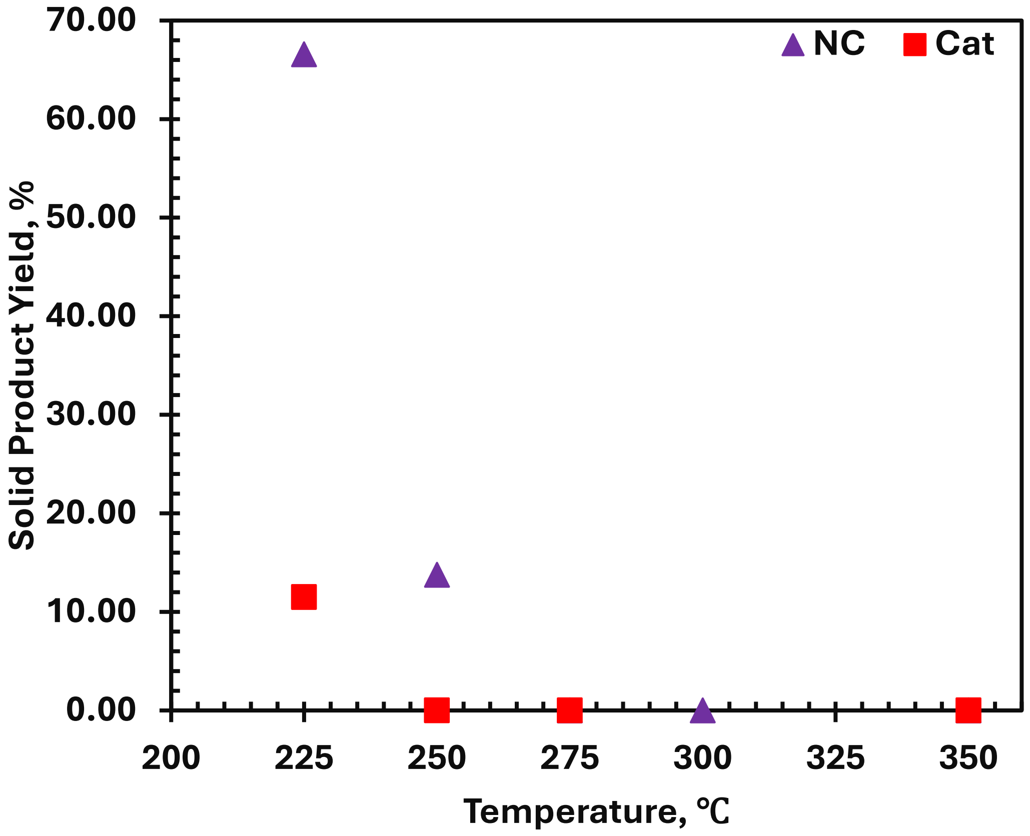

Figure 4.29. The effect of reaction temperature on the solid yield: Purple: Non-catalytic, and Red: Catalytic (SimSAU0.5Al14.5Fe, 70 rpm, 60 min, and ϑ_{Ar} = 50 ml/min)

Figure 4.30 displays the condensable product yield regarding the same conditions mentioned in the solid yield comparison. For non-catalytic decomposition reactions, it was observed that condensable product is the least at 225 °C by being around 7 wt.%, and it peaked at 250 °C to 275 °C by being around 33 wt.%. The trend for the condensable product yield was observed slightly to decline after 275 °C. However, for catalytic decomposition reaction higher amount of condensable product was observed in all temperatures. This difference, especially, is crystal clear at 225 °C. Compared to 7 wt.% of non-catalytic results, around 51 wt.% condensable product was achieved at that temperature. The same trend of decline was also observed for catalytic decomposition reactions at higher temperatures.

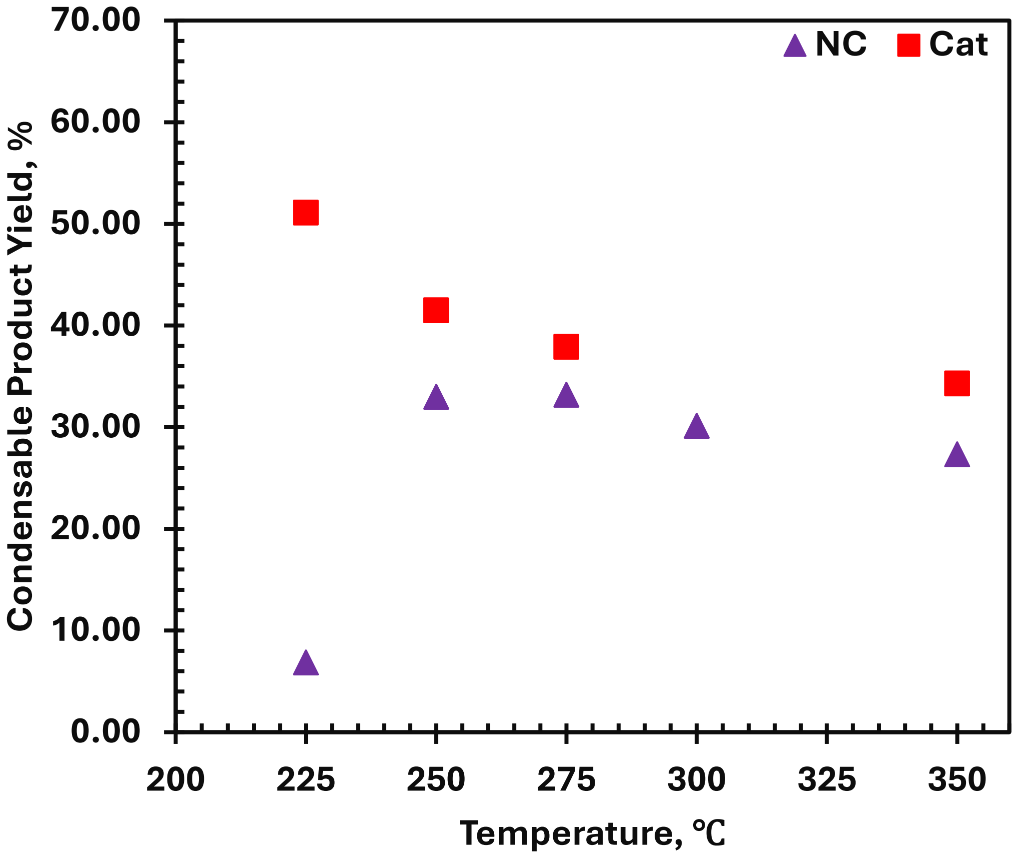

Figure 4.30. The effect of reaction temperature on the condensable product yield: Purple: Non-catalytic, and Red: Catalytic (SimSAU0.5Al14.5Fe, 70rpm, 60 min, and ϑ_{Ar} = 50 ml/min)

Finally, the non-condensable product yield can be seen in Figure 4.31. According to the figure, non-condensable product yield for the catalytic decomposition reaction is higher than the non-catalytic decomposition reaction till 275 °C, after which more amount of non-condensable product achievement for non-catalytic decomposition reaction was observed.

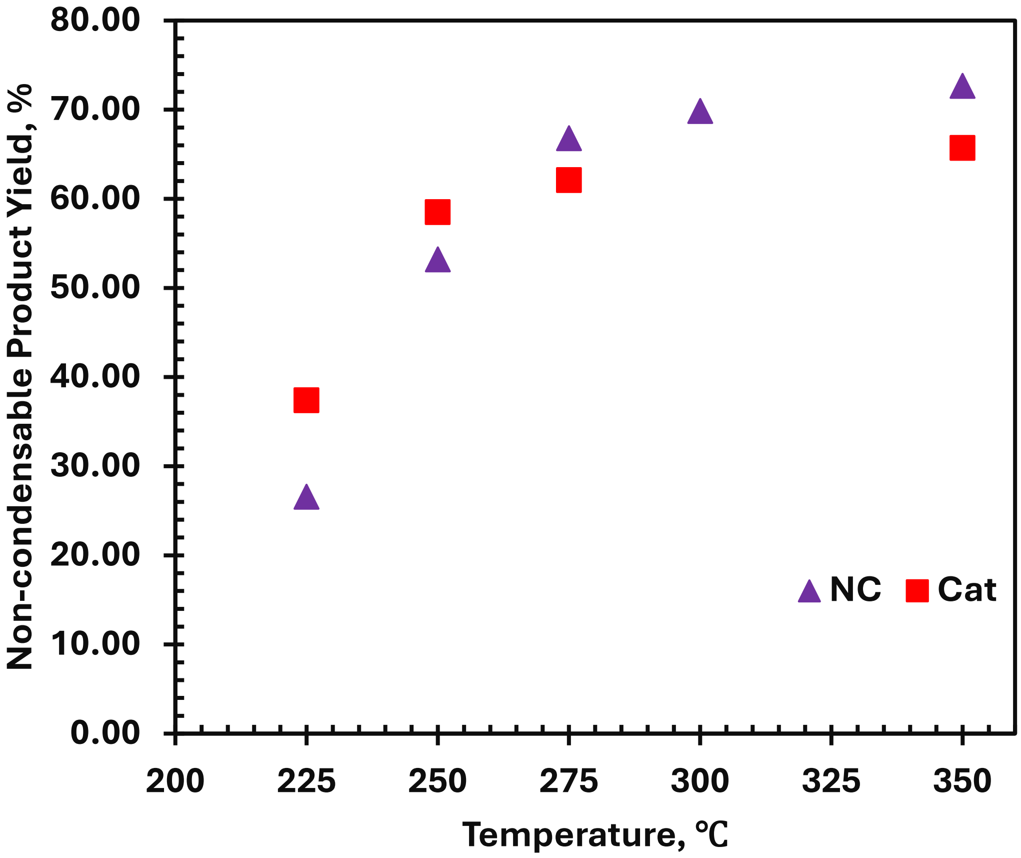

Figure 4.31. The effect of reaction temperature on the non-condensable product yield: Purple: non-catalytic, and Red: Catalytic (SimSAU0.5Al14.5Fe, 70rpm, 60 min, and ϑ_{Ar} = 50 ml/min)

Both condensable and non-condensable products were further analyzed by using GC equipment. Using a GC flame ionization detector (FID), condensable product distribution for non-catalytic and catalytic decomposition reactions was acquired (Figures 4.32 and 4.33). The condensable products observed are propionic acid (PA), lactic acid (LA), meso-lactide (Meso L), D and L lactide (DL, L), and unidentified products (UI). The retention times of the products, except UI products, are given in Appendix E. The following unidentified products at the following retention times (min) were observed: U1: 9.3, U2: 10.3, U3:12.1, U4: 13.4, U5: 17.4, and U6: 22.9. Whereas U3, U5, and U6 were only observed for non-catalytic decomposition reactions U4 was observed for both non-catalytic and catalytic decomposition reactions. The remaining UI products, U1 and U2, were only observed for catalytic decomposition reactions. For non-catalytic decomposition reactions, U3 was first observed at 250 ℃, and its concentration slightly increased with the increase in temperature. On the other hand, a trace amount of U5 was first observed at 275 ℃ and remained in trace amounts with the increase in temperature. U4 was also observed at trace amounts and remained at trace amounts with the increase in temperature. Its first observation was at 300 ℃. Lastly, U6 was only observed at 275 ℃ with a trace amount, as well.

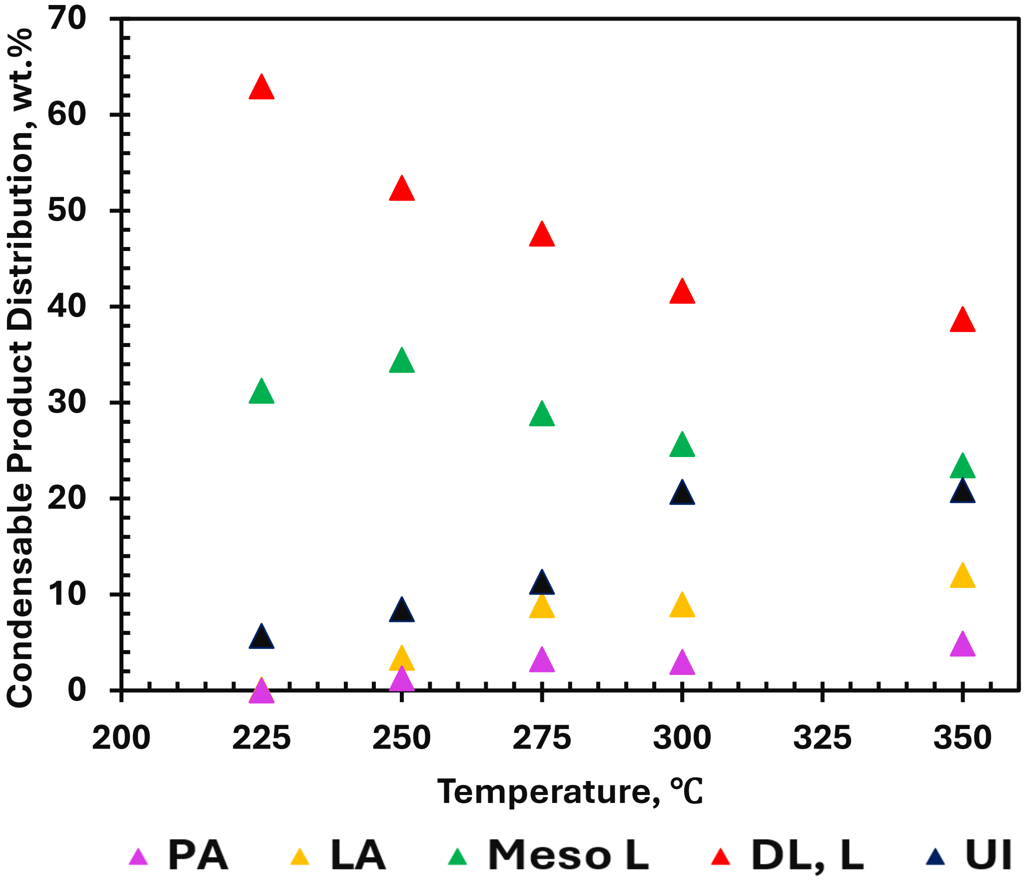

Figure 4.32. The effect of reaction temperature on the condensable product distributions in the absence of catalysts. (70rpm, 60 min, and ϑ_{Ar} = 50 ml/min)

As can be seen in both figures (Figures 4.32-4.33) DL, L, and Meso L decline was observed with the increase in temperature. For non-catalytic decomposition reactions, this decline was from 63 wt.% to 42 wt.% for DL, L and 31 wt.% to 26 wt.% for Meso L whereas the decline for catalytic decomposition reactions was from 59 wt.% to 52 wt.% for DL, L, and 35 wt.% to 15 wt.% for Meso L. The remaining products increased in amount with the increase in temperature. This was also observed by looking at the color of the acetone solution in which condensable products were dissolved. This change was from white to yellow. The difference between the non-catalytic and catalytic decomposition reactions was best observed for UI and DL, L distribution with the increase in temperature. Whereas the highest UI was achieved at 350 ℃ by being 21 wt.% for non-catalytic decomposition, UI again was highest in the amount for the catalytic decomposition at the same temperature but it was less than 21 wt.% by being 13wt.%. Moreover, DL, L stayed more stable in amount for catalytic decomposition reactions by only a 12 % decline, whereas that was a 33 % decline for non-catalytic decomposition reactions.

In conclusion, in both non-catalytic, and catalytic decomposition reactions, the observation of an increase in PA, and LA concentration with the increase in temperature could be because, with the increase in temperature, high molecular weight products such as DL, L, and Meso L were further decomposed to lower molecular weight products such as PA, and LA. Moreover, previously mentioned UI products for catalytic decomposition reaction were U1, U2, and U4. U1 and U2 were first observed at 250 ℃ and their concentration increased with the increase in temperature to 300 ℃. After that temperature, both U1 and U2's concentrations began to decrease. U4 was first observed at 275 ℃, and its concentration increased with the increase in temperature.

The study conducted by Sivri (Sivri, 2023) showed that U3 and U6 were observed for non-catalytic decomposition reactions, whereas for Al-loaded silica aerogel catalyst used in decomposition reactions, U1, U4, U6, and another UI at 15.9 min retention time were observed. Naming of the UI products is performed as mentioned earlier for the given retention times. In Sivri's study mentioned no UI products were observed for Fe loaded silica aerogel catalyst used in the decomposition reactions. As seen, some differences were observed for the UI products that could be attributed to the use of bimetallic catalysts bearing both Al and Fe, which may contribute to differences in reaction mechanism.

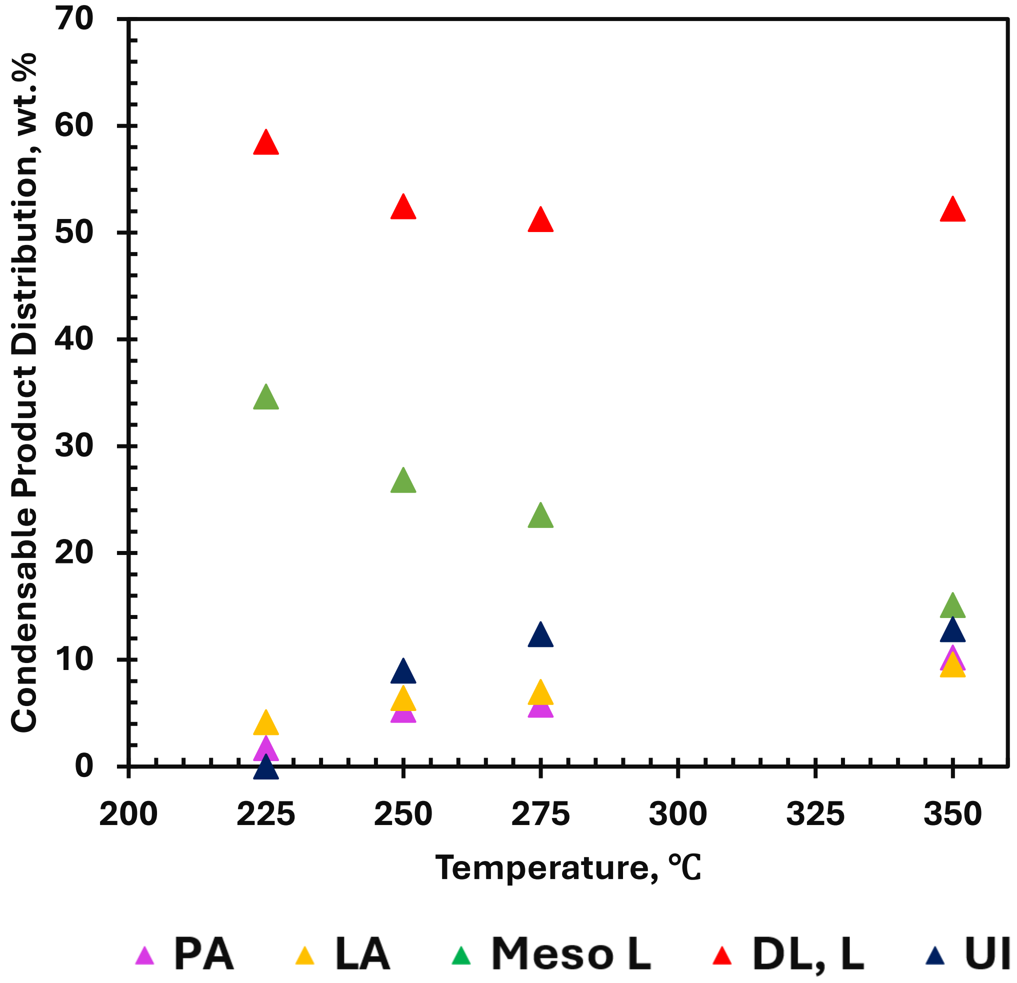

Figure 4.33. The effect of reaction temperature on the condensable product distributions in the presence of catalysts. (Catalyst: SimSAU0.5Al14.5Fe, 70rpm, 60 min, and ϑ_{Ar} = 50 ml/min)

Non-condensable products were analyzed during the reaction at the 15th and 50th minutes of the 60-minute reaction time. Non-condensable product analysis was conducted by using a thermal conductivity detector (TCD) in GC. The products observed are acetaldehyde, carbon monoxide, carbon dioxide, ethylene, and hydrogen. Figures 4.34 and 4.35 were achieved for non-catalytic decomposition reactions at the 15th min and 50th min of the 60-minute reaction time.

Figure 4.34 exhibits the effect of temperature on the non-condensable product distribution at the 15th minute of the reaction. The main products observed are acetaldehyde and carbon monoxide. Acetaldehyde concentration increased with the increase in temperature till 275 °C, and then declined to 72 mol % at 350 °C; however, carbon monoxide concentration decreased with the increase in temperature. The highest concentration of acetaldehyde was achieved at 275 °C as around 93 mol %. The highest concentration of carbon monoxide was obtained at 225 °C as 44.5 mol % and then declined to around 15 mol %. Moreover, with the increase in temperature, the concentration of carbon dioxide increased to around 12 mol %. The highest carbon dioxide concentration was achieved at 350 °C.

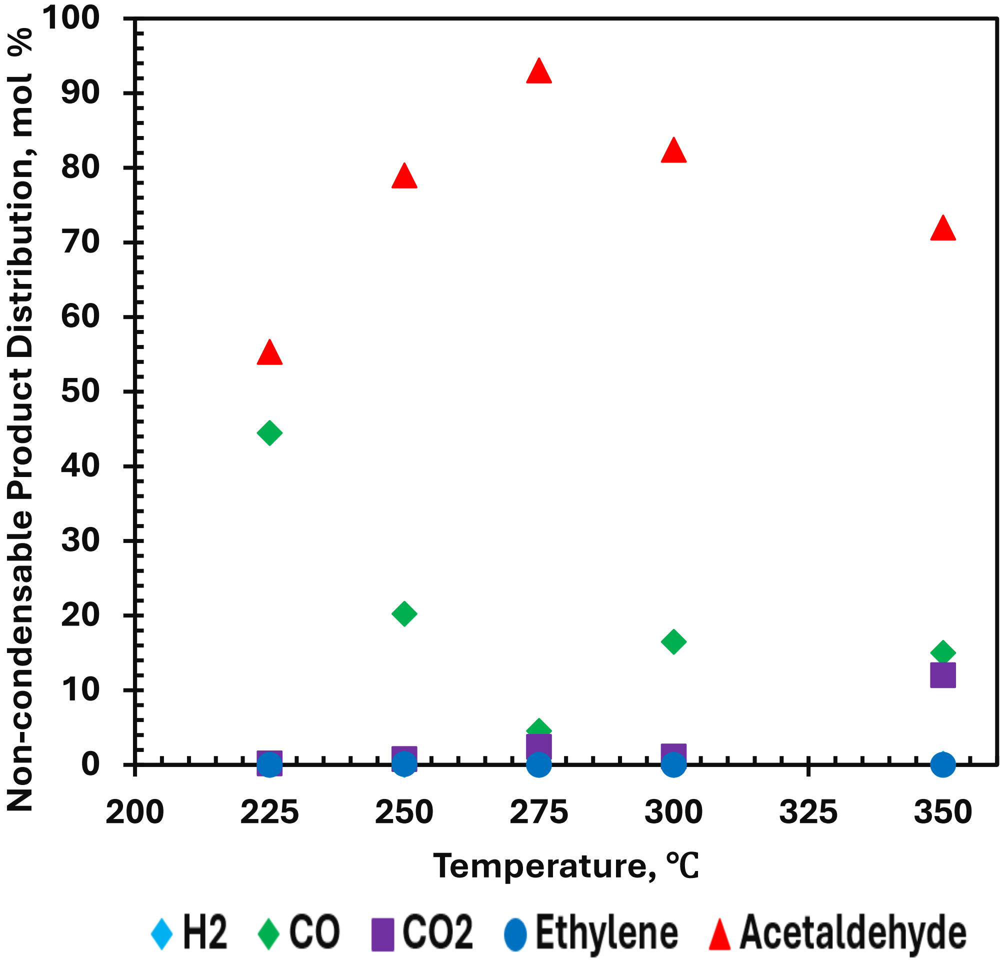

Figure 4.34. The effect of temperature on the non-condensable product distributions for t=15 min in the absence of catalysts. (70rpm, 60 min, and ϑ_{Ar} = 50 ml/min)

Considering the 50th minute of the reaction (Figure 4.35), the same main products were observed. Acetaldehyde concentration increased with the increase in temperature, whereas carbon monoxide concentration decreased with the increase in temperature. The highest amount of acetaldehyde was achieved at 300 ℃ by being 94 %, whereas the highest amount of carbon monoxide was obtained at 225 ℃ as 31 mol %. On the other hand, carbon dioxide concentration first decreases till 275 ℃ then increased with the increase in temperature. The highest carbon dioxide concentration was observed at 225 °C as around 7 mol %. Regarding other products, hydrogen, and ethylene were in trace amounts for both reaction times.

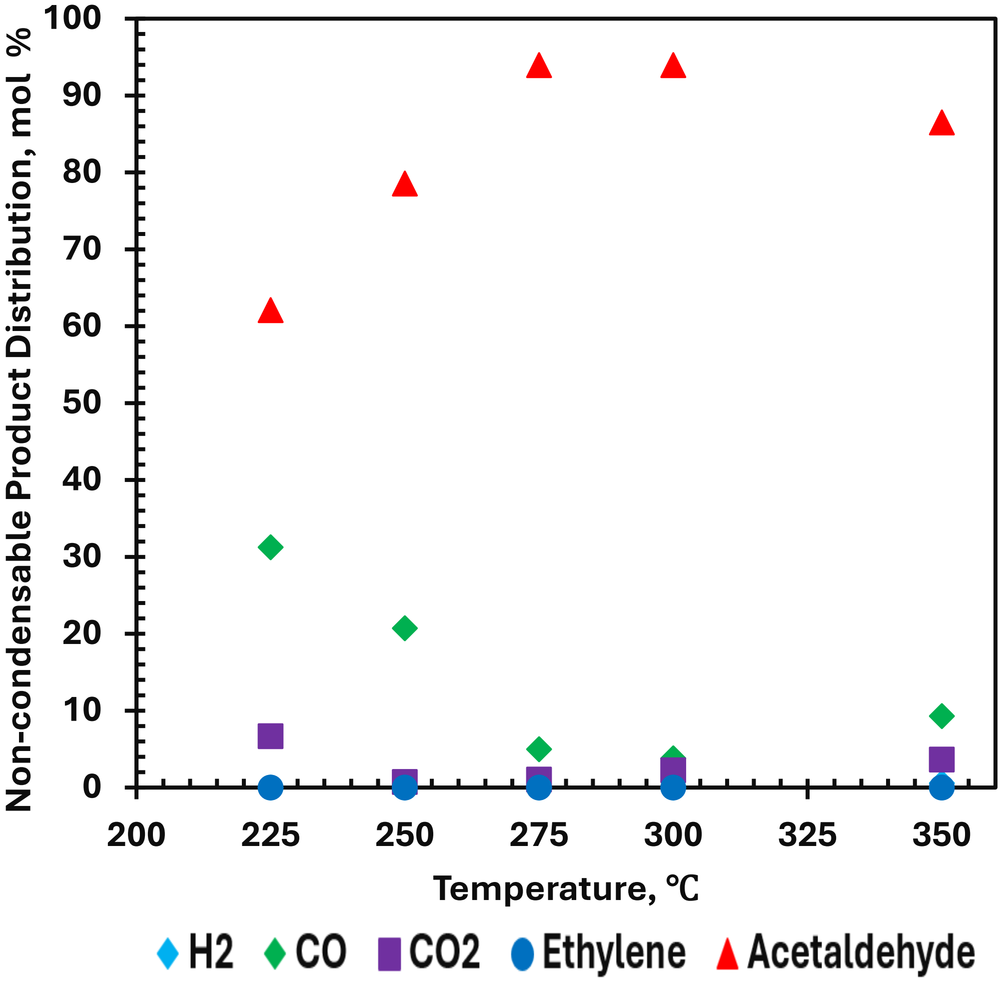

Figure 4.35. The effect of temperature on the non-condensable product distributions for t=50 min in the absence of catalysts. (70rpm, 60 min, and ϑ_{Ar} = 50 ml/min)

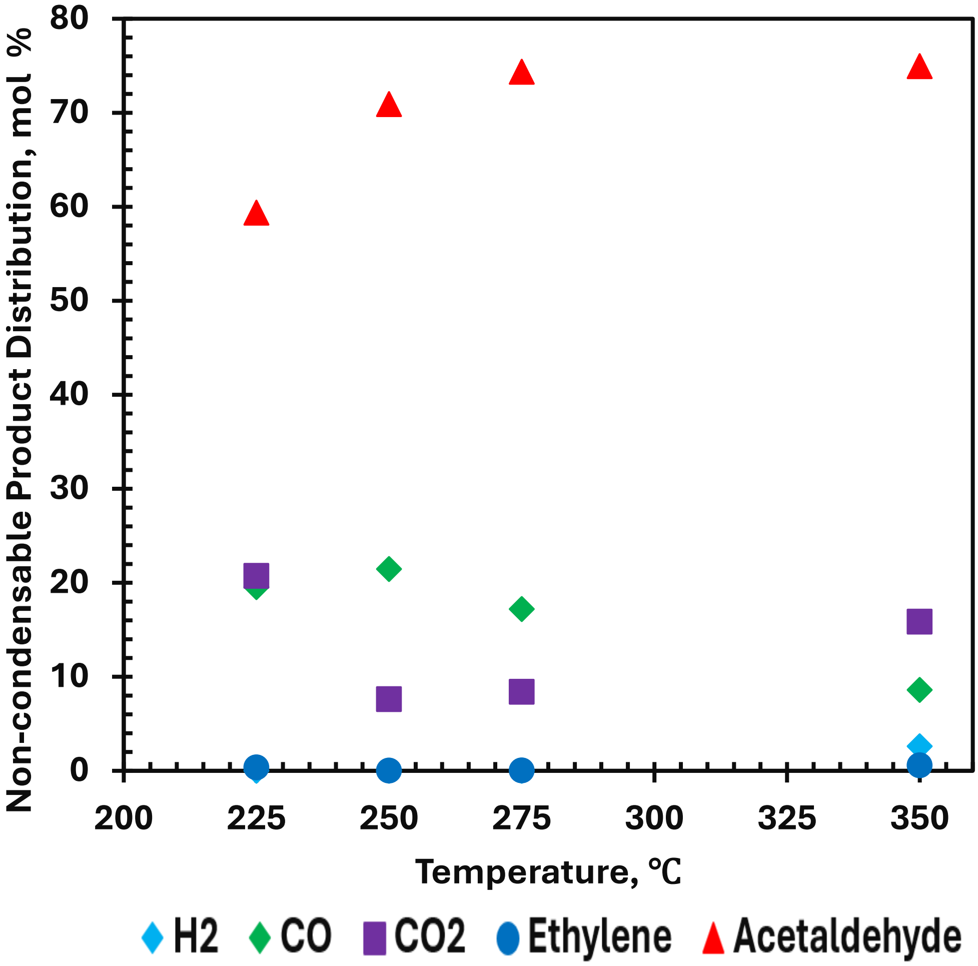

Figure 4.36. The effect of temperature on the non-condensable product distributions for t=15 min in the presence of catalysts. (Catalyst: SimSAU0.5Al14.5Fe, 70rpm, 60 min, and ϑ_{Ar} = 50 ml/min)

The same trend for all the mentioned products except carbon dioxide was also observed for catalytic decomposition reactions (Figures 4.36 & 4.37). Acetaldeheyde being major product with carbon monoxide, also hydrogen and carbon dioxide was observed at different temperatures. The hydrogen amount increased from 2 % to 7 % at the highest from the 15th min of the reaction to the 50th min of the reaction at 350°C. The highest amount of hydrogen was observed at that temperature. Carbon dioxide was higher in amount in earlier steps of the reaction, i.e., 15th min of the reaction, then it stabled around 6 %. The formation of more acetaldehyde with both an increase in the reaction time and the temperature could be attributed to the syngas formation within the decomposition reaction that can lead to non-selective acetaldehyde formation.

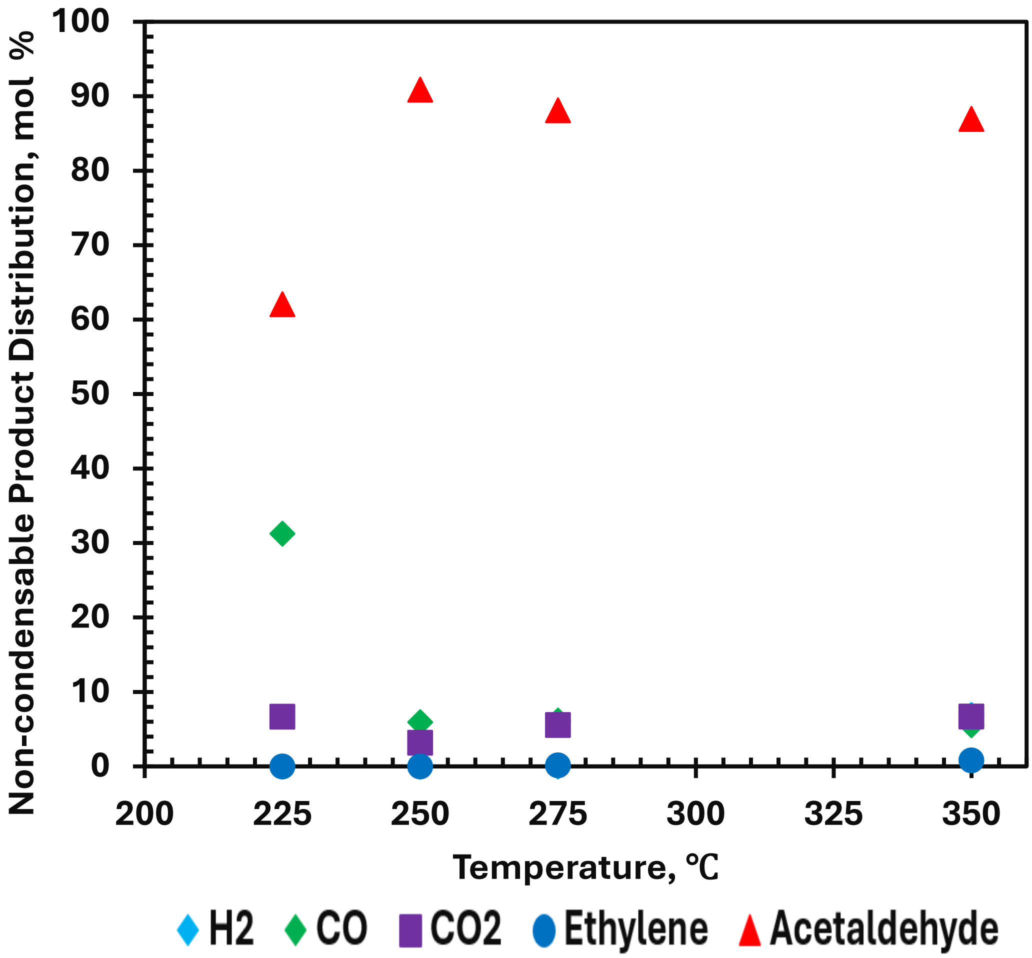

Figure 4.37. The effect of temperature on the non-condensable product distributions for t=50 min in the presence of catalysts. (Catalyst: SimSAU0.5Al14.5Fe, 70rpm, 60 min, and ϑ_{Ar} = 50 ml/min)

4.2.3 The Effect of Reaction Time on the Product Yield and Product Distribution

To observe the effects of the reaction time on product yield and product distribution, 2 different reaction times were studied. The main aim was to observe at which reaction time the solid remaining would be zero, i.e., solid yield becomes 0 wt.%. Therefore, SimSAU0.5Al14.5Fe catalyst was utilized at 225 ℃, with 50 ml/min argon flow rate, 5℃/min heating rate, and 70 rpm mixing rate.

As can be seen in Figure 4.38, the solid yield was around 11.5 % for a 60-minute reaction; however, increasing the reaction time to 120 minutes yielded no solid, which means that at those conditions, the limit reaction time to have zero solid remaining might be 120 minutes. Moreover, slight increases in condensable products were observed. This increase was from 51 wt.% to 58 wt.%. Eventually, a slight increase in non-condensable product amount was also observed by being from 37 wt.% to 41 wt.%. Those results indicate that although more solid was converted to other products, namely condensable and non-condensable, compared to 60-minute reactions, the whole conversion did not result in condensable as a whole. With the increase in reaction time, some of the condensable might be converted into non-condensable products.

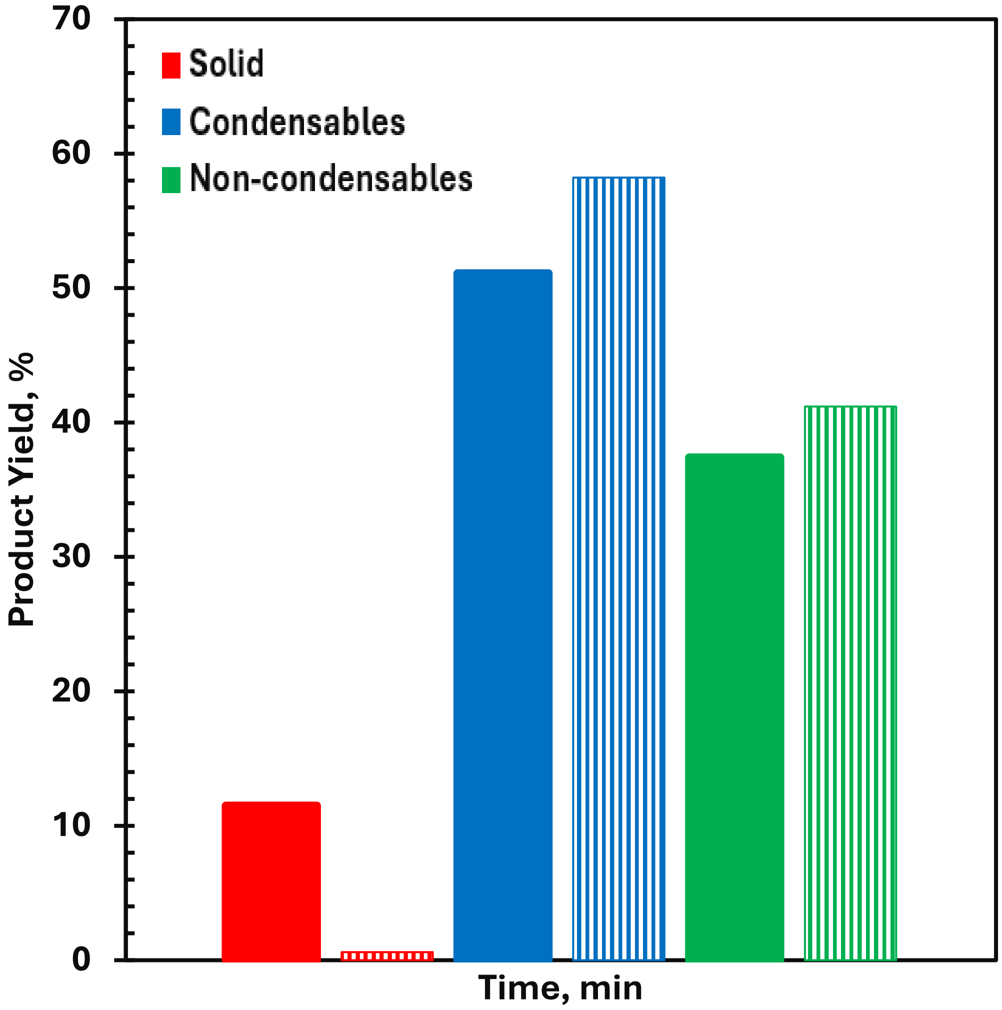

Figure 4.38. The effect of reaction time on product yields in the presence of catalysts: Filled box: 60 minutes reaction time, and vertical lined box: 120 minutes reaction time (Catalyst: SimSAU0.5Al14.5Fe, T=225 ℃, 70rpm, and ϑ_{Ar} = 50 ml/min)

Figure 4.39 shows the condensable product distribution of the 60-minute and 120-minute reactions. As can be seen, almost only detectable change was observed in the DL, L, and Meso L concentrations when the reaction time was increased. Moreover, around 1.2 wt.% increase in PA concentration was also observed with the increase in reaction time.

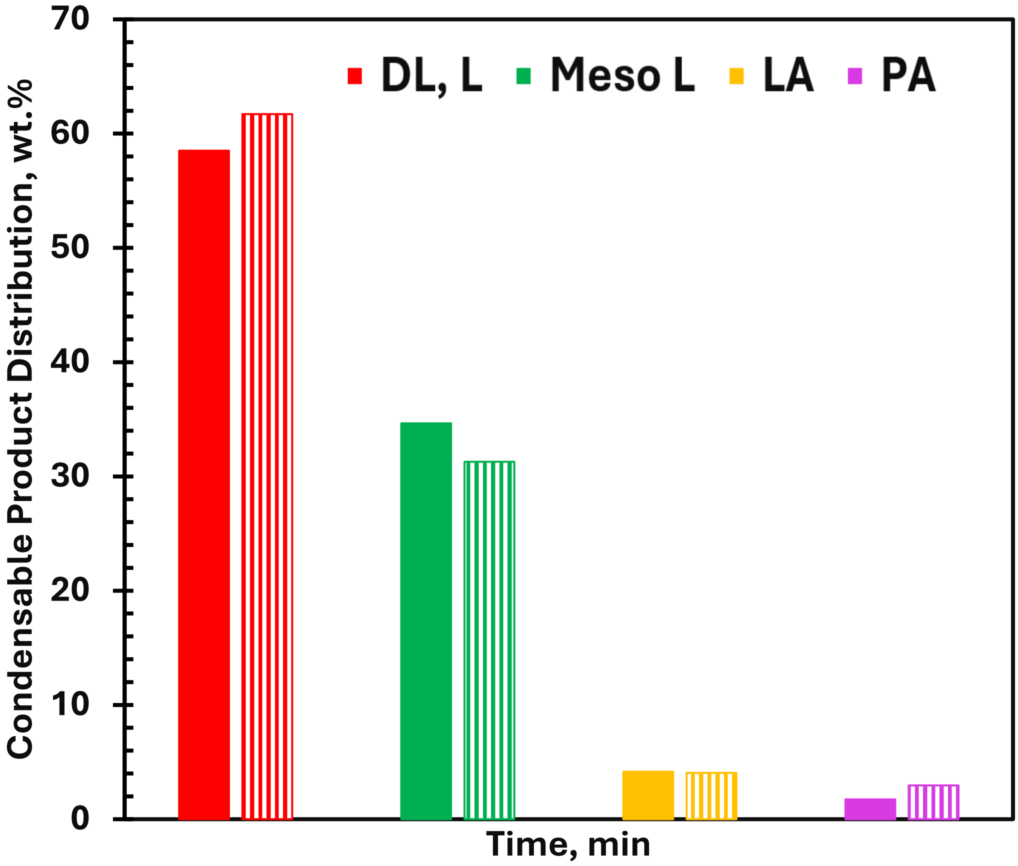

Figure 4.39. The effect of reaction time on condensable product distributions in the presence of catalysts: Filled box: 60 minutes reaction time, and vertical lined box: 120 minutes reaction time. (Catalyst: SimSAU0.5Al14.5Fe, 70rpm, 60 min, and ϑ_{Ar} = 50 ml/min)

Figure 4.40 shows the non-condensable product distribution regarding the 120-minute reaction. The main species are the same as what was mentioned prior in the effect of temperature on the degradation of PLA. In addition, with the increase in reaction time, less carbon monoxide and more acetaldehyde were observed. That could be due to the fact that it is known that acetaldehyde degrades into carbon monoxide and methane (Winkler & Hinshelwood, 1934). In addition, PLA degradation might be initiated by the cleavage of the C-O bond close to the ester group, and then the C-O bond breaking in the ester group, and cleavage of the C-C bond, which may result in mostly volatile byproducts such as carbon monoxide, carbon dioxide, and acetaldehyde (Li et al., 2022). Thus, no observation of methane and a stable amount of carbon dioxide could be attributed to the formation of syngas from which more acetaldehyde was produced.

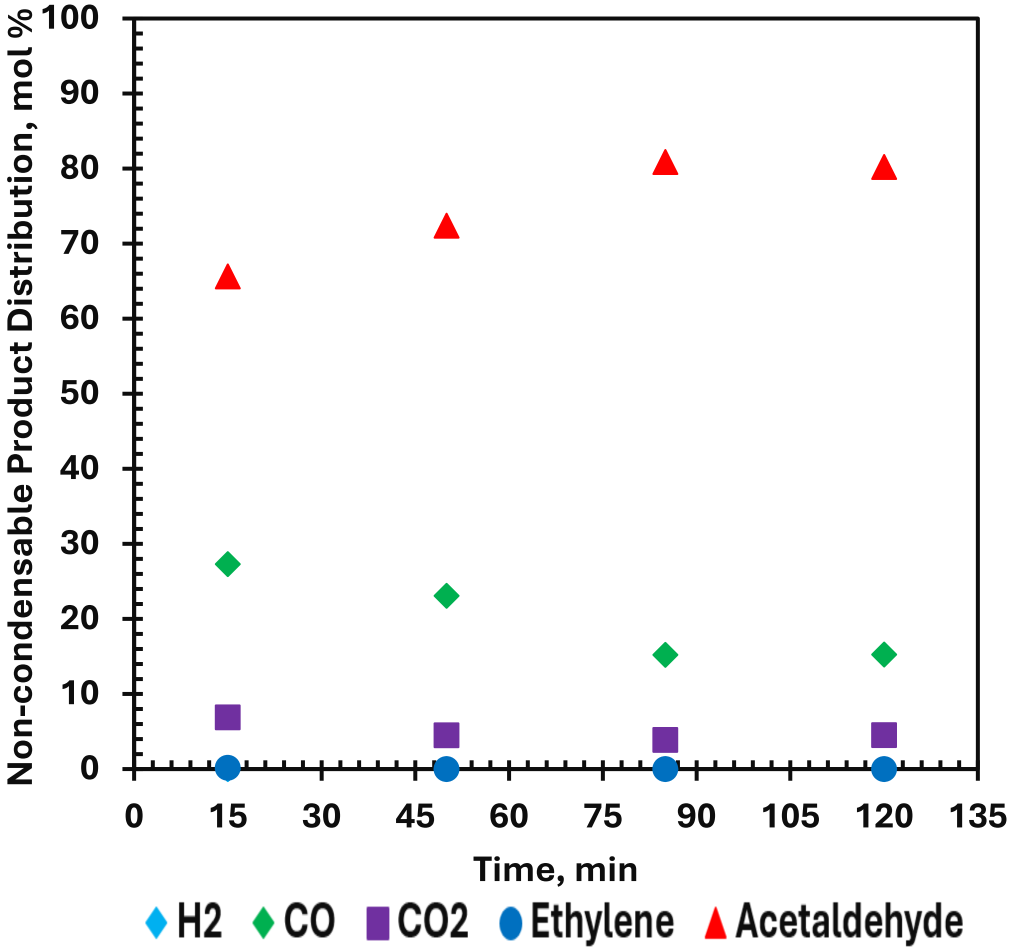

Figure 4.40. The effect of reaction time on the non-condensable product distributions at different times of the 120-minute reaction. (Catalyst: SimSAU0.5Al14.5Fe, 70rpm, 60 min, and ϑ_{Ar} = 50 ml/min)

4.2.4 Used Catalyst Characterization Results

Characterization of used catalysts was conducted using N_2 physisorption analysis and TGA. At the end of all the decomposition reactions, the catalysts were kept for further analysis. It was observed that catalysts that were brownish initially always changed color. Moreover, with the increase in temperature, the color changed from dark brown (225 ℃ used catalyst) into black color after usage in decomposition reactions. Therefore, coke deposition was anticipated and to ensure the analysis methods above-mentioned were decided to be utilized. First, N_2 physisorption to the used catalyst (SimSAU2Al13Fe and SimSAU0.5Al14.5Fe) at 225 °C (post-reaction) was applied, and the result can be seen in Figure 4.41. As expected, the loading capacity of both the used catalysts decreased compared to their fresh state. Hysteresis was observed at around 0.56 relative pressure (P/P_0) with no change in type compared to fresh catalysts (H1).

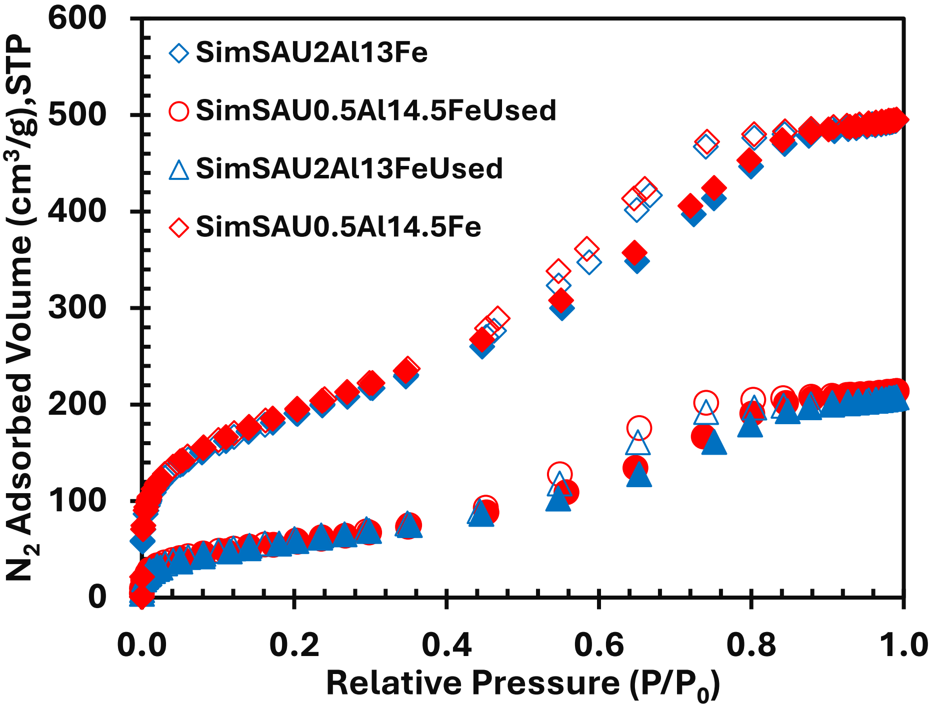

Figure 4.41. N_2 adsorption/desorption isotherms regarding fresh and used metal-loaded silica aerogels (Filled symbol: adsorption branch, empty symbol: desorption branch)

Figure 4.42 shows the pore size distribution of the silica aerogel, fresh SimSAU2Al13Fe catalyst, fresh SimSAU0.5Al14.5Fe catalyst, and the used catalysts regarding the mentioned two catalysts. As can be seen, the pores of the used catalysts were blocked compared to the fresh ones, which might be because of the coke deposition and low molecular weight solid products within the pores. Moreover, pore size distribution seems to peak around 4.64 nm, whereas there were two different peaks at 3.0 and 5.1 nm for the fresh ones. The change in pore size of the used catalysts compared to their fresh ones could be better observed by looking at Figure 4.43.

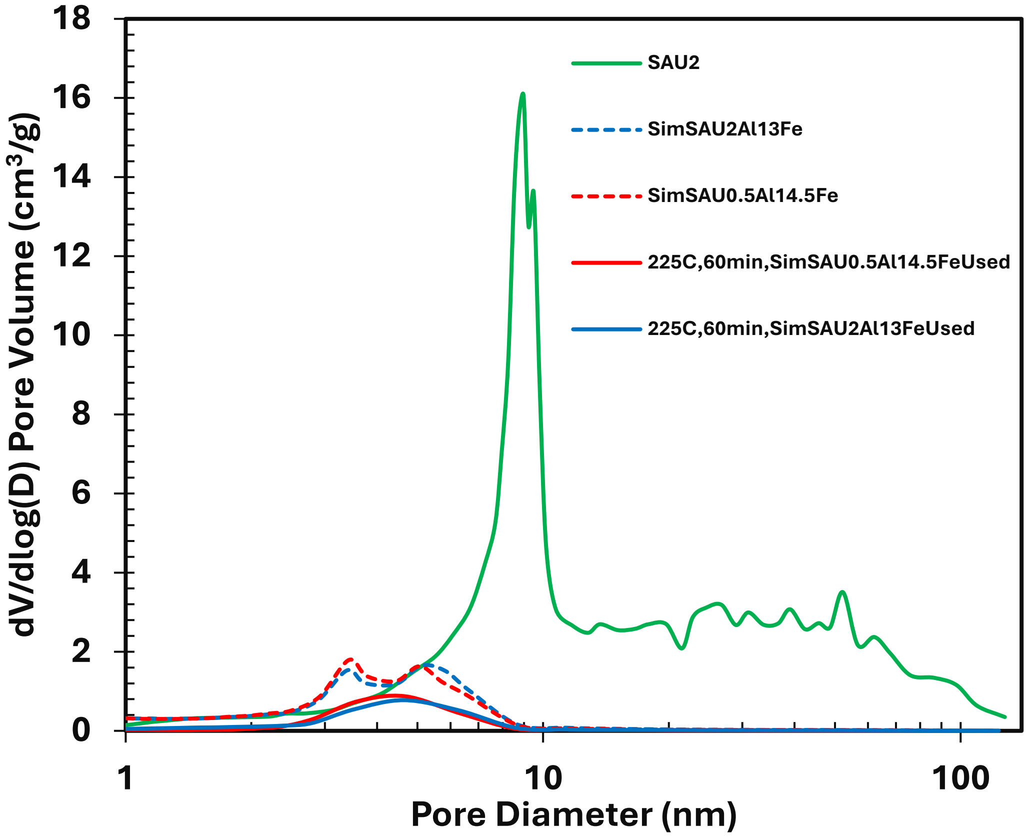

Figure 4.42. Pore size distribution of silica aerogel, fresh and used metal-loaded silica aerogels

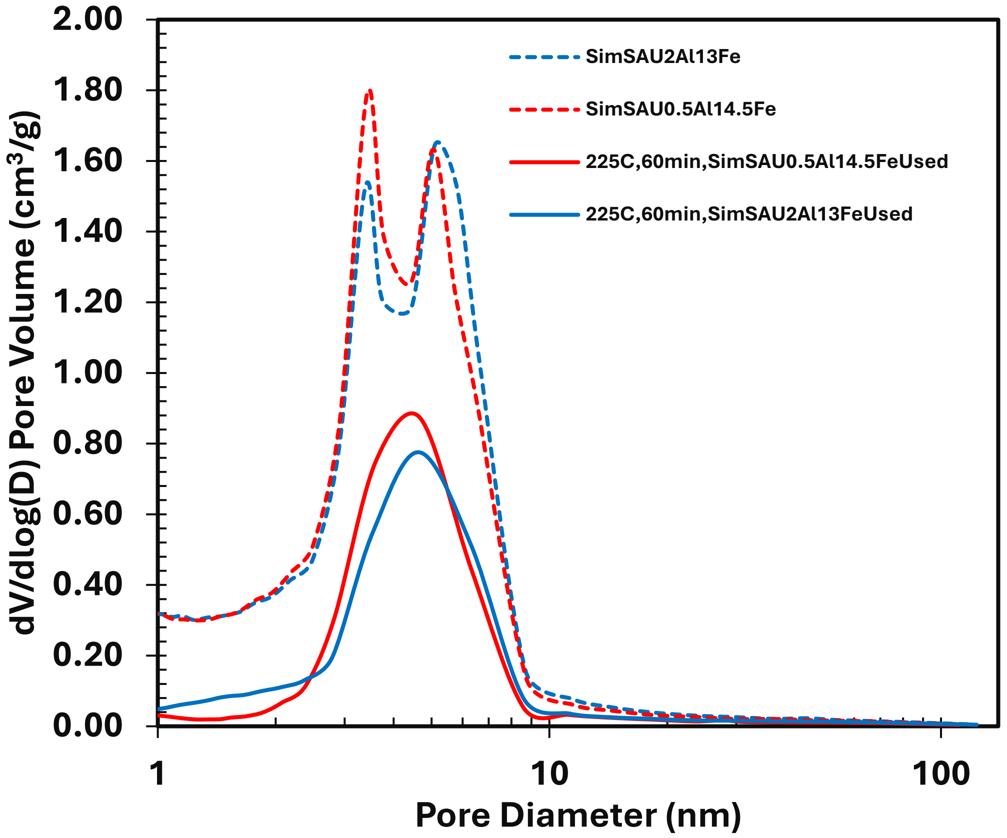

Figure 4.43. Pore size distribution of fresh and used metal-loaded silica aerogels

Eventually, to acquire more information about the cause of the pore blockage, TGA was carried out. Figure 4.44 shows the TGA results of the two used catalysts at different temperatures, namely 225 °C and 350 °C. Whereas the red line displays the used catalyst at 225 °C, the blue line exhibits the used catalyst at 350 °C. Amorphous carbon is known to burn after 300 °C (Moubark et al., 2015); therefore, around 8 % loss after 300 °C for the used catalyst at 350 °C could be attributed to the burning of the amorphous carbon deposited in the catalyst. However, when the used catalyst at 225 °C was considered, a different slope before 300 °C, around 20 % weight loss, was also observed. After 300 °C, around only 5 % weight loss was observed. Therefore, it is thought that besides amorphous carbon, low molecular weight solid products might also be available within the catalyst. The weight loss before 100 °C, around 5 %, for both used catalysts could be attributed to the moisture that might be available within the materials.

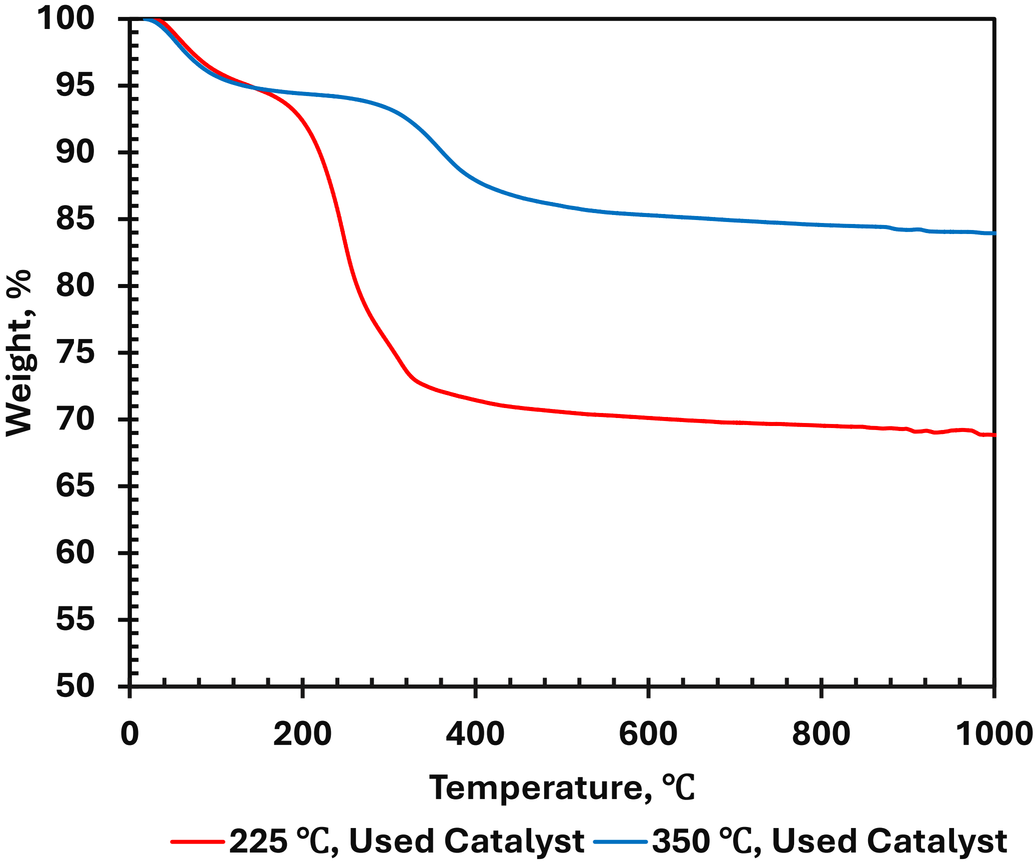

Figure 4.44. TGA result of used catalysts under air medium

CHAPTER 5

CONCLUSIONS

Within the scope of this thesis, as a support material, porous silica aerogel was selected and synthesized by the sol-gel method. Different batches of support material were characterized by both N_2 physisorption analysis and FTIR analysis to get information about the physical properties of the support material. Following that, wet impregnation was carried out to load silica aerogel with iron and aluminum to obtain bimetallic catalysts. Bimetallic catalysts were characterized by N_2 physisorption analysis, XRD, and SEM. Moreover, the activity of the catalysts was tested first by TGA and then in the depolymerization of PLA in the pyrolysis system. Some crucial findings are as follows:

- N_2 physisorption analysis showed that produced silica aerogels have 894 ∓ 123.4 m^2/g multipoint BET surface area, 3.65 ∓ 0.58 cm^3/g BJH desorption average pore volume and 9.66 ∓ 0.5 nm BJH desorption average pore diameter with Type IV isotherm. This suggests that the synthesized silica aerogels are reproducible.
- N_2 physisorption of the synthesized metal-loaded silica aerogel showed that the hysteresis type of silica aerogel shifted from H3 to H1 with the metal loading, which indicates a narrower pore size. Besides, metal-loaded silica aerogels have 2.95 ∓ 0.2 nm BJH desorption average pore diameter.
- It is found that the TGA curve shifted to the left by a catalyst in PLA degradation compared to non-catalytic PLA degradation, indicating the decrease in activation energy of the PLA degradation reaction with the use of a catalyst.
- XRD patterns of all the synthesized catalysts showed the phases, namely Fe_2O_3 and Fe_3O_4.

- Decreased Al/Fe weight ratio resulted in more condensable and less solid products.
- Temperature effect on the PLA depolymerization reactions with the SimSAU0.5Al14.5Fe catalyst showed the following results:
  - Increase in temperature resulted in a decrease in the condensable product yield from 51 % (at 225 °C) to 34 % (at 350 °C). In addition, an increase in temperature resulted in higher non-condensable product yield from 37 % (at 225 °C) to 66 % (at 350 °C).
  - No solid was observed after a reaction temperature of 250°C.
  - Condensable products are DL, L, Meso Lactide, LA, and PA with unidentified products.
  - Non-condensable products are acetaldehyde, carbon monoxide, carbon dioxide, hydrogen, and trace amounts of ethylene.
  - The impact of increasing the temperature on the distribution of the condensable products is as follows:
    - DL, L concentration within the condensable product decreased from 58 wt.% (at 225 °C) to 52 wt.% (at 350 °C).
    - Meso L concentration within the condensable product decreased from 35 wt.% (at 225 °C) to 15 wt.% (at 350 °C).
    - PA concentration within the condensable product increased from 2 wt.% (at 225 °C) to 10 wt.% (at 350 °C).
    - LA concentration within the condensable product increased from 4 wt.% (at 225 °C) to 10 wt.% (at 350 °C).
    - UI composition within the condensable product increased from 0 wt.% (at 225 °C) to 13 wt.% (at 350 °C).
  - The impact of increasing the temperature on the distribution of non-condensable products is as follows:
    - Acetaldehyde concentration within the non-condensable product increased from 62 mol % (at 225 °C) to 95 mol % (at 300 °C), and then declined to 87 mol % (at 350 °C).

        - Carbon monoxide concentration within the non-condensable product decreased from 31 mol % (at 225 °C) to 6 mol % (at 350 °C).
        - Carbon dioxide concentration within the non-condensable product initially declined from 225 °C to 250 °C then it began to increase slowly.
        - A trace amount of ethylene was observed. Moreover, the highest concentration of hydrogen is around 7 mol % at 350 °C.

- The impact of increasing the reaction time on the yield of the solid, condensable, and non-condensable products is as follows:
    - Solid yield decreased from 11.5 % to 0 %, which means no solid was observed when reaction time was increased from 60 minutes to 120 minutes.
    - Condensable product yield increased from 51 % to 58 %.
    - Non-condensable product yield increased from 37 % to 41 %.
- Coke deposition was observed. At lower temperatures (225 °C) carbon accumulation within the pores was less compared to higher temperatures.
- Finally, the highest lactide yield was observed at 225 °C as 48 % with 17 % Meso L, and 31 % DL, L yields accounting for the 48 % yield.

REFERENCES

Bråte, I. L., Halsband, C., Allan, I., & Thomas, K. (2014). Report made for the Norwegian Environment Agency: Microplastics in marine environments; Occurrence, distribution and effects.

Cam, D., & Marucci, M. (1997). Influence of residual monomers and metals on poly (l-lactide) thermal stability. *Polymer*, *38*(8), 1879-1884. https://doi.org/10.1016/S0032-3861(96)00711-2

Chang, S., Clair, B., Ruelle, J., Beauchêne, J., Di Renzo, F., Quignard, F., Zhao, G., Yamamoto, H., & Gril, J. (2009). Mesoporosity as a new parameter for understanding tension stress generation in trees. *Journal of Experimental Botany*, *60*(11), 3023-3030. https://doi.org/10.1093/jxb/erp133

Chellali, J. E., Alverson, A. K., & Robinson, J. R. (2022). Zinc Aryl/Alkyl β-diketiminates: Balancing Accessibility and Stability for High-Activity Ring-Opening Polymerization of rac-Lactide. *ACS Catalysis*, *12*(9), 5585–5594. https://doi.org/10.1021/acscatal.2c00858

Cho, S., Kim, Y., Lee, S., Andrew Lin, K., Chen, W., Jung, S., Lee, D., Hyun Moon, D., Jeon, Y. J., & Kwon, E. E. (2023). Virtuous utilization of carbon dioxide in pyrolysis of polylactic acid. *Chemical Engineering Journal*, *466*, 143307. https://doi.org/10.1016/j.cej.2023.143307

Choi, J., & Suh, D. J. (2007). Catalytic applications of aerogels. *Catalysis Surveys from Asia*, *11*(3), 123–133. https://doi.org/10.1007/s10563-007-9024-2

Değirmencioğlu, P. (2018). *Methanol steam reforming over silica aerogel supported catalyst for hydrogen production*. M.S. - Master of Science. Middle East Technical University.

Dijkstra, P. J., Du, H., & Feijen, J. (2010). Single site catalysts for stereoselective ring-opening polymerization of lactides. *Polymer Chemistry*, *2*(3), 520–527. https://doi.org/10.1039/c0py00204f

Ermiş, S. (2022). *Dimethyl ether production from synthesis gas with bifunctional catalyst mixtures*. M.S. - Master of Science. Middle East Technical University.

European bioplastics conference. (2021). *Bioplastics Market Development*. Retrieved December 30, 2024, from https://www.european-bioplastics.org/bioplastics-market-development-update-2024/

Fan, Y., Nishida, H., Mori, T., Shirai, Y., & Endo, T. (2004). Thermal degradation of poly(L-lactide): Effect of alkali earth metal oxides for selective L,L-lactide formation. *Polymer*, *45*(4), 1197–1205. https://doi.org/10.1016/j.polymer.2003.12.058

Global Elastomeric Products, Inc. (2016). Elastomer Properties and Industry Applications of Elastomers - Global Elastomeric Products. Retrieved December 30, 2024, from https://www.globaleee.com/global-news/-history/elastomers-applications

Gurav, J. L., Jung, K., Park, H., Kang, E. S., & Nadargi, D. Y. (2010). Silica Aerogel: Synthesis and Applications. *Journal of Nanomaterials*, *2010*(1), 409310. https://doi.org/10.1155/2010/409310

Hasan, M., Rasul, M., Khan, M., Ashwath, N., & Jahirul, M. (2021). Energy recovery from municipal solid waste using pyrolysis technology: A review on current status and developments. *Renewable and Sustainable Energy Reviews*, *145*, 111073. https://doi.org/10.1016/j.rser.2021.111073

Hopewell, J., Dvorak, R., & Kosior, E. (2009). Plastics recycling: Challenges and opportunities. In *Philosophical Transactions of the Royal Society B: Biological Sciences* (Vol. 364, Issue 1526, pp. 2115–2126). Royal Society. https://doi.org/10.1098/rstb.2008.0311

Horizon. (2023). *Global Polylactic Acid Market Size & Outlook, 2023-2030*. Retrieved December 30, 2024, from https://www.grandviewresearch.com/horizon/outlook/polylactic-acid-market-size/global

Hüsing, N., & Schubert, U. (1998). Aerogels—Airy Materials: Chemistry, Structure, and Properties. *Angewandte Chemie International Edition*, *37*(1-2), 22-45. https://doi.org/10.1002/(SICI)1521-3773(19980202)37:1/2<22::AID-ANIE22>3.0.CO;2-I

Jamshidian, M., Tehrany, E. A., Imran, M., Jacquot, M., & Desobry, S. (2010). Poly-Lactic Acid: Production, applications, nanocomposites, and release studies. *Comprehensive Reviews in Food Science and Food Safety*, *9*(5), 552–571. https://doi.org/10.1111/j.1541-4337.2010.00126.x

Khouri, N. G., Bahú, J. O., Blanco-Llamero, C., Severino, P., Concha, V. O., & Souto, E. B. (2024). Polylactic acid (PLA): Properties, synthesis, and biomedical applications – A review of the literature. *Journal of Molecular Structure*, *1309*, 138243. https://doi.org/10.1016/j.molstruc.2024.138243

Kibria, M. G., Masuk, N. I., Safayet, R., Nguyen, H. Q., & Mourshed, M. (2023). Plastic Waste: Challenges and Opportunities to Mitigate Pollution and Effective Management. *International Journal of Environmental Research*, *17*(1). https://doi.org/10.1007/s41742-023-00507-z

Koebel, M., Rigacci, A., & Achard, P. (2012). Aerogel-based thermal superinsulation: An overview. In *Journal of Sol-Gel Science and Technology* (Vol. 63, Issue 3, pp. 315–339). https://doi.org/10.1007/s10971-012-2792-9

Kopinke, F., Remmler, M., Mackenzie, K., Möder, M., & Wachsen, O. (1996). Thermal decomposition of biodegradable polyesters—II. Poly(lactic acid). *Polymer Degradation and Stability*, *53*(3), 329-342. https://doi.org/10.1016/0141-3910(96)00102-4

Kržan, A. (2012). *Biodegradable polymers and plastics*. Retrieved December 30, 2024, from https://icmpp.ro/sustainableplastics/files/Biodegradable_plastics_and_polymers.pdf

Kumari, S., Rao, A., Kaur, M., & Dhania, G. (2023). Petroleum-Based Plastics Versus Bio-Based Plastics: A Review. In *Nature Environment and Pollution Technology* (Vol. 22, Issue 3, pp. 1111–1124). Technoscience Publications. https://doi.org/10.46488/NEPT.2023.v22i03.003

Li, C., Liu, Q., Gong, W., Zhou, Z., Yao, Z., & Meng, X. (2022). Study on the atomic scale of thermal and thermo-oxidative degradation of polylactic acid via reactive molecular dynamics simulation. *Thermochimica Acta*, *709*, 179144. https://doi.org/10.1016/j.tca.2021.179144

Lowell, S., Shields, J.E., Thomas, M.A., Thommes, M. (2004). Adsorption Isotherms. In: Characterization of Porous Solids and Powders: Surface Area, Pore Size and Density. Particle Technology Series, vol 16. Springer, Dordrecht. https://doi.org/10.1007/978-1-4020-2303-3_3

Luckachan, G. E., & Pillai, C. K. S. (2011). Biodegradable Polymers- A Review on Recent Trends and Emerging Perspectives. *Journal of Polymers and the Environment*, *19*(3), 637–676. https://doi.org/10.1007/s10924-011-0317-1

Maleki, H., Durães, L., García-González, C. A., del Gaudio, P., Portugal, A., & Mahmoudi, M. (2016). Synthesis and biomedical applications of aerogels: Possibilities and challenges. In *Advances in Colloid and Interface Science* (Vol. 236, pp. 1–27). Elsevier B.V. https://doi.org/10.1016/j.cis.2016.05.011

Maleki, H., & Hüsing, N. (2018). Current status, opportunities and challenges in catalytic and photocatalytic applications of aerogels: Environmental protection aspects. *Applied Catalysis B: Environmental*, *221*, 530-555. https://doi.org/10.1016/j.apcatb.2017.08.012

McKeown, P., & Jones, M. D. (2020). The Chemical Recycling of PLA: A Review. *Sustainable Chemistry*, *1*(1), 1-22. https://doi.org/10.3390/suschem1010001

McNeill, I., & Leiper, H. (1985). Degradation studies of some polyesters and polycarbonates—2. Polylactide: Degradation under isothermal conditions, thermal degradation mechanism and photolysis of the polymer. *Polymer Degradation and Stability*, *11*(4), 309-326. https://doi.org/10.1016/0141-3910(85)90035-7

Michler, G. H., & Baltá-Calleja, F. J. (2012). General importance of polymers and trends. In *Carl Hanser Verlag GmbH & Co. KG eBooks* (pp. 1–33). https://doi.org/10.3139/9783446428447.001

Moubark, M. (2015). Sulfonated Ion Exchange Polystyrene Composite Resin for Calcium Hardness Removal. *International Journal of Emerging Technology and Advanced Engineering*, *5*, 20–29.

Namazi, H. (2017). Polymers in our daily life. *Bioimpacts*, *7*(2), 73–74. https://doi.org/10.15171/bi.2017.09

Obalı, Z. (2010). *Synthesis of aluminum incorporated mesoporous catalysts for pyrolysis of polypropylene*. Ph.D. - Doctoral Program. Middle East Technical University.

OECD (2022), *Global Plastics Outlook: Policy Scenarios to 2060*, OECD Publishing, Paris, https://doi.org/10.1787/aa1edf33-en

Pajonk, G. M. (1991). Aerogel catalysts. *Applied Catalysis*, *72*(2), 217–266. https://doi.org/10.1016/0166-9834(91)85054-Y

Pajonk, G. (1999). Some catalytic applications of aerogels for environmental purposes. *Catalysis Today*, *52*(1), 3-13. https://doi.org/10.1016/S0920-5861(99)00057-7

Pang, X., Zhuang, X., Tang, Z., & Chen, X. (2010). Polylactic acid (PLA): Research, development and industrialization. *Biotechnology Journal*, *5*(11), 1125–1136. https://doi.org/10.1002/biot.201000135

PerkinElmer. (2010). Thermogravimetric Analysis (TGA) TGA 8000 TGA 4000 STA 6000 / STA 8000 The Thermogravimetric Instrument Family. *PerkinElmer*. Retrieved December 30, 2024, from https://resources.perkinelmer.com/lab-solutions/resources/docs/faq_beginners-guide-to-thermogravimetric-analysis_009380c_01.pdf

Rahman, M. R., Taib, N. a. B., Bakri, M. K. B., & Taib, S. N. L. (2020). Importance of sustainable polymers for modern society and development. In *Elsevier eBooks* (pp. 1–35). https://doi.org/10.1016/b978-0-12-820338-5.00001-1

Redwing. (2024). Basic Polymer Structure | MATSE 81: Materials In Today's World. Retrieved December 30, 2024, from https://www.e-education.psu.edu/matse81/node/2210

Research Nester. (2024). Polymers Market Size & Share, Growth Forecasts 2037. Retrieved December 30, 2024, from https://www.researchnester.com/reports/polymers-market/1387

Ryan, A. J. & TA Instruments – Waters LLC. (2021). Thermogravimetric Analysis (TGA) Theory and Applications. *TAINSTRUMENTS.COMTAINSTRUMENTS.COM*. Retrieved December 30, 2024, from https://www.tainstruments.com/wp-content/uploads/San-Jose-Thermal-TGA.pdf

Safwan-Ul-Iman, N., Rahman, S., Rahman, M. Z., Saha, B., & Salsabil, Z. (2024). Recent development trends on polymeric materials—Investigation of properties and applications. In *Elsevier eBooks* (pp. 125–152). https://doi.org/10.1016/b978-0-323-96020-5.00145-x

Samir, A., Ashour, F. H., Hakim, A. A., & Bassyouni, M. (2022). Recent advances in biodegradable polymers for sustainable applications. *Npj Materials Degradation*, *6*(1), 1-28. https://doi.org/10.1038/s41529-022-00277-7

Schneider, M., & Baiker, A. (1995). Aerogels in Catalysis. *Catalysis Reviews*, *37*(4), 515–556. https://doi.org/10.1080/01614949508006450

Silva, R. R. A., Marques, C. S., Arruda, T. R., Teixeira, S. C., & De Oliveira, T. V. (2023). Biodegradation of Polymers: Stages, Measurement, Standards and Prospects. *Macromol—A Journal of Macromolecular Research*, *3*(2), 371–399. https://doi.org/10.3390/macromol3020023

Sivri, S. (2023). *Recycling of Polymer Waste Using Different Techniques*. Ph.D. - Doctoral Program. Middle East Technical University.

Sivri, S., Dilek, C. & Sezgi, N. (2019). Synthesis and Characterization of Aluminum Containing Silica Aerogel Catalysts for Degradation of PLA. *International Journal of Chemical Reactor Engineering*, *17*(5), 20180163. https://doi.org/10.1515/ijcre-2018-0163

Su, T., Lu, G., Sun, K., Wu, P., & Cai, C. (2023). Boosting the selective catalytic pyrolysis of plastic waste polylactic acid to monomer. *Journal of Environmental Chemical Engineering*, *11*(6), 111397. https://doi.org/10.1016/j.jece.2023.111397

Sun, C., Wei, S., Tan, H., Huang, Y., & Zhang, Y. (2022). Progress in upcycling polylactic acid waste as an alternative carbon source: A review. *Chemical Engineering Journal*, *446*, 136881. https://doi.org/10.1016/j.cej.2022.136881

Statista. (2021). Global production capacity shares of biodegradable plastics 2019, by material. Retrieved December 30, 2024, from https://www.statista.com/statistics/1283701/global-bioplastic-production-capacity-shares-by-material/

Tan, L., Yu, X., Wan, P., & Yang, K. (2013). Biodegradable Materials for Bone Repairs: A Review. *Journal of Materials Science and Technology*, *29*(6), 503–513. https://doi.org/10.1016/j.jmst.2013.03.002

Thommes, M., & Cychosz, K. A. (2014). Physical adsorption characterization of nanoporous materials: Progress and challenges. *Adsorption*, *20*(2–3), 233–250. https://doi.org/10.1007/s10450-014-9606-z

Tyler, B., Gullotti, D., Mangraviti, A., Utsuki, T., & Brem, H. (2016). Polylactic acid (PLA) controlled delivery carriers for biomedical applications. *Advanced Drug Delivery Reviews*, *107*, 163–175. https://doi.org/10.1016/j.addr.2016.06.018

Van Krevelen, D., & Nijenhuis, K. T. (2009). Typology of Polymers. In *Elsevier eBooks* (pp. 7–47). https://doi.org/10.1016/b978-0-08-054819-7.00002-9

Walker, T. R. (2021). (Micro)plastics and the UN Sustainable Development Goals. *Current Opinion in Green and Sustainable Chemistry*, *30*, 100497. https://doi.org/10.1016/j.cogsc.2021.100497

Wang, B., Liu, W., & Zhang, M. (2024). Application of carbon-based adsorbents in the remediation of micro- and nanoplastics. *Journal of Environmental Management*, *349*, 119522. https://doi.org/10.1016/j.jenvman.2023.119522

Winkler, C. A., & Hinshelwood, C. N. (1934). The thermal decomposition of acetaldehyde. *Proceedings of the Royal Society of London a Mathematical and Physical Sciences*, *149*(867), 355–359. https://doi.org/10.1098/rspa.1935.0067

APPENDICES

A. XRD Data

Table A.1 XRD Data of Silicon Oxide

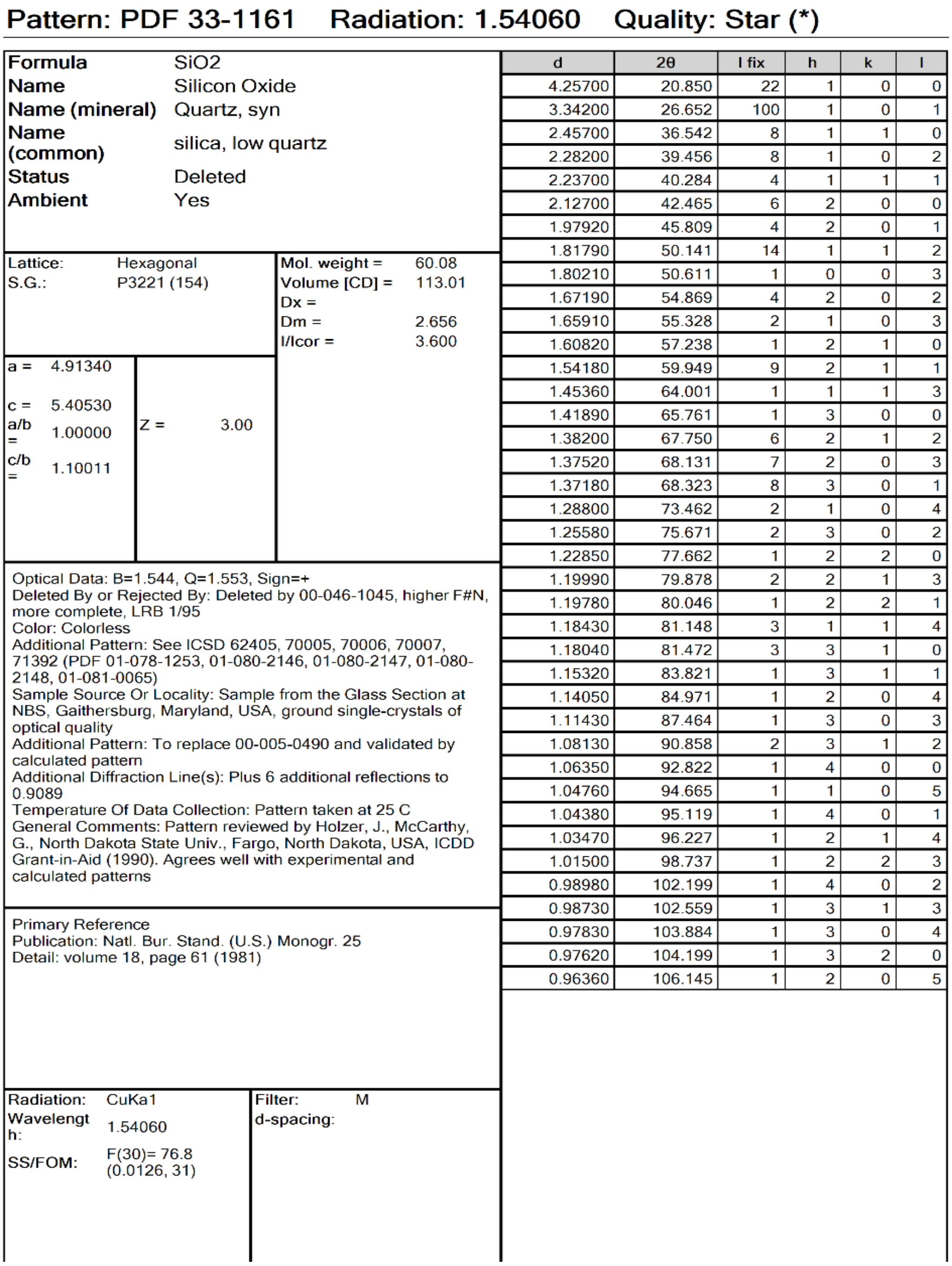

Pattern: PDF 33-1161 Radiation: 1.54060 Quality: Star (*)

Formula	SiO2
Name	Silicon Oxide
Name (mineral)	Quartz, syn
Name (common)	silica, low quartz
Status	Deleted
Ambient	Yes

Lattice: Hexagonal
S.G.: P3221 (154)

Mol. weight = 60.08
Volume [CD] = 113.01
Dx =
Dm = 2.656
I/Icor = 3.600

a = 4.91340
c = 5.40530
a/b = 1.00000
c/b = 1.10011
Z = 3.00

Optical Data: B=1.544, Q=1.553, Sign=+
Deleted By or Rejected By: Deleted by 00-046-1045, higher F#N, more complete, LRB 1/95
Color: Colorless
Additional Pattern: See ICSD 62405, 70005, 70006, 70007, 71392 (PDF 01-078-1253, 01-080-2146, 01-080-2147, 01-080-2148, 01-081-0065)
Sample Source Or Locality: Sample from the Glass Section at NBS, Gaithersburg, Maryland, USA, ground single-crystals of optical quality
Additional Pattern: To replace 00-005-0490 and validated by calculated pattern
Additional Diffraction Line(s): Plus 6 additional reflections to 0.9089
Temperature Of Data Collection: Pattern taken at 25 C
General Comments: Pattern reviewed by Holzer, J., McCarthy, G., North Dakota State Univ., Fargo, North Dakota, USA, ICDD Grant-in-Aid (1990). Agrees well with experimental and calculated patterns

Primary Reference
Publication: Natl. Bur. Stand. (U.S.) Monogr. 25
Detail: volume 18, page 61 (1981)

Radiation: CuKa1
Wavelength: 1.54060
SS/FOM: F(30)= 76.8 (0.0126, 31)

Filter: M
d-spacing:

d	2θ	I fix	h	k	l
4.25700	20.850	22	1	0	0
3.34200	26.652	100	1	0	1
2.45700	36.542	8	1	1	0
2.28200	39.456	8	1	0	2
2.23700	40.284	4	1	1	1
2.12700	42.465	6	2	0	0
1.97920	45.809	4	2	0	1
1.81790	50.141	14	1	1	2
1.80210	50.611	1	0	0	3
1.67190	54.869	4	2	0	2
1.65910	55.328	2	1	0	3
1.60820	57.238	1	2	1	0
1.54180	59.949	9	2	1	1
1.45360	64.001	1	1	1	3
1.41890	65.761	1	3	0	0
1.38200	67.750	6	2	1	2
1.37520	68.131	7	2	0	3
1.37180	68.323	8	3	0	1
1.28800	73.462	2	1	0	4
1.25580	75.671	2	3	0	2
1.22850	77.662	1	2	2	0
1.19990	79.878	2	2	1	3
1.19780	80.046	1	2	2	1
1.18430	81.148	3	1	1	4
1.18040	81.472	3	3	1	0
1.15320	83.821	1	3	1	1
1.14050	84.971	1	2	0	4
1.11430	87.464	1	3	0	3
1.08130	90.858	2	3	1	2
1.06350	92.822	1	4	0	0
1.04760	94.665	1	1	0	5
1.04380	95.119	1	4	0	1
1.03470	96.227	1	2	1	4
1.01500	98.737	1	2	2	3
0.98980	102.199	1	4	0	2
0.98730	102.559	1	3	1	3
0.97830	103.884	1	3	0	4
0.97620	104.199	1	3	2	0
0.96360	106.145	1	2	0	5

Table A.2 XRD Data of Iron Oxide

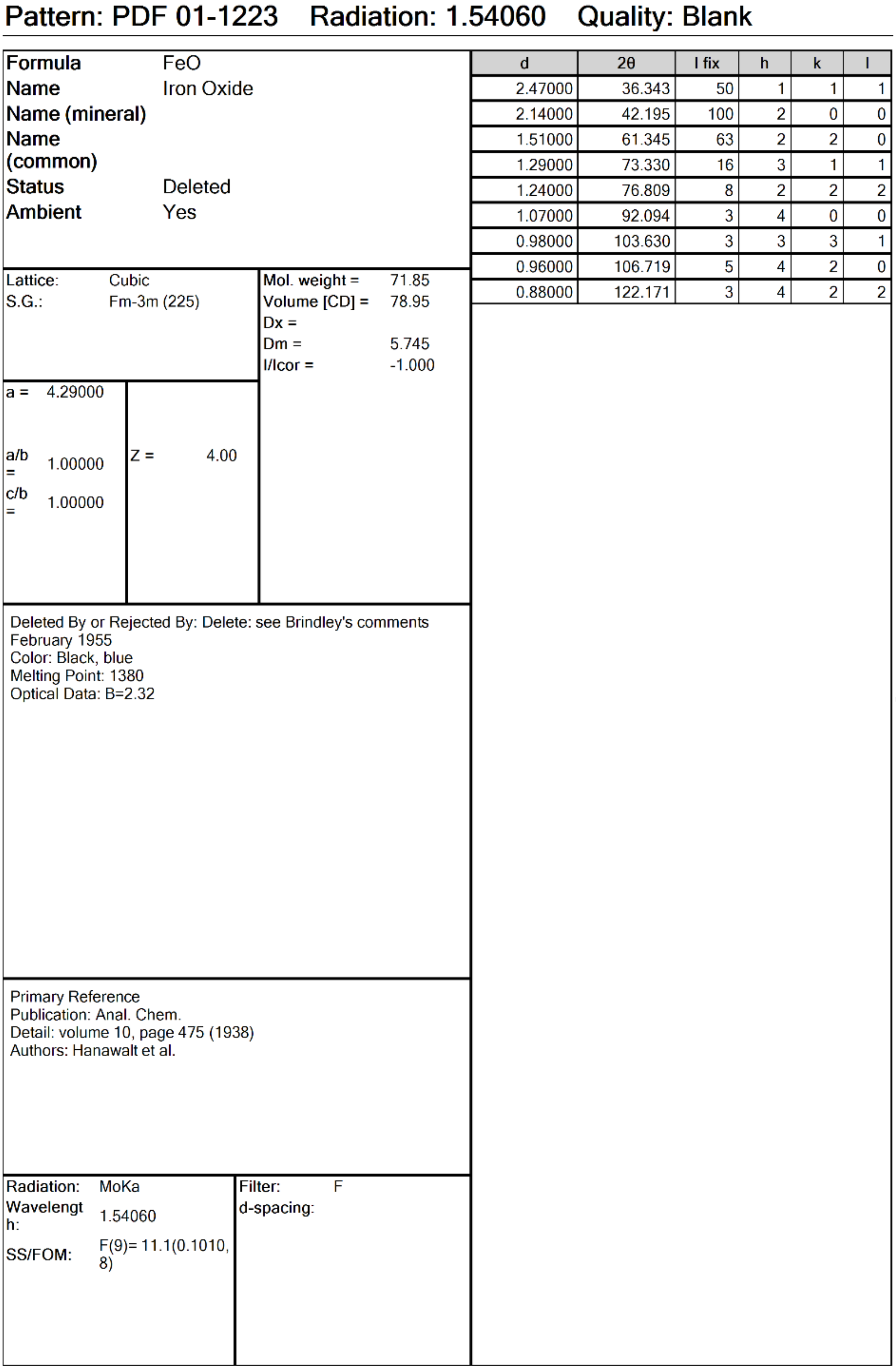

Pattern: PDF 01-1223 Radiation: 1.54060 Quality: Blank

Formula FeO
Name Iron Oxide
Name (mineral)
Name (common)
Status Deleted
Ambient Yes

Lattice: Cubic
S.G.: Fm-3m (225)

Mol. weight = 71.85
Volume [CD] = 78.95
Dx =
Dm = 5.745
I/Icor = -1.000

a = 4.29000
a/b = 1.00000
c/b = 1.00000
Z = 4.00

Deleted By or Rejected By: Delete: see Brindley's comments February 1955
Color: Black, blue
Melting Point: 1380
Optical Data: B=2.32

Primary Reference
Publication: Anal. Chem.
Detail: volume 10, page 475 (1938)
Authors: Hanawalt et al.

Radiation: MoKa
Wavelength: 1.54060
SS/FOM: F(9)= 11.1(0.1010, 8)
Filter: F
d-spacing:

d	2θ	I fix	h	k	l
2.47000	36.343	50	1	1	1
2.14000	42.195	100	2	0	0
1.51000	61.345	63	2	2	0
1.29000	73.330	16	3	1	1
1.24000	76.809	8	2	2	2
1.07000	92.094	3	4	0	0
0.98000	103.630	3	3	3	1
0.96000	106.719	5	4	2	0
0.88000	122.171	3	4	2	2

Table A.3 XRD Data of Iron Oxide, Hematite

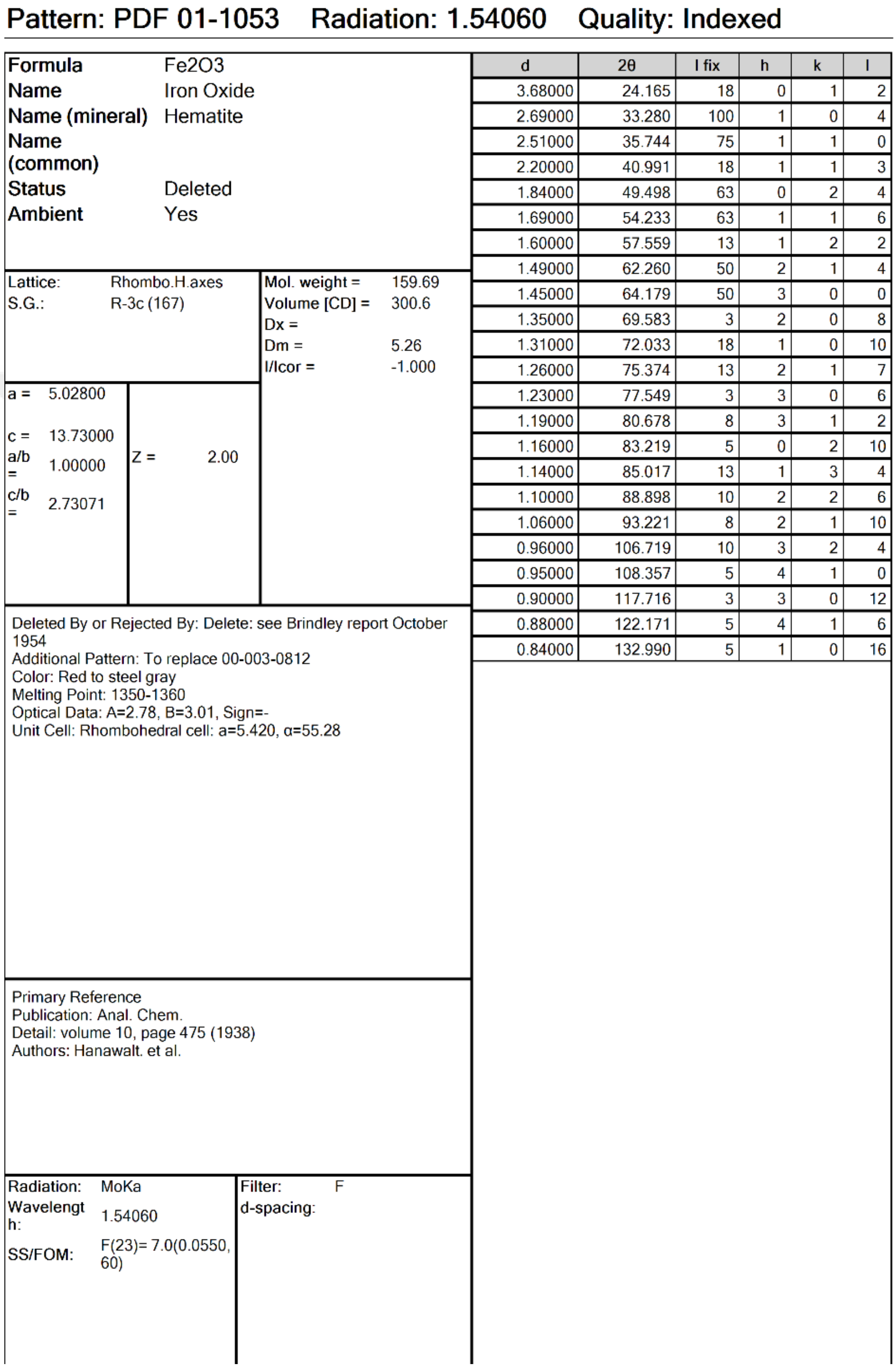

Pattern: PDF 01-1053 Radiation: 1.54060 Quality: Indexed

Formula	Fe2O3
Name	Iron Oxide
Name (mineral)	Hematite
Name (common)	
Status	Deleted
Ambient	Yes

Lattice:	Rhombo.H.axes	Mol. weight =	159.69
S.G.:	R-3c (167)	Volume [CD] =	300.6
		Dx =	
		Dm =	5.26
		I/Icor =	-1.000

a = 5.02800

c = 13.73000

a/b = 1.00000

c/b = 2.73071

Z = 2.00

Deleted By or Rejected By: Delete: see Brindley report October 1954
Additional Pattern: To replace 00-003-0812
Color: Red to steel gray
Melting Point: 1350-1360
Optical Data: A=2.78, B=3.01, Sign=-
Unit Cell: Rhombohedral cell: a=5.420, α=55.28

Primary Reference
Publication: Anal. Chem.
Detail: volume 10, page 475 (1938)
Authors: Hanawalt. et al.

Radiation:	MoKa	Filter:	F
Wavelength:	1.54060	d-spacing:	
SS/FOM:	F(23)= 7.0(0.0550, 60)		

d	2θ	I fix	h	k	l
3.68000	24.165	18	0	1	2
2.69000	33.280	100	1	0	4
2.51000	35.744	75	1	1	0
2.20000	40.991	18	1	1	3
1.84000	49.498	63	0	2	4
1.69000	54.233	63	1	1	6
1.60000	57.559	13	1	2	2
1.49000	62.260	50	2	1	4
1.45000	64.179	50	3	0	0
1.35000	69.583	3	2	0	8
1.31000	72.033	18	1	0	10
1.26000	75.374	13	2	1	7
1.23000	77.549	3	3	0	6
1.19000	80.678	8	3	1	2
1.16000	83.219	5	0	2	10
1.14000	85.017	13	1	3	4
1.10000	88.898	10	2	2	6
1.06000	93.221	8	2	1	10
0.96000	106.719	10	3	2	4
0.95000	108.357	5	4	1	0
0.90000	117.716	3	3	0	12
0.88000	122.171	5	4	1	6
0.84000	132.990	5	1	0	16

Table A.4 XRD Data of Iron Oxide, Magnetite

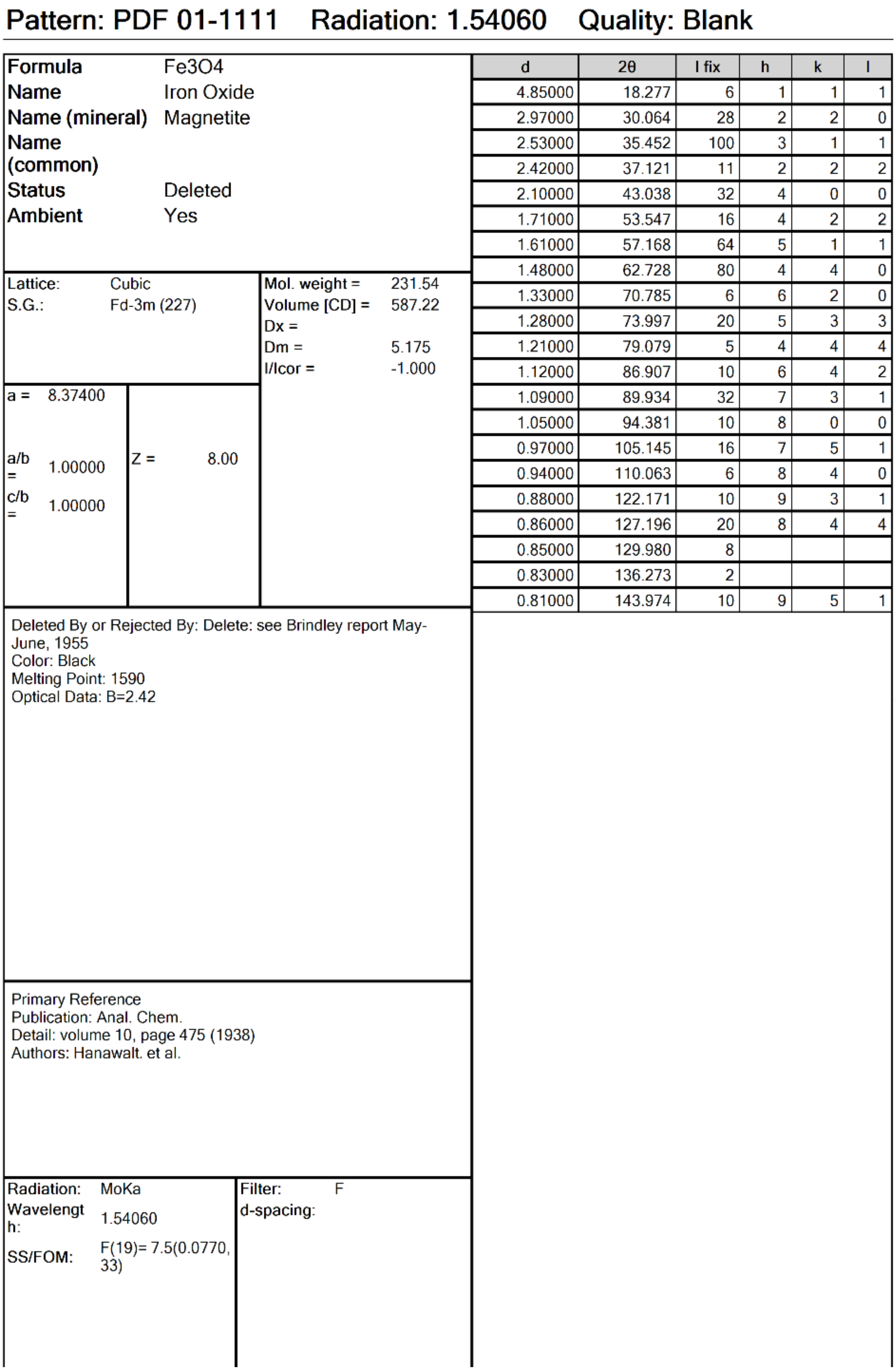

Pattern: PDF 01-1111 Radiation: 1.54060 Quality: Blank

Formula	Fe3O4
Name	Iron Oxide
Name (mineral)	Magnetite
Name (common)	
Status	Deleted
Ambient	Yes

Lattice:	Cubic	Mol. weight =	231.54
S.G.:	Fd-3m (227)	Volume [CD] =	587.22
		Dx =	
		Dm =	5.175
		I/Icor =	-1.000

a =	8.37400	Z =	8.00
a/b =	1.00000		
c/b =	1.00000		

Deleted By or Rejected By: Delete: see Brindley report May-June, 1955
Color: Black
Melting Point: 1590
Optical Data: B=2.42

Primary Reference
Publication: Anal. Chem.
Detail: volume 10, page 475 (1938)
Authors: Hanawalt. et al.

Radiation:	MoKa	Filter:	F
Wavelength:	1.54060	d-spacing:	
SS/FOM:	F(19)= 7.5(0.0770, 33)		

d	2θ	I fix	h	k	l
4.85000	18.277	6	1	1	1
2.97000	30.064	28	2	2	0
2.53000	35.452	100	3	1	1
2.42000	37.121	11	2	2	2
2.10000	43.038	32	4	0	0
1.71000	53.547	16	4	2	2
1.61000	57.168	64	5	1	1
1.48000	62.728	80	4	4	0
1.33000	70.785	6	6	2	0
1.28000	73.997	20	5	3	3
1.21000	79.079	5	4	4	4
1.12000	86.907	10	6	4	2
1.09000	89.934	32	7	3	1
1.05000	94.381	10	8	0	0
0.97000	105.145	16	7	5	1
0.94000	110.063	6	8	4	0
0.88000	122.171	10	9	3	1
0.86000	127.196	20	8	4	4
0.85000	129.980	8			
0.83000	136.273	2			
0.81000	143.974	10	9	5	1

Table A.5 XRD Data of Iron, Cubic

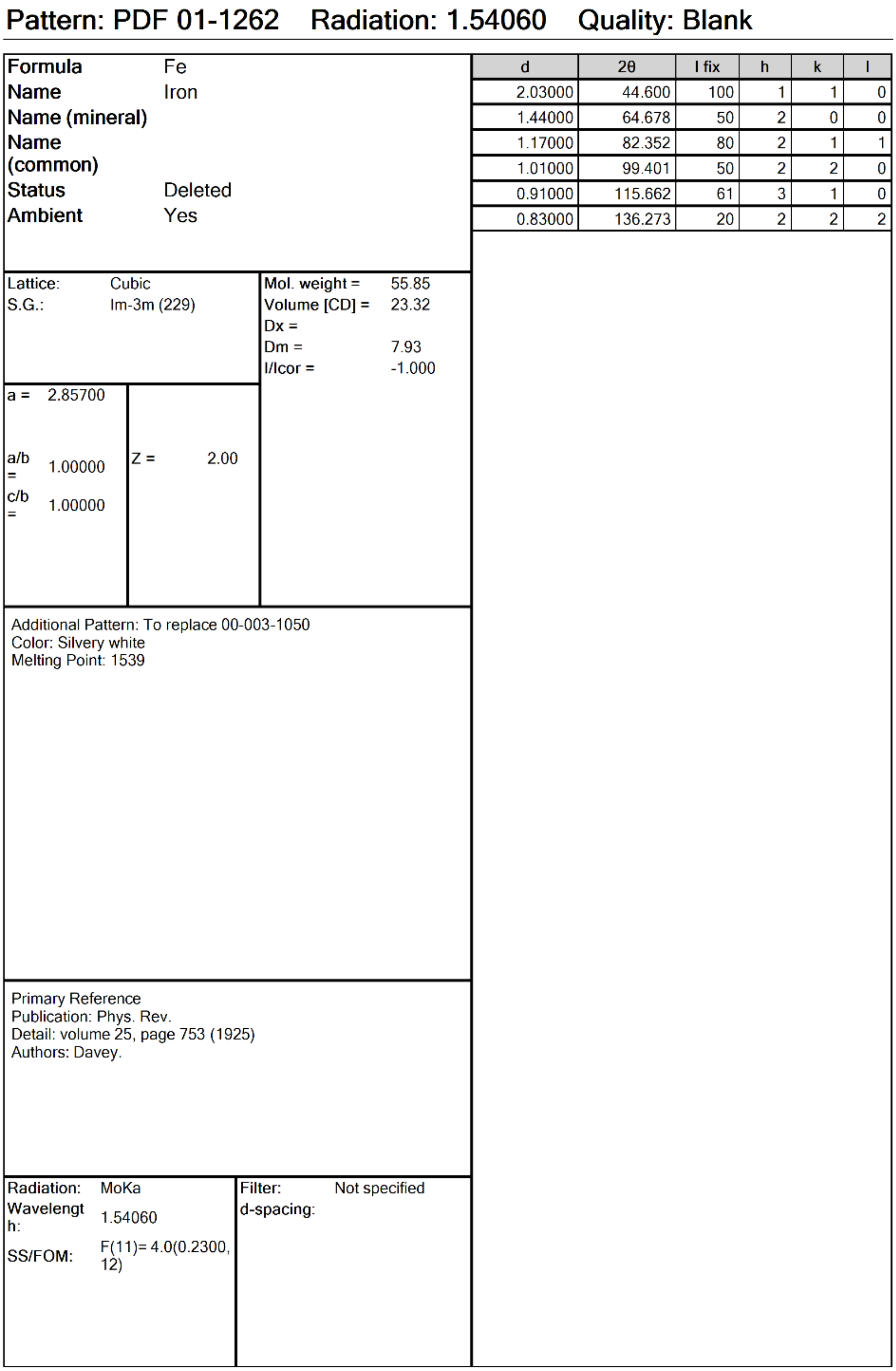

Pattern: PDF 01-1262 Radiation: 1.54060 Quality: Blank

Formula Fe
Name Iron
Name (mineral)
Name (common)
Status Deleted
Ambient Yes

d	2θ	I fix	h	k	l
2.03000	44.600	100	1	1	0
1.44000	64.678	50	2	0	0
1.17000	82.352	80	2	1	1
1.01000	99.401	50	2	2	0
0.91000	115.662	61	3	1	0
0.83000	136.273	20	2	2	2

Lattice: Cubic
S.G.: Im-3m (229)

Mol. weight = 55.85
Volume [CD] = 23.32
Dx =
Dm = 7.93
I/Icor = -1.000

a = 2.85700
a/b = 1.00000
c/b = 1.00000

Z = 2.00

Additional Pattern: To replace 00-003-1050
Color: Silvery white
Melting Point: 1539

Primary Reference
Publication: Phys. Rev.
Detail: volume 25, page 753 (1925)
Authors: Davey.

Radiation: MoKa
Wavelength: 1.54060
SS/FOM: F(11)= 4.0(0.2300, 12)

Filter: Not specified
d-spacing:

Table A.6 XRD Data of Aluminum Oxide, Corundum, syn

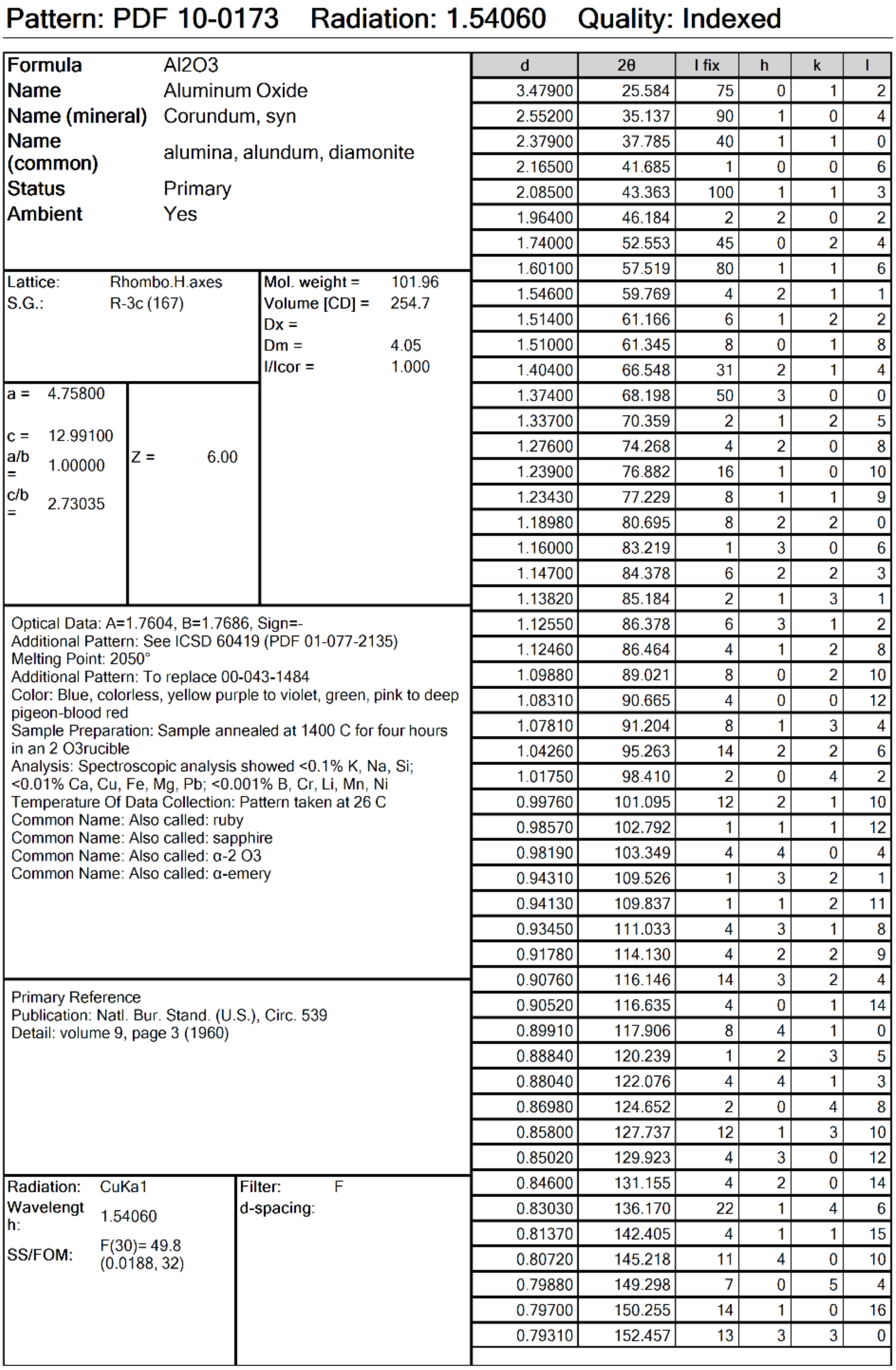

Pattern: PDF 10-0173 Radiation: 1.54060 Quality: Indexed

Formula	Al2O3
Name	Aluminum Oxide
Name (mineral)	Corundum, syn
Name (common)	alumina, alundum, diamonite
Status	Primary
Ambient	Yes

Lattice: Rhombo.H.axes
S.G.: R-3c (167)

Mol. weight = 101.96
Volume [CD] = 254.7
Dx =
Dm = 4.05
I/Icor = 1.000

a = 4.75800
c = 12.99100
a/b = 1.00000
c/b = 2.73035

Z = 6.00

Optical Data: A=1.7604, B=1.7686, Sign=-
Additional Pattern: See ICSD 60419 (PDF 01-077-2135)
Melting Point: 2050°
Additional Pattern: To replace 00-043-1484
Color: Blue, colorless, yellow purple to violet, green, pink to deep pigeon-blood red
Sample Preparation: Sample annealed at 1400 C for four hours in an 2 O3rucible
Analysis: Spectroscopic analysis showed <0.1% K, Na, Si; <0.01% Ca, Cu, Fe, Mg, Pb; <0.001% B, Cr, Li, Mn, Ni
Temperature Of Data Collection: Pattern taken at 26 C
Common Name: Also called: ruby
Common Name: Also called: sapphire
Common Name: Also called: α-2 O3
Common Name: Also called: α-emery

Primary Reference
Publication: Natl. Bur. Stand. (U.S.), Circ. 539
Detail: volume 9, page 3 (1960)

Radiation: CuKa1
Wavelength: 1.54060
SS/FOM: F(30)= 49.8 (0.0188, 32)

Filter: F
d-spacing:

d	2θ	I fix	h	k	l
3.47900	25.584	75	0	1	2
2.55200	35.137	90	1	0	4
2.37900	37.785	40	1	1	0
2.16500	41.685	1	0	0	6
2.08500	43.363	100	1	1	3
1.96400	46.184	2	2	0	2
1.74000	52.553	45	0	2	4
1.60100	57.519	80	1	1	6
1.54600	59.769	4	2	1	1
1.51400	61.166	6	1	2	2
1.51000	61.345	8	0	1	8
1.40400	66.548	31	2	1	4
1.37400	68.198	50	3	0	0
1.33700	70.359	2	1	2	5
1.27600	74.268	4	2	0	8
1.23900	76.882	16	1	0	10
1.23430	77.229	8	1	1	9
1.18980	80.695	8	2	2	0
1.16000	83.219	1	3	0	6
1.14700	84.378	6	2	2	3
1.13820	85.184	2	1	3	1
1.12550	86.378	6	3	1	2
1.12460	86.464	4	1	2	8
1.09880	89.021	8	0	2	10
1.08310	90.665	4	0	0	12
1.07810	91.204	8	1	3	4
1.04260	95.263	14	2	2	6
1.01750	98.410	2	0	4	2
0.99760	101.095	12	2	1	10
0.98570	102.792	1	1	1	12
0.98190	103.349	4	4	0	4
0.94310	109.526	1	3	2	1
0.94130	109.837	1	1	2	11
0.93450	111.033	4	3	1	8
0.91780	114.130	4	2	2	9
0.90760	116.146	14	3	2	4
0.90520	116.635	4	0	1	14
0.89910	117.906	8	4	1	0
0.88840	120.239	1	2	3	5
0.88040	122.076	4	4	1	3
0.86980	124.652	2	0	4	8
0.85800	127.737	12	1	3	10
0.85020	129.923	4	3	0	12
0.84600	131.155	4	2	0	14
0.83030	136.170	22	1	4	6
0.81370	142.405	4	1	1	15
0.80720	145.218	11	4	0	10
0.79880	149.298	7	0	5	4
0.79700	150.255	14	1	0	16
0.79310	152.457	13	3	3	0

Table A.7 XRD Data of Aluminum, Cubic

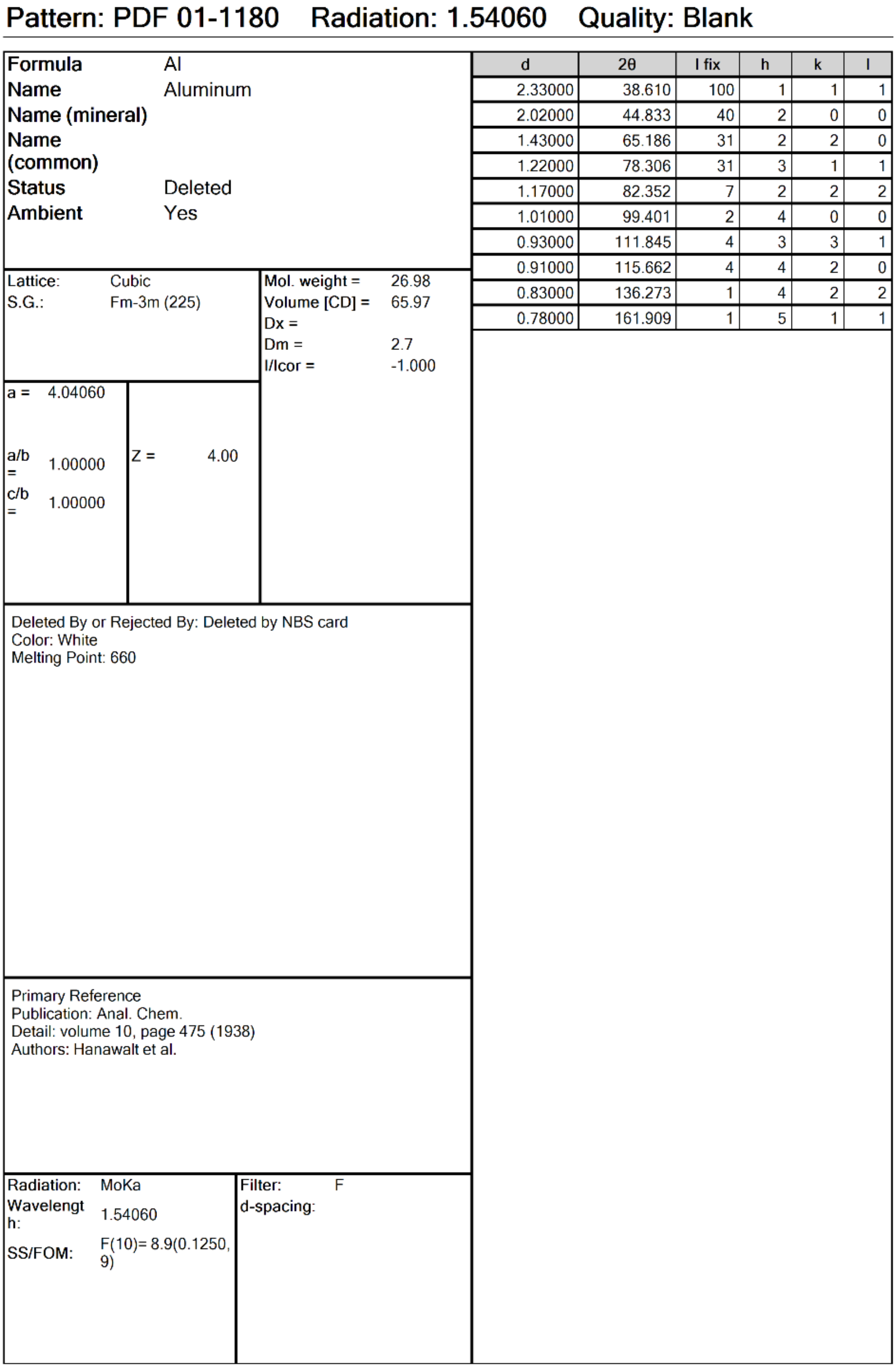

Pattern: PDF 01-1180   Radiation: 1.54060   Quality: Blank

Formula	Al
Name	Aluminum
Name (mineral)	
Name (common)	
Status	Deleted
Ambient	Yes

Lattice: Cubic
S.G.: Fm-3m (225)

Mol. weight = 26.98
Volume [CD] = 65.97
Dx =
Dm = 2.7
I/Icor = -1.000

a = 4.04060
a/b = 1.00000
c/b = 1.00000

Z = 4.00

Deleted By or Rejected By: Deleted by NBS card
Color: White
Melting Point: 660

Primary Reference
Publication: Anal. Chem.
Detail: volume 10, page 475 (1938)
Authors: Hanawalt et al.

Radiation: MoKa
Wavelength: 1.54060
SS/FOM: F(10)= 8.9(0.1250, 9)

Filter: F
d-spacing:

d	2θ	I fix	h	k	l
2.33000	38.610	100	1	1	1
2.02000	44.833	40	2	0	0
1.43000	65.186	31	2	2	0
1.22000	78.306	31	3	1	1
1.17000	82.352	7	2	2	2
1.01000	99.401	2	4	0	0
0.93000	111.845	4	3	3	1
0.91000	115.662	4	4	2	0
0.83000	136.273	1	4	2	2
0.78000	161.909	1	5	1	1

Table A.8 XRD Data of Aluminum Silicate, Sillimanite

Pattern: PDF 01-0626 Radiation: 1.54060 Quality: Indexed

Formula	Al2O3·SiO2
Name	Aluminum Silicate
Name (mineral)	Sillimanite
Name (common)	
Status	Deleted
Ambient	Yes

Lattice:	Orthorhombic
S.G.:	Pbnm (62)

Mol. weight =	162.05
Volume [CD] =	328.04
Dx =	
Dm =	3.247
I/Icor =	-1.000

a =	7.50000
b =	7.66000
c =	5.71000
a/b =	0.97911
c/b =	0.74543

Z = 4.00

d	2θ	I fix	h	k	l
3.40000	26.189	100	1	2	0
2.89000	30.917	40	2	1	1
2.68000	33.408	40	2	2	0
2.54000	35.308	61	1	1	2
2.41000	37.281	20	1	3	0
2.27000	39.673	40	2	0	2
2.19000	41.187	61	1	2	2
2.11000	42.824	40	2	3	0
1.97000	46.035	20	3	2	1
1.87000	48.652	20	4	0	0
1.83000	49.786	20	3	1	2
1.69000	54.233	61	3	2	2
1.59000	57.955	20	0	4	2
1.56000	59.179	20	1	4	2
1.52000	60.899	61	3	4	0
1.44000	64.678	61	4	2	2
1.39000	67.307	20	5	2	0
1.33000	70.785	61	1	4	3
1.27000	74.679	40	2	5	2
1.25000	76.084	40	6	0	0

Deleted By or Rejected By: Delete: Berry parcel of January 20, 1959, see 1-614, 10-369, 22-18
Color: Colorless
Sample Source Or Locality: Specimen from Delaware Co., Pennsylvania, USA
Optical Data: A=1.659, B=1.660, Q=1.681, Sign=+, 2V=25-30°

Primary Reference
Publication: Am. J. Sci.
Detail: volume 11, page 459 (1926)
Authors: Wyckoff, Grieg, Bowen.

Radiation:	MoKa1
Wavelength:	1.54060
SS/FOM:	F(20)= 4.1(0.0470, 104)

Filter:	Not specified
d-spacing:	

B. EDX Spectra of the Synthesized Catalysts

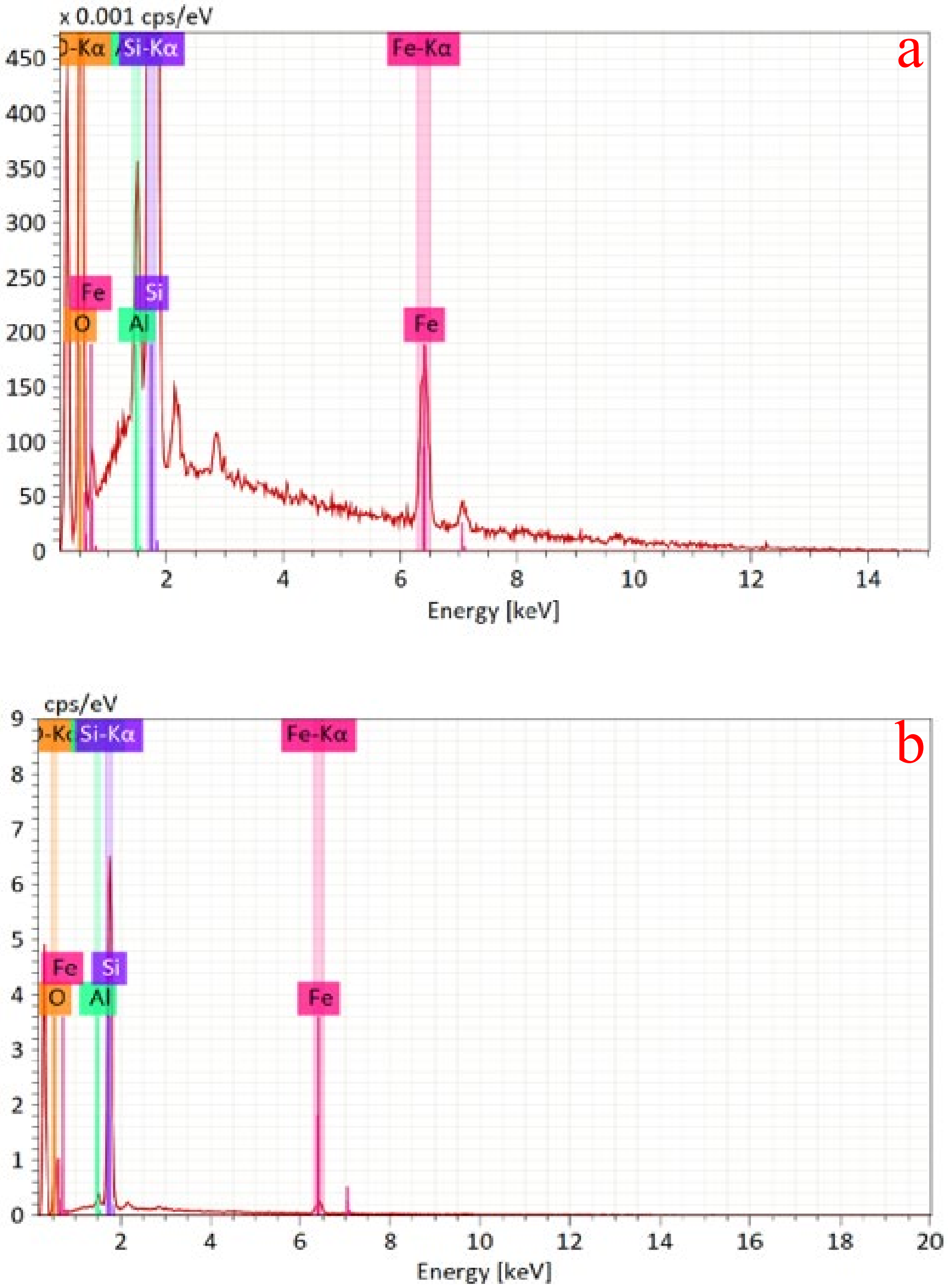

Figure B.1 EDX spectra of SimSAU2Al13Fe catalyst from different regions: a) Region 1, and b) Region 2

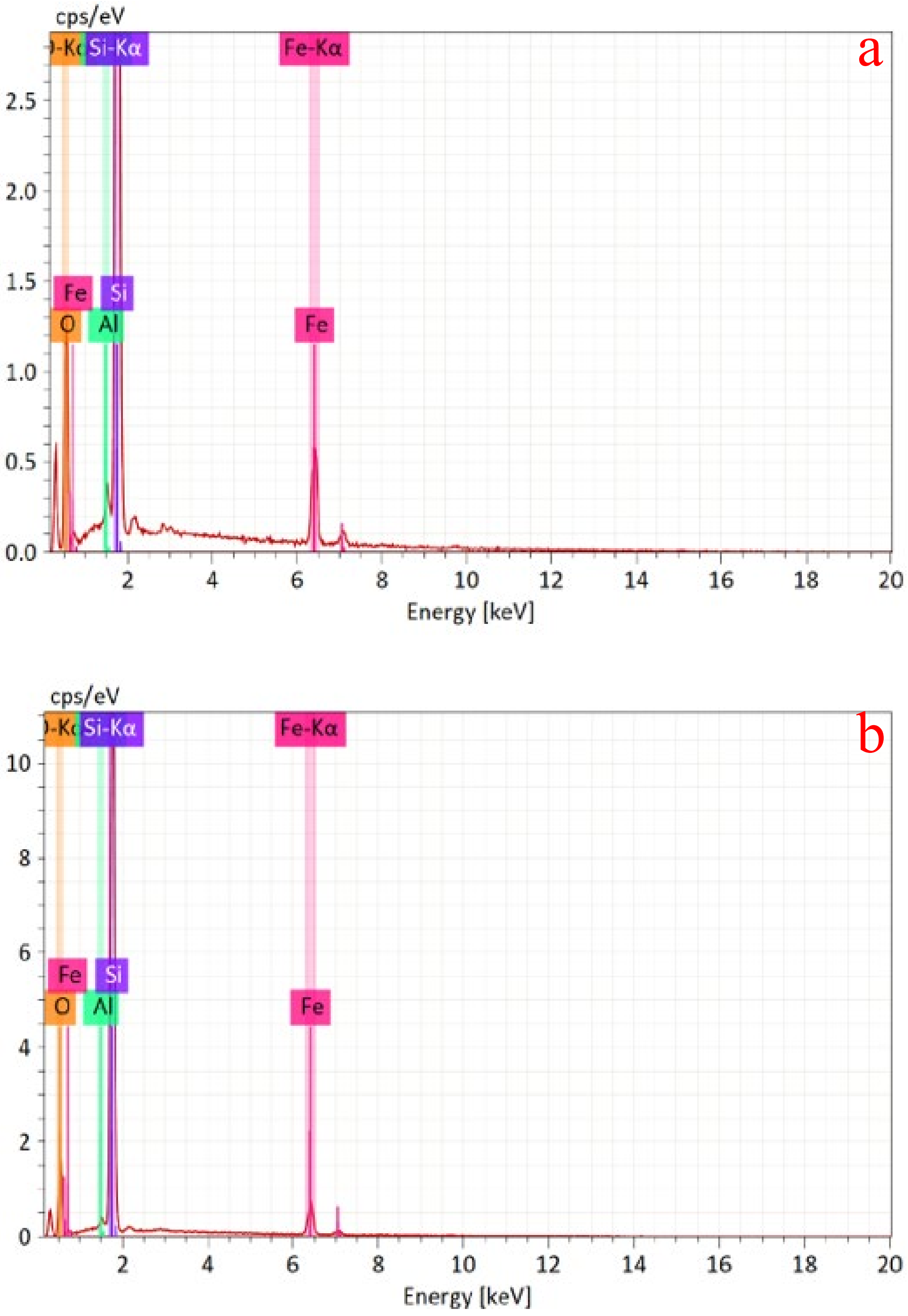

Figure B.2 EDX spectra of SimSAU1Al14Fe catalyst from different regions: a) Region 1, and b) Region 2

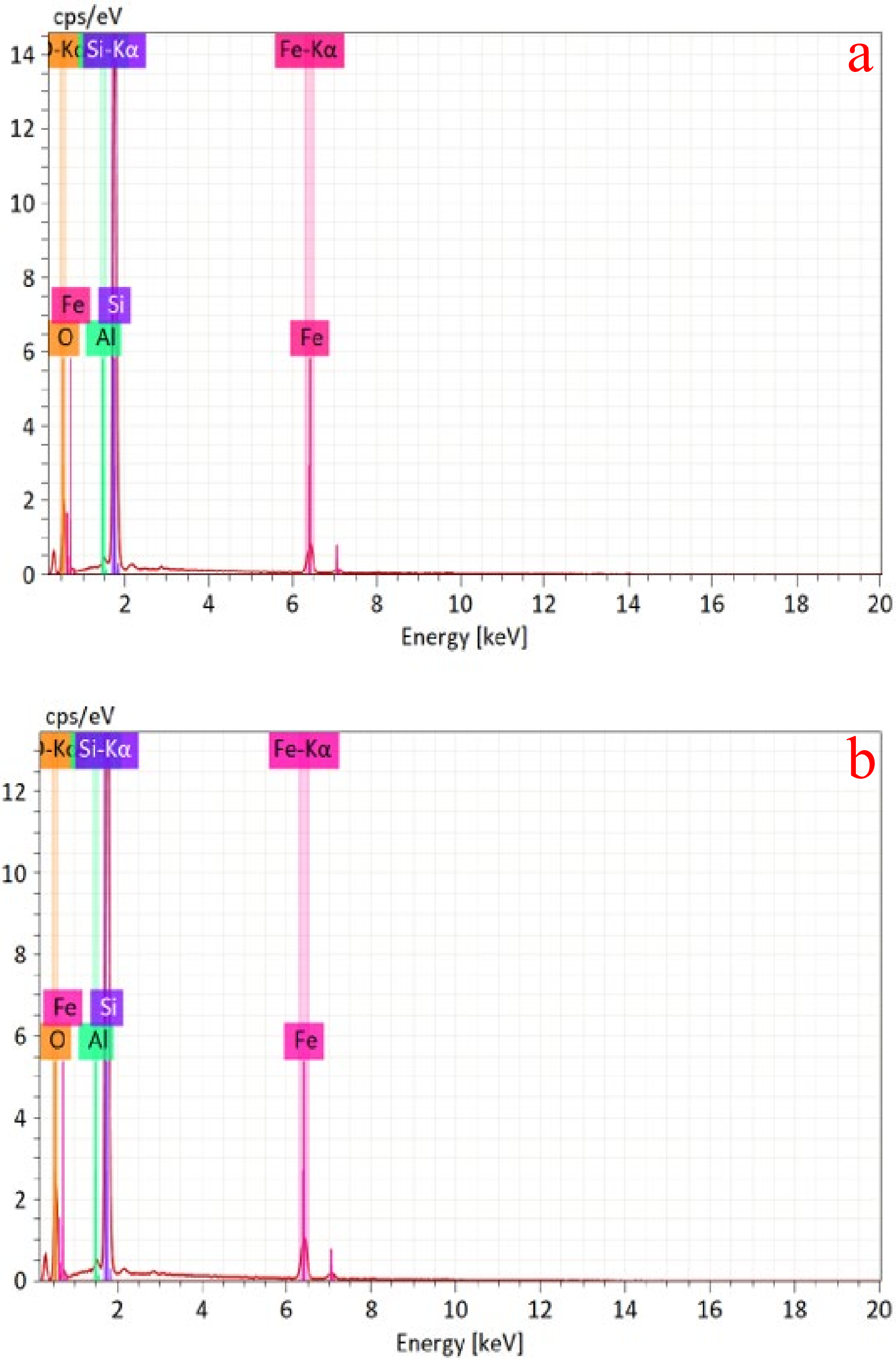

Figure B.3 EDX spectra of SimSAU0.5Al14.5Fe catalyst from different regions:

a) Region 1, and b) Region 2

C. Calculation of Activation Energy Procedure Regarding PLA Degradation Reaction

Kinetic parameters related to PLA degradation reaction taking place were estimated based on a power law model that was mentioned by Obalı for general polymer degradation reaction (Obalı, 2010). Accordingly, the PLA degradation reaction rate was expressed as follows:

$$\frac{d\alpha}{dt} = Ae^{-E_a/RT}(1-\alpha)^n \tag{C.1}$$

α displays the decomposition fraction of PLA at time t for the overall reaction order of n. α was evaluated as follows:

$$\alpha = \frac{\omega_0 - \omega_t}{\omega_0 - \omega_\infty} \tag{C.2}$$

$$\frac{dT}{dt} = q \tag{C.3}$$

where ω_0 stands for the initial weight of the sample; ω_t sample weight at any time and ω_∞ sample weight at infinite time. Applying linear heating rate equation C.3 and combining equations C.1, C.2, and C.3, the following equation C.4 could be obtained.

$$\frac{1-(1-\alpha)^{(1-n)}}{(1-n)T^2} = \frac{AR}{qE_a}[1 - \frac{2RT}{E_a}]e^{\frac{-E_a}{RT}} \text{ for } n \neq 1 \tag{C.4}$$

$\frac{2RT}{E_a}$ term could be neglected compared to 1 within the $[1 - \frac{2RT}{E_a}]$ term and taking the natural logarithm of both sides of equation C.4, equation C.5 was obtained.

$$ln\frac{1-(1-\alpha)^{(1-n)}}{(1-n)T^2} = ln\frac{AR}{qE_a} - \frac{E_a}{RT} \text{ for } n \neq 1 \tag{C.5}$$

Depending on the order of the reaction, equation C.5 could be modified, and if a similar analysis was conducted for $n = 1$, equation C.6 could be achieved.

$$ln\frac{-(1-\alpha)}{T^2} = ln\frac{AR}{qE_a} - \frac{E_a}{RT} \text{ for } n = 1 \tag{C.6}$$

Modifying equation C.6 as

$$-ln\frac{-(1-\alpha)}{T^2} = y; \tag{C.7}$$

$$\frac{1}{T} = x; \tag{C.8}$$

$$\frac{E_a}{R}(\frac{1}{T}) = a * x; \tag{C.9}$$

$$-ln\frac{AR}{qE_a} = b \tag{C.10}$$

A linear relation was obtained as y=a*x+b where how y, x, a, & b terms were defined as given in equations C.7-C.10. By plotting this linear relation from the slope of this linear plot, activation energy regarding PLA decomposition reaction could be obtained. Figure C.1 exhibits the results of utilizing the above-mentioned procedure for reaction orders of 1 and 2, respectively, for pure PLA decomposition.

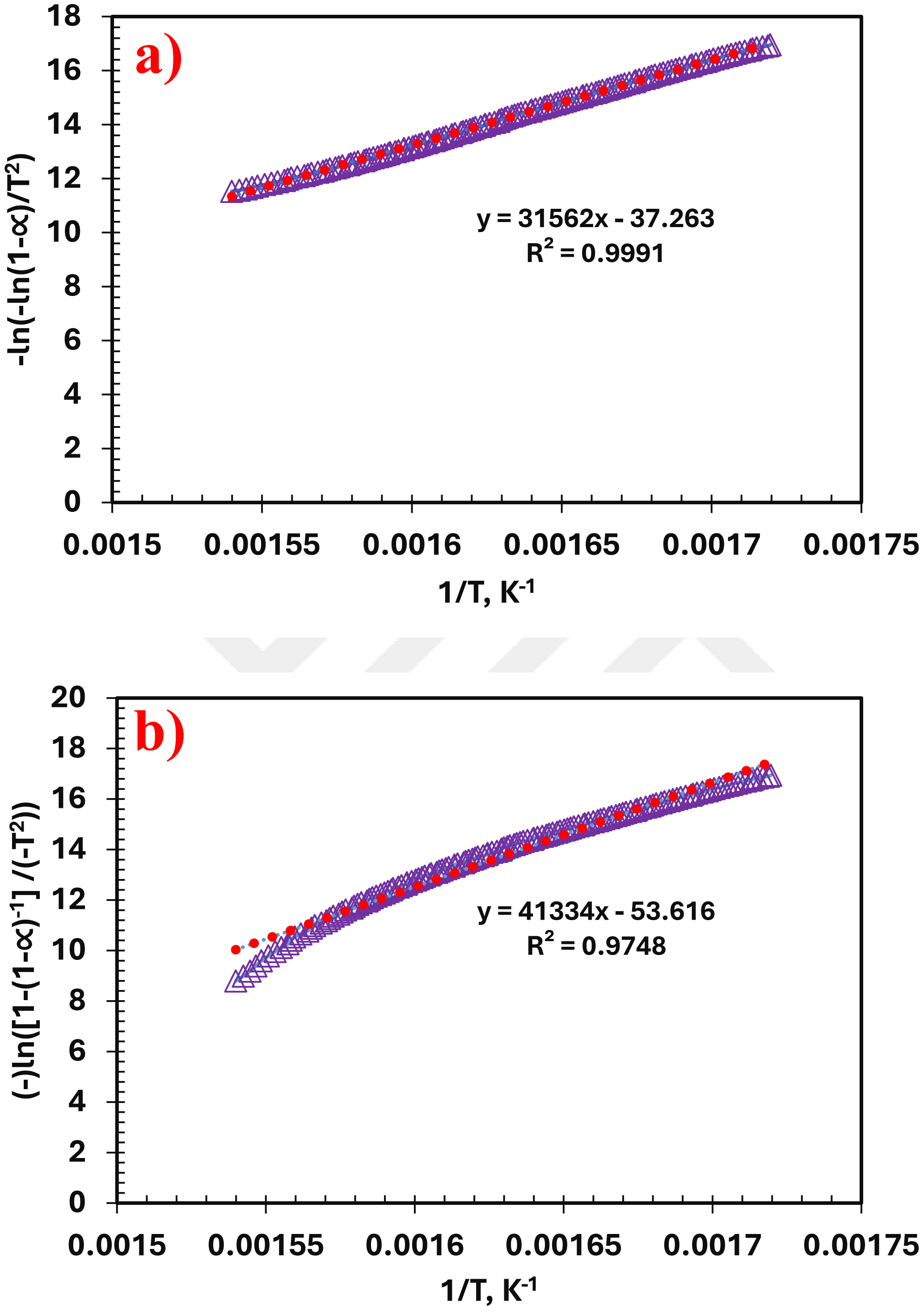

Figure C.1 Determination of reaction order of PLA degradation reaction:

a) reaction order of 1 and b) reaction order of 2 (Sivri, 2023)

D. Calculation of Solid, Condensable, and Non-condensable Product Yields and Weight Fraction of Compounds in Condensable Products

Yields regarding solid, condensable, and non-condensable products were calculated by using equation D.1. The solid products were calculated by weighing the initial and final weights of the reactor whereas condensable products were calculated by applying the same procedure for condenser traps.

$$M_{\text{non-condensable}} = M_{\text{initial PLA}} - M_{\text{solid}} - M_{\text{condensable}} \tag{D.1}$$

Since M_{solid}, $M_{\text{condensable}}$ could be calculated by utilizing weight differences of reactor and condenser traps, and knowing the initial weight of PLA, $M_{\text{non-condensable}}$ could be found.

Then, regarding yields could be calculated as shown in equation D.2:

$$Y_i\,(\%) = \frac{M_i}{M_{initial\ PLA}} * 100 \tag{D.2}$$

where M_i stands for the weight of the solid (for solid yield), or condensable (for condensable yield), or non-condensable (for non-condensable yield) products and $M_{initial\ PLA}$ stands for the initial weight of PLA.

The weight fraction of the condensable products can be calculated from equation D.3.

$$W_i\,(\text{wt. }\%) = \frac{M_i}{M_{condensable}} * 100 \tag{D.3}$$

E. Calculation of Relative Response Factor and Number of Moles of the Components in the Condensable Products

RRF technique and calibration factors performed by Sivri in her Ph.D study were utilized (Sivri, 2023).

Accordingly, Tables E.1 & E.2 and equations E.1-E.5 were utilized to calculate the species' number of moles, mass, and weight fractions.

Table E. 1 RRF values and the retention times of the compounds

Compound	Molecular Weight (g/mol)	Retention Times (min)	RRF
D L, L	144.1	15.3	1.41
Meso L	144.1	14.2	1.41
LA	90.08	8.3	0.36
PA	74.08	7.3	1

Table E. 2 Densities of the compounds

Compound	Density (g/cm^3)
D L, L	1.186
Meso L	1.186
LA	1.209
PA	0.988

Equations E.1 & E.2 were used to calculate the number of moles of acetone, and the number of moles of the compounds in condensable products, respectively.

$$N_{C_3H_6O} = \frac{V_{C_3H_6O}}{MW_{C_3H_6O}} * \rho_{C_3H_6O} \quad \text{(E.1)}$$

$$N_i = \frac{A_i}{A_{C_3H_6O}} * \frac{1}{RRF_i} * N_{C_3H_6O} \quad \text{(E.2)}$$

where A_i is the chromatogram peak area of compound i, and units of the N, V, MW, ρ, and A in equations E.1 and E.2 are mol, ml, g/mol, g/ml, and mVolt^2*sec, respectively.

The mass and weight fractions of condensable products were calculated using equations E.3-E.5.

$$M_i = N_i * MW_i \quad \text{(E.3)}$$

$$M_{condensable} = \sum_{i=1}^{j} M_i * MW_i \quad \text{(E.4)}$$

$$W_i\ (\text{wt. \%}) = \frac{M_i}{M_{condensable}} * 100\% \quad \text{(E.5)}$$

F. Calculation of Mole Fraction of Compounds in Non-condensable Products

Beta factors and calibration factors performed by Sivri in her Ph.D study were utilized (Sivri, 2023). Accordingly, Table F.1 and equations F.1-F.4 were utilized to calculate the beta factor, number of moles, and compositions of the species.

Table F. 1 Beta factors and the retention times of the gas compounds

Compound	**Retention Times (min)**	**β factor**
Hydrogen, H_2	2.7	0.14
Carbon monoxide, CO	5	1.42
Methane, CH_4	9.8	0.35
Carbon dioxide, CO_2	13.1	1.00
Ethylene, C_2H_4	17.5	0.39
Acetaldehyde, CH_3CHO	26.4	3.06

The beta factor of CO_2 is taken as 1, and beta factors of the other species were found by using equation F.1.

$$\beta_i = \frac{A_{CO_2} * \beta_{CO_2}}{A_i} * \frac{N_i}{N_{CO_2}} \tag{F.1}$$

Then using equations F.2 and F.3 species moles and the total number of moles of non-condensable products were found.

$$N_i = \beta_i * A_i \tag{F.2}$$

$$N_{non-condensable} = N_{CO} + N_{CO_2} + N_{C_2H_4O} + N_{H_2} \tag{F.3}$$

Finally, utilizing equation F.4, the mole fraction of each compound in non-condensable products was found.

$$y_i \text{ (mol \%)} = \frac{N_i}{N_{non-condensable}} * 100 \tag{F.4}$$